

NASA Contractor Report 174733

(NASA-CR-174733) ADVANCED COMPOSITE
COMBUSTOR STRUCTURAL CONCEPTS PROGRAM Final
Report (Pratt and Whitney Aircraft) 118 p
CSCI 11D

N87-20387

Unclas

G3/24 45324

ADVANCED COMPOSITE COMBUSTOR STRUCTURAL CONCEPTS PROGRAM

Final Report

P-118

IN - CAT. 24

65658

M.A. Sattar and R.P. Lohmann

Contract NAS3-23284

December 1984

NASA

Copy Number

00046

1. REPORT NO. NASA CR-174333		2. GOVERNMENT AGENCY		3. RECIPIENT'S CATALOG NO.	
4. TITLE AND SUBTITLE ADVANCED COMPOSITE COMBUSTOR STRUCTURAL CONCEPTS PROGRAM				5. REPORT DATE December, 1984	
				6. PERFORMING ORG. CODE	
7. AUTHOR(S) M. A. Sattar and R. P. Lohmann				8. PERFORMING ORG. REPT. NO. PWA 5890-24	
9. PERFORMING ORG. NAME AND ADDRESS UNITED TECHNOLOGIES CORPORATION Pratt & Whitney Engineering Division				10. WORK UNIT NO.	
				11. CONTRACT OR GRANT NO. NAS3-23284	
12. SPONSORING AGENCY NAME AND ADDRESS National Aeronautics and Space Administration Lewis Research Center 21000 Brookpark Road, Cleveland, Ohio 44135				13. TYPE REPT./PERIOD COVERED Final Report	
				14. SPONSORING AGENCY CODE	
15. SUPPLEMENTARY NOTES					
16. ABSTRACT An analytical study was conducted to assess the feasibility of and benefits derived from the use of high temperature composite materials in aircraft turbine engine combustor liners. The study included a survey and screening of the properties of three candidate composite materials including tungsten reinforced superalloys, carbon-carbon and silicon carbide (SiC) fibers reinforcing a ceramic matrix of lithium aluminosilicate (LAS). The SiC-LAS material was selected as offering the greatest near term potential primarily on the basis of high temperature capability. A limited experimental investigation was conducted to quantify some of the more critical mechanical properties of the SiC-LAS composite having a multidirection 0°/45°/-45°/90° fiber orientation favored for the combustor liner application. Rigorous cyclic thermal tests demonstrated that SiC-LAS was extremely resistant to the thermal fatigue mechanisms that usually limit the life of metallic combustor liners. A thermal design study led to the definition of a composite liner concept that incorporated film cooled SiC-LAS shingles mounted on a Hastelloy X shell. With coolant fluxes consistent with the most advanced metallic liner technology, the calculated hot surface temperatures of the shingles were within the apparent near term capability of the material. Structural analyses indicated that the stresses in the composite panels were low, primarily because of the low coefficient of expansion of the material and it was concluded that the dominant failure mode of the liner would be an as yet unidentified deterioration of the composite from prolonged exposure to high temperature. An economic study, based on a medium thrust size commercial aircraft engine, indicated that the SiC-LAS combustor liner would weigh 22.8N (11.27 lb) less and cost less to manufacture than advanced metallic liner concepts intended for use in the late 1980's.					
17. KEY WORDS (SUGGESTED BY AUTHOR(S)) Combustor, Liner, Composite Materials			18. DISTRIBUTION STATEMENT [REDACTED] until December 31, 1985		
19. SECURITY CLASS THIS (REPT) Unclassified		20. SECURITY CLASS THIS (PAGE) Unclassified		21. NO. PGS	
				22. PRICE *	

NASA Contractor Report 174733

ADVANCED COMPOSITE COMBUSTOR STRUCTURAL CONCEPTS PROGRAM

Final Report

**M.A. Sattar and R.P. Lohmann
United Technologies Corporation
Pratt & Whitney**

**Prepared for
NASA-Lewis Research Center
Under Contract NAS3-23284**



CONTRIBUTION

**This report will remain available
without limitation until
December 31, 1985.**

FOREWORD

This report presents the results of an analytical study conducted with limited experimental support to assess the feasibility of the use of advanced high temperature composite materials in aircraft gas turbine combustor liner applications. The study was conducted for the National Aeronautics and Space Administration (NASA) under Contract NAS3-23284.

The NASA Project Manager for this study was Dr. Robert L. Thompson of the Structures Section, Lewis Research Center, Cleveland, Ohio, and the Pratt & Whitney Program Manager was Dr. Robert P. Lohmann. Mohammed A. Sattar was the principal investigator for the study, while supporting laboratory characterization tests of the composite material were conducted at United Technologies Research Center under the direction of Dr. Karl M. Prewé.

TABLE OF CONTENTS

<u>Section</u>	<u>Page</u>
1.0 SUMMARY	1
2.0 INTRODUCTION	3
3.0 DEFINITION OF COMBUSTOR REQUIREMENTS	5
3.1 Reference Engine and Combustor	5
3.2 Combustor Operating Environment	8
3.3 Combustor Life and Performance Requirements	10
4.0 ANALYSIS OF REFERENCE METALLIC COMBUSTOR LINER	12
4.1 Metallic Liner Configuration	12
4.2 Thermal Analysis	14
4.3 Static Stress Analysis	15
4.4 Cyclic Fatigue Life Analysis	23
4.5 Segment Oxidation Life	24
4.6 Dynamic Analysis of the Liner	24
4.7 Summation	26
5.0 SURVEY OF HIGH TEMPERATURE COMPOSITE MATERIALS	27
5.1 Candidate Composite Materials	27
5.2 Survey Procedure	28
5.3 Material Property Survey Results	32
5.3.1 Temperature Limitations	32
5.3.2 Density	33
5.3.3 Strategic Materials	33
5.3.4 Thermal Conductivity and Expansion	33
5.3.5 Static Strength	34
5.3.6 Dynamic Strength	34
5.3.7 Thermal Fatigue	35
5.3.8 Workability	35
5.3.9 Miscellaneous Properties	36
5.4 Material Screening and Selection	36
6.0 EXPERIMENTAL EVALUATION OF COMPOSITE MATERIAL PROPERTIES	39
6.1 Test Specimen Fabrication	39
6.2 Evaluation of Static Load Characteristics	40
6.3 Creep Strength Characteristics	47
6.4 Mechanical Fatigue Tests	49
6.5 Thermal Fatigue Tests	55
6.6 Surface Radiant Emissivity	67
6.7 Thermal Expansion	67
6.8 Thermal Conductivity	69

TABLE OF CONTENTS (continued)

<u>Section</u>	<u>Page</u>
7.0 COMPOSITE COMBUSTOR LINER DEFINITION AND ANALYSIS	70
7.1 Preliminary Aerothermal Study	70
7.2 Composite Liner Concept Definition	74
7.3 Thermal Analysis of Composite Liner	79
7.4 Structural Model of the Composite Liner	83
7.5 Dynamic Structural Analysis	86
7.6 Static Structural Analysis	89
7.7 Liner Life Analysis	99
7.8 Summation	103
8.0 ECONOMIC BENEFIT ASSESSMENT	104
9.0 CONCLUDING REMARKS	109
REFERENCES	110

SECTION 1.0

SUMMARY

This report presents the results of an analytical study conducted with limited experimental support to assess the feasibility of and benefits derived from the use of high temperature composite materials in combustor liners for advanced aircraft turbine engines. The study was initiated with the definition of a reference metallic combustor liner which could be used as a basis for comparison with the advanced composite liner structural concept that would be evolved. The approach to defining the advanced composite liner consisted of screening of the properties of high temperature composites to select a material consistent with near term application. After definition of an advanced liner construction consistent with the use of the selected composite material, detailed parallel thermal and structural analyses were conducted of both the advanced liner and the reference metallic combustor liner to establish the relative merits of each.

The reference engine for this study was an advanced version of the PW2037 engine having components representative of late 1980's technology level. The combustor liner, which served as the reference metallic liner for this study, consisted of individual segments cast from high creep strength turbine alloys and attached to a Hastelloy X shell. Cooled primarily by convection on the cold side, the segments were projected to encounter peak metal temperatures of 1049°C (1920°F) at the takeoff condition and structural analyses indicated that the dominant failure mode would be cracking due to cyclic thermal fatigue. The analysis also showed the design life goal of 15,000 hours operation, based on a 90-minute flight cycle, could be achieved without excessive deterioration.

Three different high temperature composite materials were considered for the combustor liner application. These included tungsten wire reinforced superalloys originally conceived for application in turbine blades, carbon-carbon systems and a fiber reinforced ceramic consisting of silicon carbide (SiC) fibers in a matrix of lithium aluminosilicate (LAS). Following a survey and screening of the properties of these three materials, the SiC-LAS composite was selected as offering the greatest near term potential primarily on the basis of high temperature capability, low density and the lack of need for strategically critical or costly materials.

Nearly all of the available data on the mechanical properties of SiC-LAS composites had been obtained on materials with unidirectional fiber orientation, whereas the combustor liner application favored a multidirectional reinforcement. Consequently, a limited experimental program was conducted to acquire data on the most critical properties of SiC-LAS composites with 0°/+45°/-45°/90° fiber orientations. The most illuminating of these tests was a thermal fatigue assessment in which circular specimens of the material were cyclically heated in the center to temperatures of 1095 to 1317°C (2000 to 2400°F) and then cooled to 537°C (1000°F). After as many as 3500 and 4000 such cycles, the SiC-LAS specimens were found to have sustained, at most, only minute distress and cracking of the hot surface, whereas metal specimens evaluated at lower

peak temperatures bulged and cracked through after only a few cycles in the same apparatus. On the basis of these results, it was evident that the SiC-LAS material has a very high thermal fatigue resistance which is very desirable in a combustor liner material.

Due to its low thermal conductivity, the incorporation of the SiC-LAS composite material in the combustor liner required unique aerothermal design approaches. This led to the definition of a composite liner concept in which film cooled SiC-LAS shingles were attached to a Hastelloy X shell. Thermal analysis indicated the shingles would encounter a maximum hot side surface temperature of 1261°C (2303°F) at the takeoff operating condition while utilizing the same total quantity of cooling air as the reference metallic segment liner. This temperature appears to be within the near term capabilities of SiC-LAS composites, and a structural analysis revealed that the stresses in the liner panels consisted primarily of thermal stresses which were low due to the low thermal expansion of this material. On the basis of the low stress levels and the above cited high thermal fatigue resistance, it was concluded that the dominant distress mechanism for the SiC-LAS combustor liner panels would be deterioration due to accumulative exposure to high temperatures. While the specific mechanism of deterioration could not be identified on the basis of currently available data, an analytical model of this failure mechanism was formulated and, with reinforcement by experimental data, could be used in the future for predicting the life of ceramic composite liner materials.

The study was concluded with an economic benefit assessment in which the direct operating cost of the Boeing 757 aircraft with the reference PW2037 engine having the advanced composite combustor liner or the reference metallic liner was evaluated. While the results were not conclusive due to the incomplete definition of the service life of the composite liner panels, they did demonstrate that, in addition to being 22.8 N (11.27 lb) per engine lighter, the SiC-LAS composite liner components cost less than those of the metallic liner. The cost increment was sufficient that the direct operating cost of the aircraft would break even if the life of the composite liner panels was only 76 percent of that of their metallic counterparts.

While of only a preliminary nature, the results of this study have indicated that ceramic composites, and in particular silicon carbide reinforced lithium aluminosilicate, offer significant potential as a material for future aircraft turbine engine combustor liner applications. The limitations of the data available to the study create a mandate for near term research to more rigorously characterize the properties of this and other ceramic composite materials. Particular emphasis should be directed at the definition and quantification of the unique life limiting mechanisms of these materials in high temperature environments, after which verification tests of the composite combustor liner concept should be conducted in high pressure combustor rig tests. While restricted to the specific application to combustor liners, the results of this study have reiterated observations that ceramic composite materials have unique properties including low density, high fracture toughness and thermal and mechanical fatigue resistance that can also be exploited in other high temperature engine components.

SECTION 2.0

INTRODUCTION

As the maximum cycle temperatures of aircraft gas turbine engines increase in response to demands for increased efficiency, improved durability of the combustor structure becomes increasingly important because it affects the basic structural integrity, maintenance cost, and overall performance of the engine. Current louvered liners, of either sheet metal or rolled ring constructions, will not be capable of meeting the increasingly severe design goals for engine combustors introduced in the late 1980's time period. Achieving these more rigorous goals will dictate the need for segmented liner constructions. Even though the segmented liner concept offers substantial advantages, the use of nickel base alloys containing chromium and cobalt to fabricate high temperature components will impose significant limitations due to high material and fabrication cost, potentially limited material availability, high material density (weight), and the continuing need for substantial amounts of cooling air to permit these metals to survive in the hot combustor environment. However, several high temperature advanced composite materials are being developed by various research groups and appear to offer the potential of overcoming some of the difficulties associated with metallic combustor liner materials.

The objective of the Advanced Composite Combustor Structural Concepts Program was to conduct a preliminary design and evaluation study of an advanced combustor liner structural concept using high temperature composite materials. A benefit assessment of the advanced design was conducted to establish the viability of the use of composite combustor structures and lead to definition of the required technology development effort.

The technical effort on this program was conducted in four distinct tasks:

Task I - Baseline Combustor Design

Under this task a reference combustor liner configuration was established, using late 1980's performance criteria and conventional metallic materials. The design was established in sufficient detail to permit definition of combustor liner operational requirements. Detailed structural analyses were conducted to identify component life and failure modes for a typical commercial engine flight cycle.

Task II - Advanced Combustor Concept Screening

This task involved the definition and screening of various design concepts and high temperature composite materials for an advanced combustor liner. Deficiencies in the available data on the material properties of SiC-LAS composites were identified and limited laboratory scale tests were conducted to evaluate the most critical of these properties.

Task III - Advanced Combustor Liner Design

Based on the conceptual definition established in Task II, the initial design of the advanced composite combustor liner was generated. Detailed thermal and structural analyses were conducted to assess the structural integrity of this configuration.

Task IV - Benefit Assessment

This task provided an economic benefit assessment of the advanced composite combustor liner relative to the reference metallic segment liner defined in Task I.

The results of this study indicate that the incorporation of high temperature ceramic composites, such as SiC-LAS (silicon carbide reinforced lithium aluminosilicate), in combustor liners requires unique design approaches because of the thermal properties of these materials. However, liners constructed of ceramic composites are projected to be lighter, less costly to fabricate and less dependent on strategic materials than their metallic counterparts with comparable operational capability.

SECTION 3.0

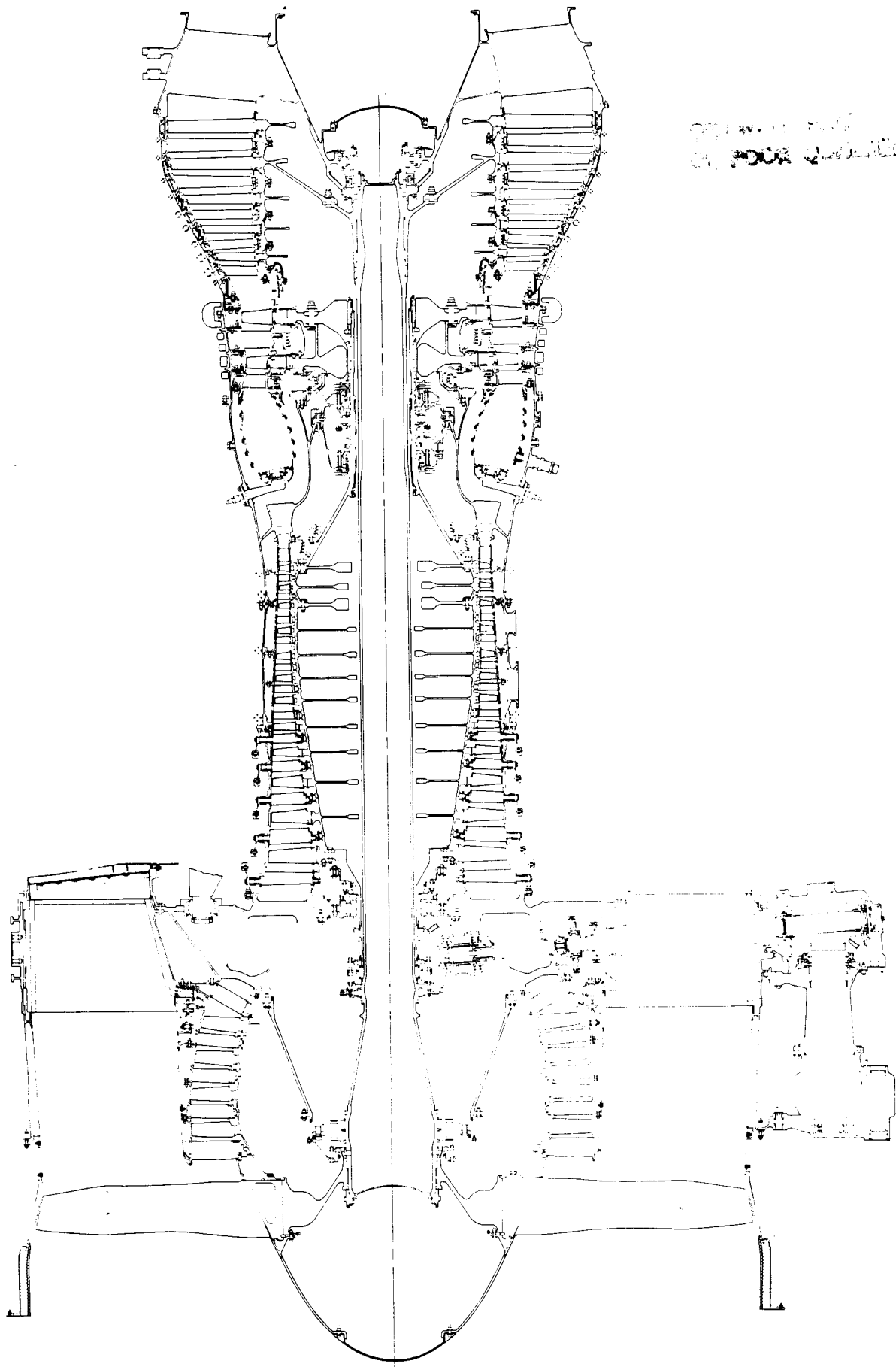
DEFINITION OF COMBUSTOR REQUIREMENTS

The objective of the Advanced Composite Combustor Structural Concepts Program was to provide an assessment of the feasibility of the use of advanced composite materials in the construction of the combustors for aircraft turbine engines. The assessment involved evaluation of metallic and composite combustor structures in a late 1980's high bypass ratio commercial aircraft engine application. To accomplish this evaluation, requirements for the durability of the combustor structure and the impact of its design on overall engine performance had to be defined. Likewise, the operating environment of the combustor in a representative late 1980's engine had to be established to provide the basis for thermal and structural analyses.

3.1 Reference Engine and Combustor

The PW2037 engine was selected as the reference engine for this study. The PW2037 is the first of a new generation of advanced technology turbofan engines that powers the Boeing 757 aircraft and meets the requirements of a wide spectrum of commercial and military aircraft through the remainder of this century. Figure 3-1 shows a cross section of the PW2037 which is a twin-spool, five bearing, axial flow, high bypass ratio turbofan engine. It incorporates multistage compressors and a fan driven by a multistage reaction turbine designed for operation with fixed area nozzles for primary and fan discharge. The engine employs a single-stage fan while the low-pressure compressor consists of four compression stages. The high-pressure compressor is a twelve-stage compression system with variable geometry in the first five stages. A two-stage high-pressure turbine and a five-stage low-pressure turbine are employed. The combustor is annular in design, and the liner in the current configuration of this engine has a burning length of 22.8 cm (9.0 in) between the fuel injector face and the leading edge of the turbine inlet guide vane. The liner is film cooled using an advanced rolled ring louver construction, and the twenty-four single pipe aerating fuel injectors are externally removable from the engine case.

However, advanced models of the PW2037 which will enter service in the late 1980s are expected to include, in addition to further improvements in component efficiencies, several new technology concepts in the combustor section. To maintain consistency with the engines of the late 1980 time period, the reference combustor for this study also incorporated these features. In particular, rather than the conventional combustor shown in Figure 3-1 and described above, the late 1980's model of the PW2037 engine is expected to incorporate an advanced technology combustion system that has been under development at Pratt & Whitney. It is an outgrowth of the Vorbix combustor concept that was evolved and demonstrated under the National Aeronautics and Space Administration/Pratt & Whitney Experimental Clean Combustor and Energy Efficient Engine programs (References 1 through 4). Figure 3-2 shows this concept as it would be incorporated in the burner section of advanced models of the PW2037 engine.



Copyright © 1997
by Lockheed Martin

Figure 3-1 Cross Section of the PW2037 Reference Engine (J27676-1)

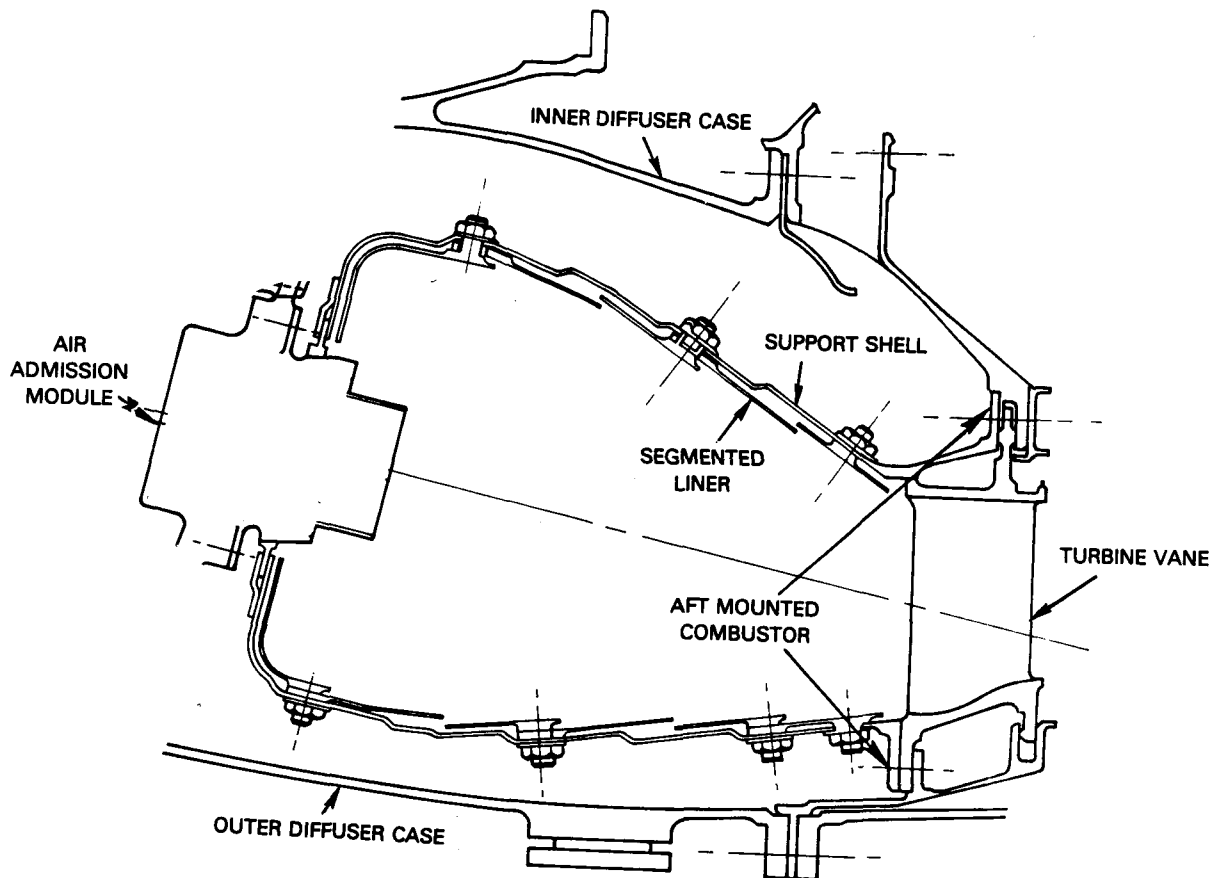


Figure 3-2 Advanced Technology Combustor in PW2037

Another advanced technology feature incorporated in the combustor of the late 1980's engine is a segmented liner. The conventional combustor shown in the current model of the PW2037 engine employs a single piece or "full hoop liner" which can be severely strained to maintain compatibility between the thermal growth of the hot and cold sides. The high metal temperature results in plastic and creep damage, leading to relatively low creep-fatigue life. Segmenting the liner (i.e., the surfaces exposed to the hot combustion products are divided into a number of circumferentially and axial separate pieces attached to a common cold side shell) can relieve these thermal stresses and result in a much improved low cycle fatigue life. Another advantage of the segmented liner is that the fatigue strain is lower, allowing use of less ductile, high creep strength materials. The use of cast metallic materials permits forming intricate shapes required for sophisticated cooling schemes, casting being relatively inexpensive. In addition, combustor field maintenance will be easier and less expensive because the panels can be replaced individually if distorted or cracked; whereas present single-piece liners require repair by welding.

Further details on the specific segmented liner construction employed in the reference combustor for this study are provided in Section 4.0.

3.2 Combustor Operating Environment

The thermal and mechanical loading on the combustor components are dictated by the combustor inlet, i.e., compressor discharge, total pressure and total temperature, and the temperature of the combustion products inside the combustor liner proper. The latter is readily associated with the average combustor exit total temperature. Aerodynamic and thermal analyses are used to relate the temperature distribution in and pressure loads on the combustor components to these three readily defined engine operating parameters.

Figure 3-3 shows a typical flight profile for a 90-minute commercial aircraft mission and lists the engine operating modes at key points during the flight. Based on the performance of the PW2037 engine, histories of the combustor inlet and exit total temperature have been constructed and are shown on Figure 3-4. This figure also demonstrates the corresponding history of the local combustor liner metal temperature during this flight. From the point of view of selecting critical structural design points, the pressure loading on combustor components is highest at takeoff. Likewise, maximum combustor inlet and exit temperature occur at this condition. Consequently, the takeoff condition is critical to the analysis of maximum loading and cyclic fatigue phenomena. From Figure 3-4 it is evident that the combustor components are exposed to gas temperatures corresponding to combustor exit temperatures above 1093°K (2000°F) for more than two-thirds of the mission duration. Failure modes that are dependent on time at temperature, such as oxidation, would be expected to respond to a time weighting of the temperature history over the takeoff-climb-cruise portion of the flight for which the "begin cruise" condition would be representative.

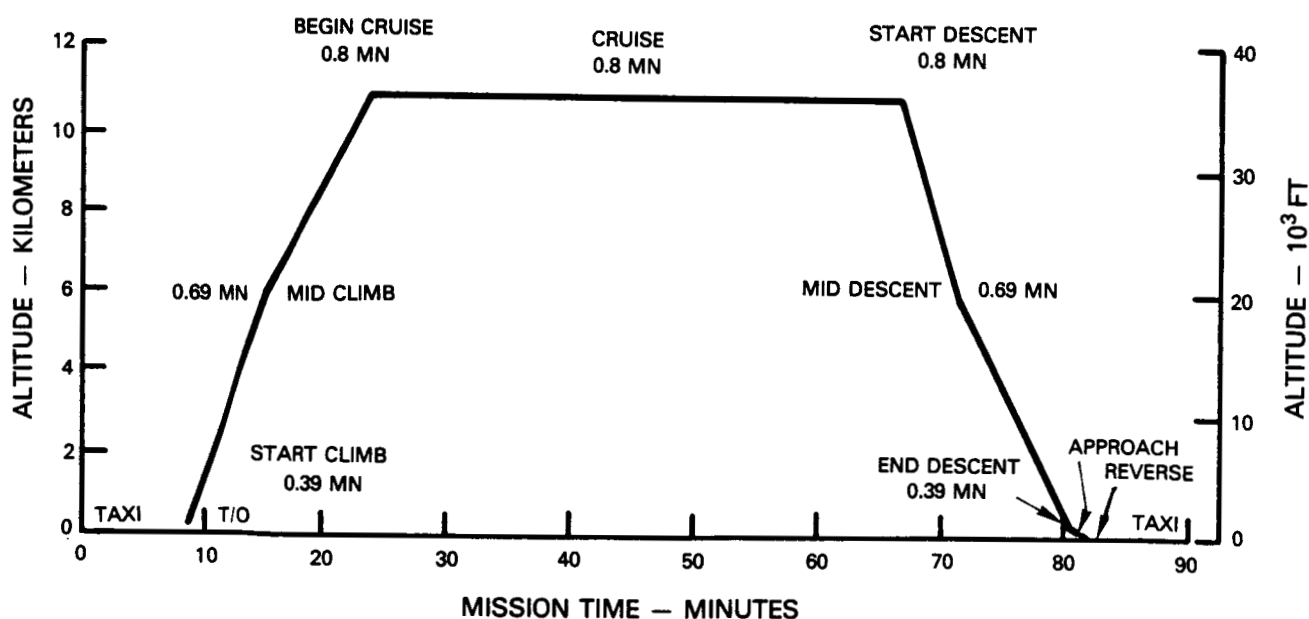


Figure 3-3 Typical 90-Minute Flight for a PW2037 Engine

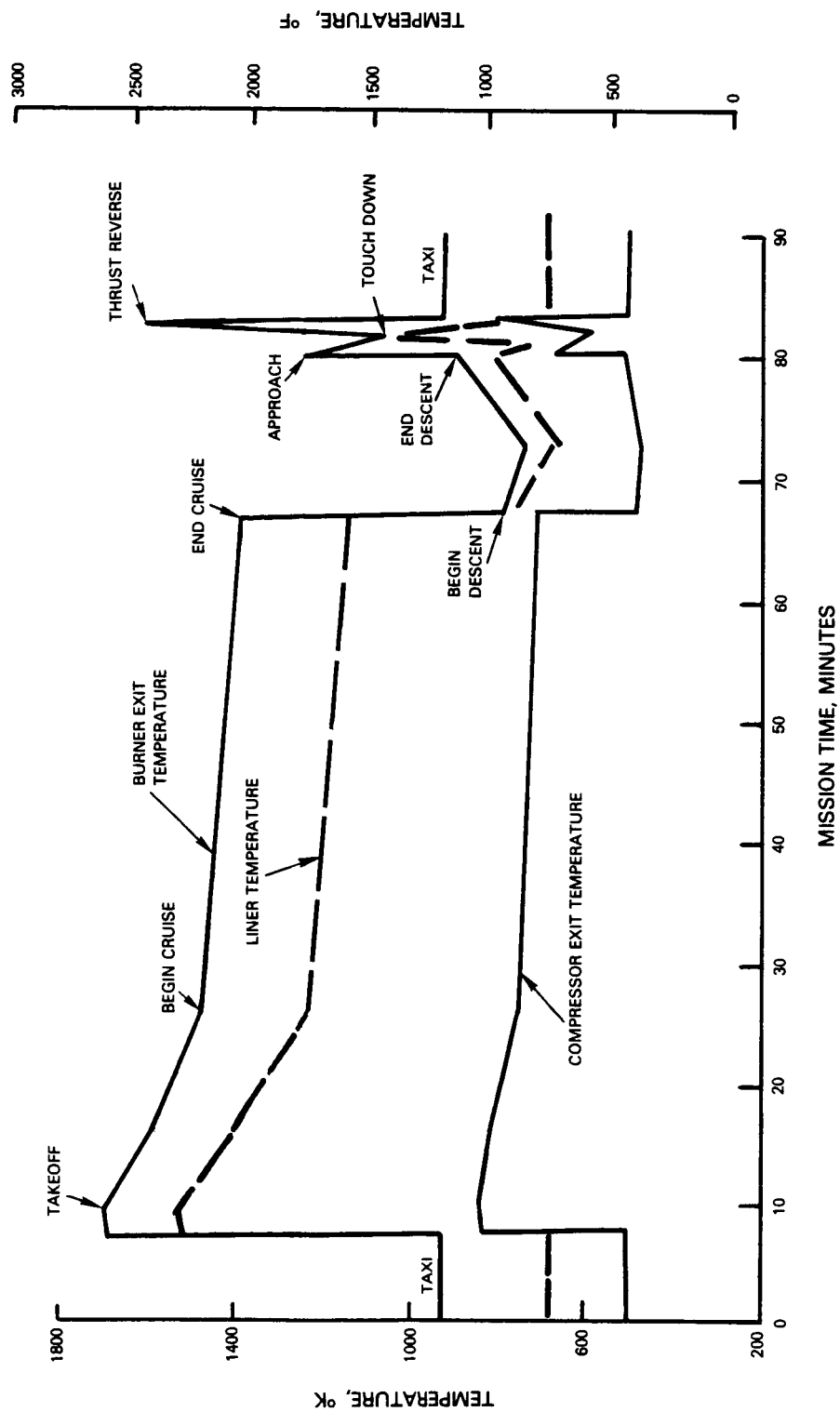


Figure 3-4 Combustor Temperature History During a Typical 90-Minute Flight

Table 3-I lists the above cited combustor operating parameters at the takeoff and beginning of cruise condition that were used for the design of the combustors under this program. The values listed were established on the basis of the performance of the current PW2037, projected improvements in its performance in the late 1980's models and margins for nonstandard ambient air temperature.

Table 3-I
Combustor Operating Conditions

	<u>Sea Level Takeoff</u>	<u>Begin Cruise M=0.8 10.67 km (35,000 ft)</u>
Combustor Inlet Total Temperature, °C (°F)	565 (1050)	445 (833)
Combustor Exit Total Temperature, °C (°F)	1425 (2600)	1187 (2170)
Combustor Inlet Total Pressure, MPa (psia)	2.758 (400)	1.117 (162)

The analysis of vibration of the combustor structure requires definition of the maximum high rotor speed of the engine so that resonance with the natural frequencies of the structures may be avoided. The maximum high rotor speed of the late 1980's model of the PW2037 engine is expected to be 11,900 rpm and will occur at low altitude high power operation with below standard ambient air temperatures.

3.3 Combustor Life and Performance Requirements

From a structural design viewpoint the most significant combustor performance requirement is the life of the combustor liner. To be consistent with anticipated engine overhaul schedules, the target life of the combustor liners designed under this study was a 7,500 hour B-5 life, i.e., no more than 5 percent of the combustor liners will fail during this interval. This goal was selected to be consistent with the projected service life of other components so that combustor repairs would not solely dictate the need for engine removal for overhaul. This life is equivalent to a B-50 life of 15,000 hours (i.e., no more than 50 percent of the combustor liners will fail during this interval). For liners that are cyclic fatigue limited, the B-50 life corresponds to 10,000 ambient to maximum temperature cycles based on a typical 90-minute flight.

The mode of failure of the combustor liner must also be benign in that it should not cause impact damage to downstream components. Anticipating the use of segmented liner constructions, this requirement dictates the need for a degree of redundancy and minimal design risks in the segment attachment areas.

To meet design requirements for the late 1980's PW2037 engine, the pressure drop across the combustor liner must be limited to two and one-half percent of the combustor inlet total pressure. This drop is the static-to-static pressure differential from the burner shroud passages to the gaspath of the combustor and includes the losses across both the burner shell and any extended surfaces on the cold side of the liner segments. This restriction limits the attainable cooling air velocity and hence the convective heat transfer capability of these surfaces.

A third combustor performance "requirement" is the incentive to restrict the quantity of air used to cool the combustor liner. The ability to minimize the output of undesirable combustion byproducts as emissions or smoke and to control the gas temperature distribution at the combustor exit for maximum turbine airfoil life is dependent on large quantities of air for combustion and mixing purposes. The use of excessive fractions of the available air for cooling of the liner compromises the ability to achieve these performance goals. Obviously, a stringent limit on the quantity of liner cooling air cannot be established a priori, but differences in the cooling air demands of a composite as opposed to metallic combustor construction must be recognized in the final Cost-Benefit Analysis. To this end, the design of both liners included a comprehensive thermal analysis to establish the quantity of cooling air required to maintain the particular liner at a selected maximum temperature consistent with its material properties and the expected life.

SECTION 4.0

ANALYSIS OF REFERENCE METALLIC COMBUSTOR LINER

A reference metallic combustor liner representative of late 1980's technology was defined and analyzed to provide a basis for comparison with the design of liners using the composite materials. The analysis, which addressed thermal and static and dynamic structural aspects, demonstrated that this reference liner met all of the design requirements and constraints of Section 3.0.

4.1 Metallic Liner Configuration

Figure 4-1 shows the segmented liner construction that was selected as the reference for this study. The liner consists of panels or segments about 40 mm (1.5 in) in length and subtending an arc of 30° in the circumferential direction. The segments have a nominal thickness of 0.76 mm (0.030 in) and are cast from a high creep strength alloy normally used for turbine airfoils. The segments are attached to a 1.14 mm (0.045 in) thick Hastelloy X shell by either two or three integrally cast attachment studs. As shown on Figure 4-1, the position of the attachment studs is staggered circumferentially to avoid exposing all of the studs to a hot streak. Redundancy is also provided by the lugs on the rear of each segment which are retained by the stud on the upstream panel to produce effectively five attachment locations per segment. The attachment studs constrain the segments radially, but they are sufficiently free to move in the axial and circumferential directions to accommodate thermal expansion differences.

Pin-fin extended heat transfer surfaces are cast on the cold side surface of the segment and cooling is accomplished by introducing cooling air through circumferentially extending rows of holes in the Hastelloy X support shell. The flow of cooling air is over the pin-fin surface after which it is discharged to form a film on the hot side surface of the segment.

Several candidate materials were considered for the segments, including INCO-713, Waspalloy[®], and a modified B-1900 alloy. Table 4-1 compares the physical properties of these three materials at 988°C (1800°F). Modified B-1900 was selected because of its higher creep strength, yield strength, and ultimate strength. The availability of data on fatigue strength and crack propagation rate was also a consideration.

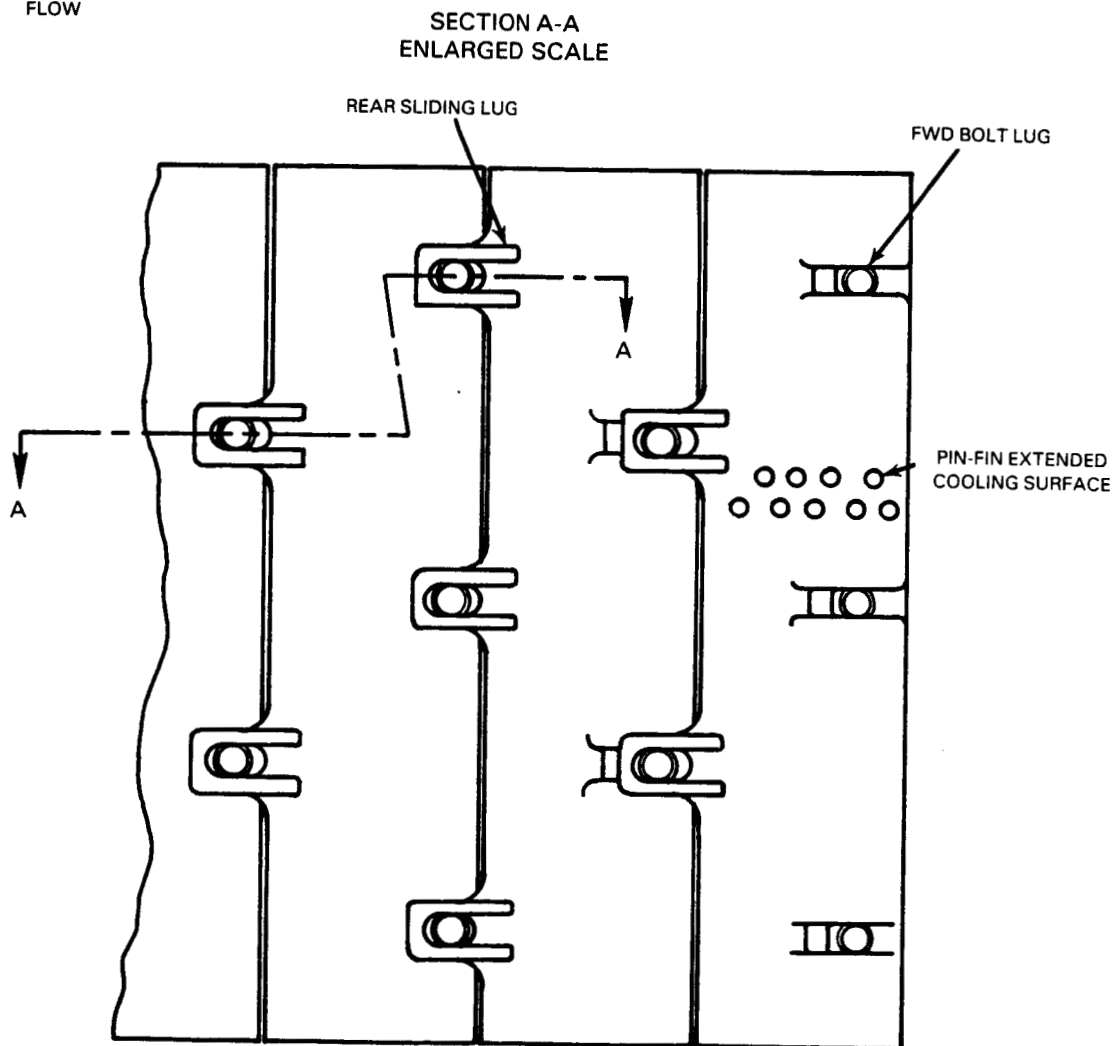
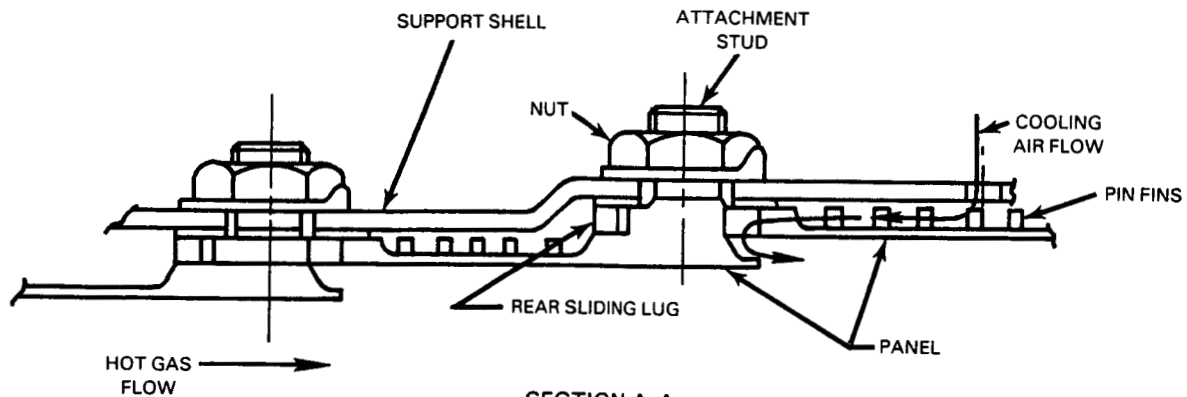


Figure 4-1 Baseline Segmented Liner Concept

Table 4-I

Comparison of Combustor Segment Material at 988°C (1800°F)

<u>Material Property</u>	<u>Modified B-1900</u>	<u>INCO-713</u>	<u>Waspalloy®</u>
Coefficient of Expansion x 10 ⁻⁶ per °C (°F)	15.66 (8.7)	16.56 (9.2)	17.10 (9.5)
Creep Strength MPa (ksi) to produce 1% strain in 10 hours	160 (23)	125 (18)	51 (7.5)
Thermal Mechanical Fatigue Cycle I - 0.3%Δε Compressive when hot	(Typical) 4000 Cycles	Not Available	Not Available
Cycle II - 0.3%Δε Tensile when hot	(Typical) 8000 Cycles	Not Available	Not Available
Yield Strength MPa (ksi) at 0.2%	313 (45)	174 (25)	236 (34)
Ultimate Strength MPa (ksi)	376 (54)	264 (38)	264 (38)
Crack Growth Rate at ΔKε = 10 ⁻³ √in cm(in)/cycle	20.3 (8) X 10 ⁻⁵	Not Available	Not Available

4.2 Thermal Analysis

With the definition of the baseline metallic liner established, the design study was initiated with a thermal analysis of the combustor. An existing computer program was used for this analysis which consisted of conducting local energy balances on elements of the liner segment to define temperature distribution. The energy balance included internal conduction, convective and radiant heat input from the combustion gases, convective cooling of the rear face of the segment, including the extended-surface effects produced by the pin-fins, and similar modes of heat transfer to and from the shell. The analysis was based on a typical segment near the front of the combustor where heat loads are highest. It was recognized that circumferentially spaced hot streaks would occur in the combustion products and that these would be associated with the richer and more intensive burning regions downstream of the 24 air admission modules on the combustor. A maximum metal temperature of 1049°C (1920°F) was stipulated in these high temperature streak regions and this condition was expected to be encountered at the takeoff operating condition. The thermal analysis established the temperature distribution in the segment consistent with this maximum hot-spot temperature criteria and defined the quantity of air required to cool the liner. The results of this analysis indicated that a total of 20.54 percent of the combustor airflow would be required for liner cooling with this being split 7.62 percent and 12.92 percent respectively for the inner and the outer liner including the adjacent surfaces on the front bulkhead of the combustor.

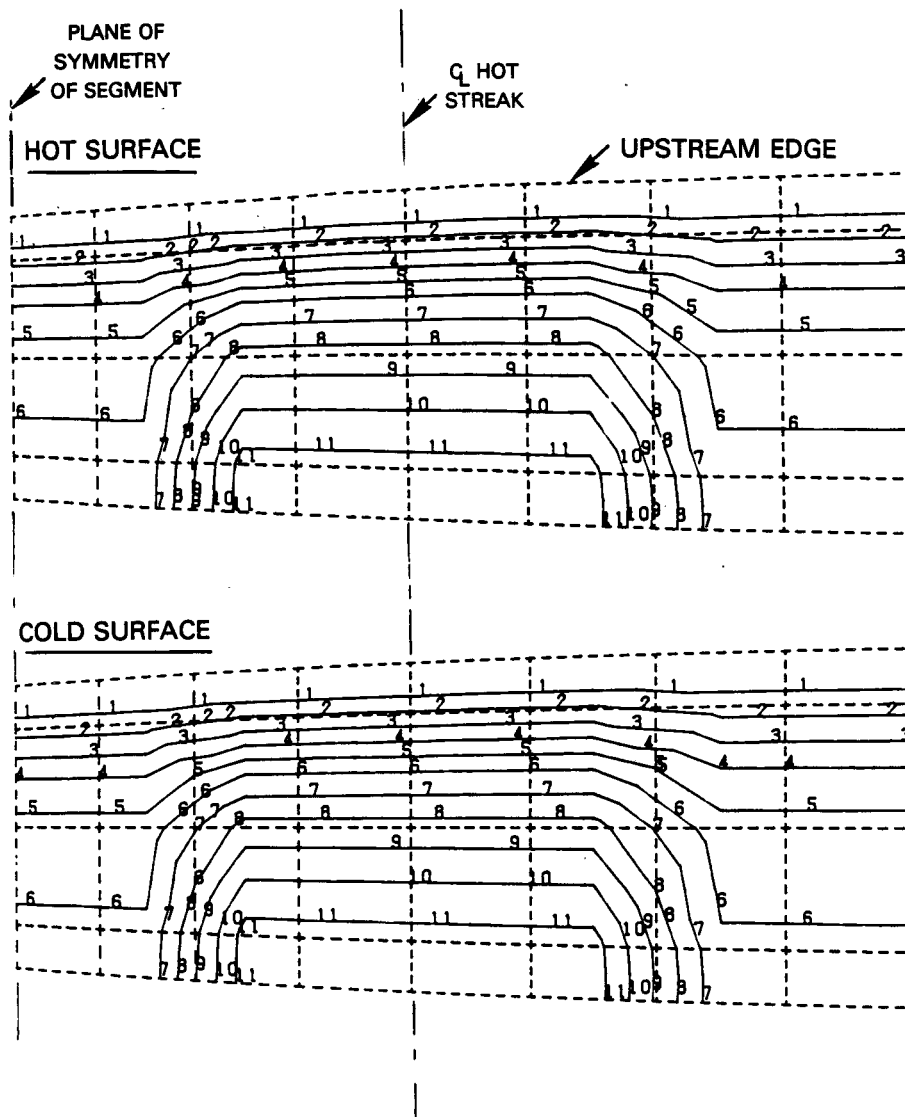
Figure 4-2 shows the computed temperature distribution on the hot and cold side surfaces of the inner liner segment at the takeoff operating condition. High temperature streaks are associated with each air admission module and with the segments having a circumferential width equivalent to twice the module spacing; the temperature distribution is symmetrical with respect to the center of the segment. Consequently, this figure only shows the temperature distribution in half the segment. (While the surface of the segment is actually a sector of a cylinder or a frustrum of a cone and would be expected to appear as a quasi rectangular shape in this figure, it appears tapered because the computer-generated "view" is from an angle and includes built-in perspective. This also occurs in subsequent figures in this section.) The dominant feature of the temperature distribution in the segment is the high temperature streak region. On the hot surface of the panel the stipulated maximum temperature of 1049°C (1920°F) occurs at the downstream end of the panel and is more than 83°C (150°F) higher than the 968°C (1775°F) circumferential average temperature at this end of the panel.

The temperature distribution on the cold side surface of the panel closely parallels that of the hot surface. The highly effective cooling of the cold side by the extended surface pin-fins lead to high heat flow through the metal segment and, hence, significant through thickness temperature gradients in the metal. The average temperature differential across the 0.76 mm (0.030 in) thick segment at the downstream end of the segment is about 25°C (45°F), but it reaches a peak of nearly 55°C (100°F) at the maximum temperature location at the center of the streak.

The results of the thermal analysis indicated that the heat load on the support shell behind the liner segments was low and its temperature was less than 55°C (100°F) above the combustor inlet air temperature of 838°K (1050°F) at the takeoff condition. There were no significant nonuniformities in this temperature distribution that would be cause for concern over thermal stresses in this component of the liner.

4.3 Static Stress Analysis

A detailed nonlinear stress analysis was conducted of the combined segment and shell using the MARC computer program (Reference 5). The domain of the analysis included two axially adjacent segments of the inner liner and the underlying sector of the shell as shown on Figure 4-3. This allowed evaluation of segments with both three and two attachments at the downstream end. As in the case of the thermal analysis, because of symmetry of the thermal profiles and loading on the segment and shell, only half the circumferential width of the segment was modeled. Each segment has five attachments to the shell which were modeled as lugs attached to the segment and are capable of transmitting radial loads, but were unconstrained and free to translate axially and transversely relative to the shell.



TEMPERATURES

HOT SURFACE			COLD SURFACE		
	°C	°F		°C	°F
1 =	664	1230	1 =	664	1230
2 =	703	1300	2 =	697	1290
3 =	742	1370	3 =	731	1350
4 =	781	1440	4 =	764	1410
5 =	823	1510	5 =	793	1470
6 =	853	1570	6 =	836	1520
7 =	892	1640	7 =	869	1580
8 =	931	1710	8 =	903	1640
9 =	970	1780	9 =	936	1700
10 =	1009	1850	10 =	969	1760
11 =	1047	1920	11 =	992	1820

Figure 4-2 Temperature Distributions in the Metallic Liner Segments

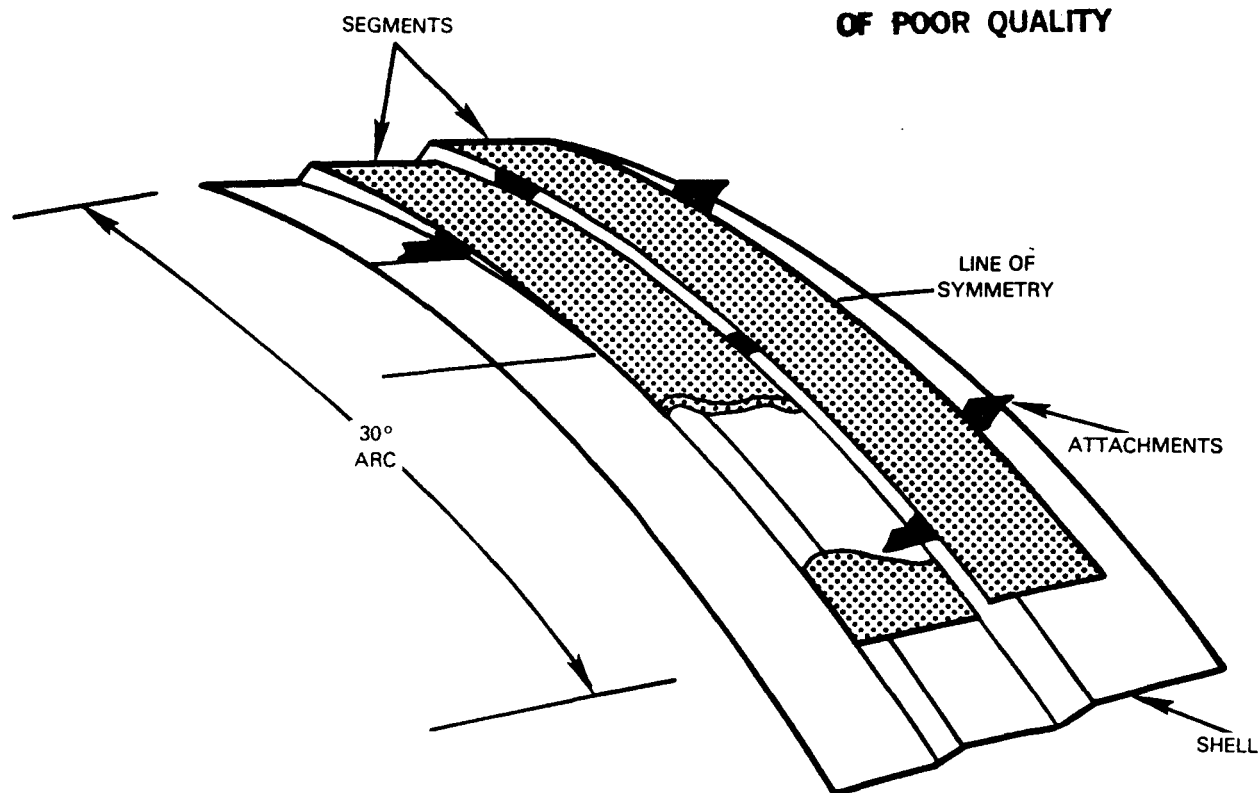


Figure 4-3 Domain of Static Structural Analysis of Liner

Figure 4-4 shows the finite element breakup of the segment and the shell. Smaller elements were incorporated in the areas of anticipated large variations in load and stresses including the attachment and step areas of the shell and the upstream and downstream ends of the segments. The curved quadrilateral thick shell Mark Element 22 was used for the analysis. It is a superparametric element obtained by degeneration of the 20-noded isoparametric solid element. The element-22 has eight nodes in each model element with five degrees (three displacements and two rotations) of freedom. The in-plane displacements are interpolated bi-quadratically in the middle surface from their values at the eight corner nodes. In the third direction (i.e., through the thickness) a linear displacement variation is incorporated.

The stress analysis was conducted by numerically subjecting the initially cold and stress-free liner to the temperature distribution and pressure loadings encountered at the takeoff condition. The material was allowed to creep for an equivalent of fifty hours, more than sufficient time to characterize the creep strain versus time response that would be required for subsequent life analysis.

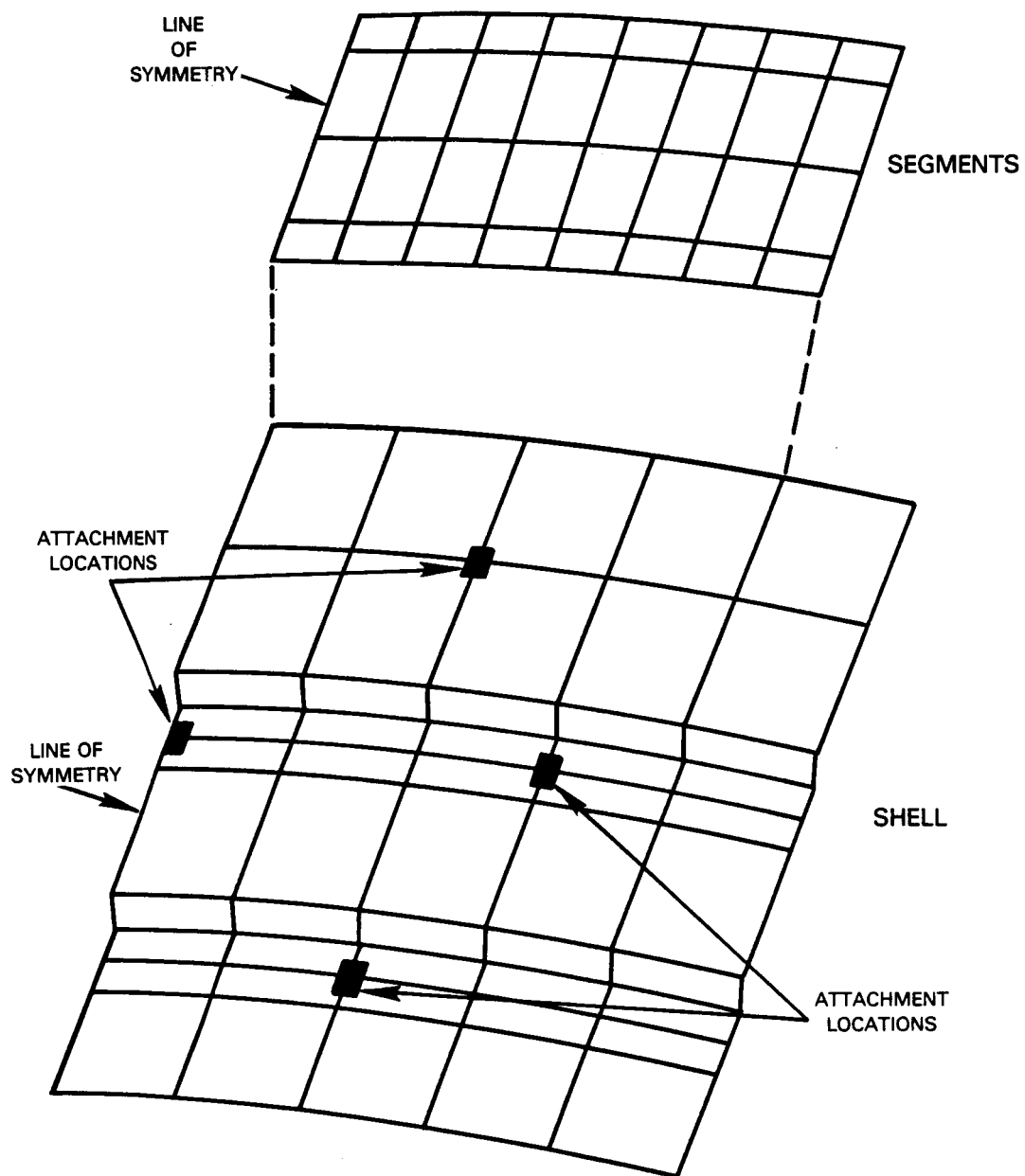


Figure 4-4 Finite Element Breakup of Liner for Static Structural Analysis

Figure 4-5 shows the distribution of the Von Mises stress in the liner segments as computed by the analysis. Distributions are shown for an "upstream" and a "downstream" panel reflecting the difference in attachment locations. These stresses are induced by the combined effect of in-plane thermal gradients, bending loads caused by the pressure differential produced by the cooling air behind the panel and the radially constraining influence of the support shell. The results indicate that the highest stresses occur in two characteristic locations: in the vicinity of the lugs which attach the segment to the shell and, referring back to Figure 4-2, in the regions of high transverse temperature gradients at the edges of the streak regions on the downstream half of the segments. In one location on the upstream panel the attachment and the high temperature gradient region coincide and the highest stress level in a segment, 247 MPa (35.3 ksi), occurs at this point. Since this is less than 80 percent of the 0.2 percent yield strength of the modified B-1900 segment material cited in Table 4-I at these operating temperature levels the loads on the segments are acceptable.

Figure 4-6 shows another result of the nonlinear stress analysis in which the circumferential creep strain distribution is plotted for the hot side surface of the segment after fifty hours. The circumferential component of the strain is critical to the initiation of axial cracks at the downstream end of the segment, which will be the dominant failure mode of this liner. The effect of the location of the attachments of the segment to the shell is also demonstrated by showing the creep strain distribution in the two segment panels that were analyzed. The results presented on this figure in combination with the temperature distributions of Figure 4-2 indicate that the circumferential creep strain is highest at the downstream end of the segment in the regions of steep circumferential temperature gradients near the edge of the high temperature streak, such as locations A, C and D. In the case of a segment with an attachment lug on the downstream end of the panel at the centerline of the hot streak, another region of high creep strain is evident near this attachment, i.e., at location B. The combination of high creep strain and elevated temperatures led to the identification of these regions as the most likely sites for crack initiation. The computed creep strains and metal temperatures at these locations will be used to project crack initiation and subsequent propagation histories at these locations to define the cyclic fatigue life of the segment in Section 4.4.

Stresses are induced in the combustor liner shell by pressure forces and by loads transmitted from the segments through the attachments. Figure 4-7 shows the computed Von Mises stress distribution in the shell from the structural analysis. The maximum computed stress in the shell was 118 MPa (17 ksi) and occurred in the vicinity of one of the segment attachments located on the downstream end of a panel in the streak region. The remaining attachments were also sources of moderately high localized stresses. The high axial thermal gradient in the segment caused a couple to be transmitted to the shell and resulted in higher stresses in the vicinity of the attachments. Even with this local concentration effect, the maximum stress of 118 MPa (17 ksi) in the shell is well below the 0.2 percent yield limit of 200 MPa (30 ksi) for the Hastelloy X shell material, and, hence, is acceptable.

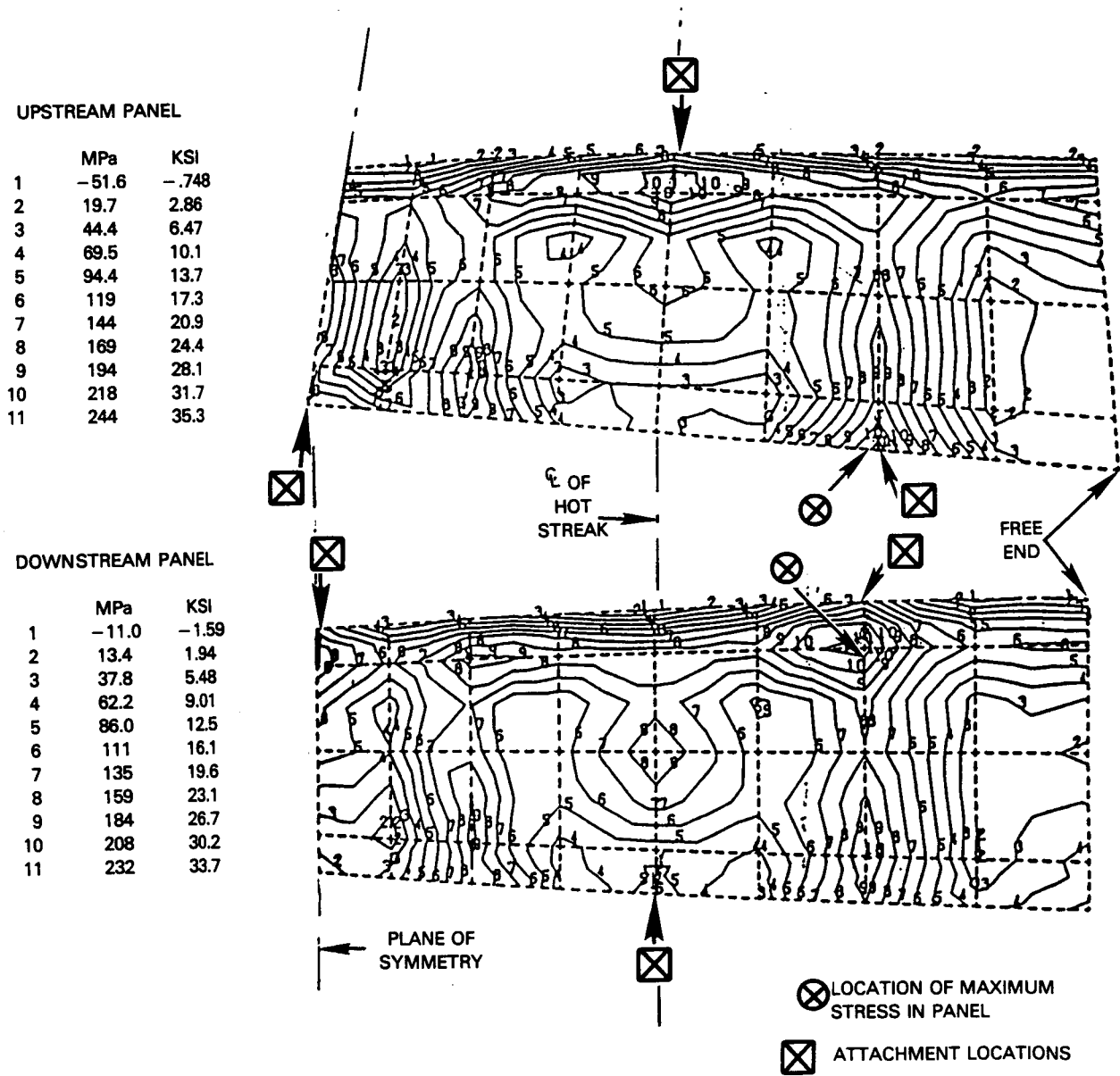


Figure 4-5 Von Mises Stresses in the Metallic Liner Segments

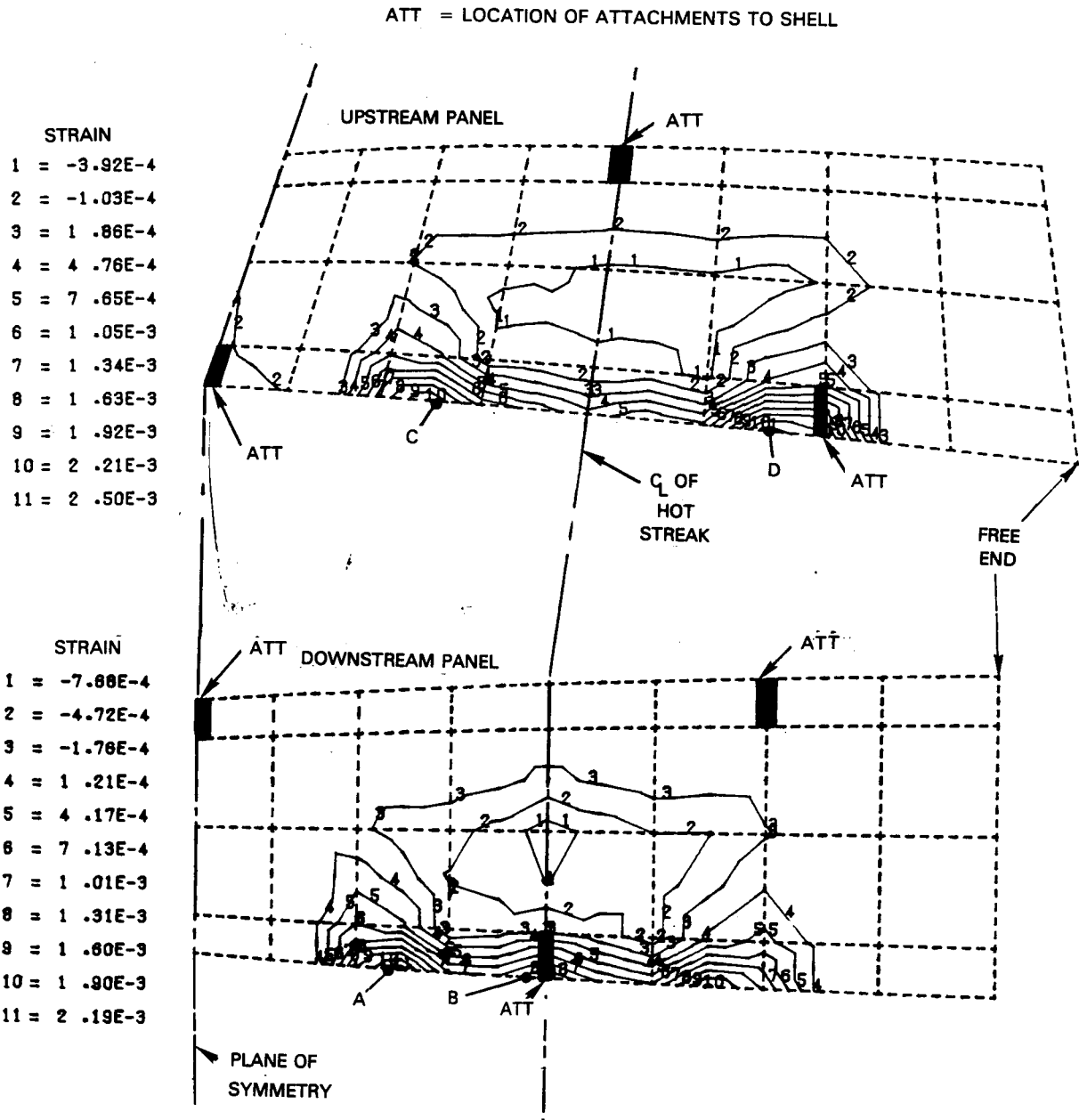
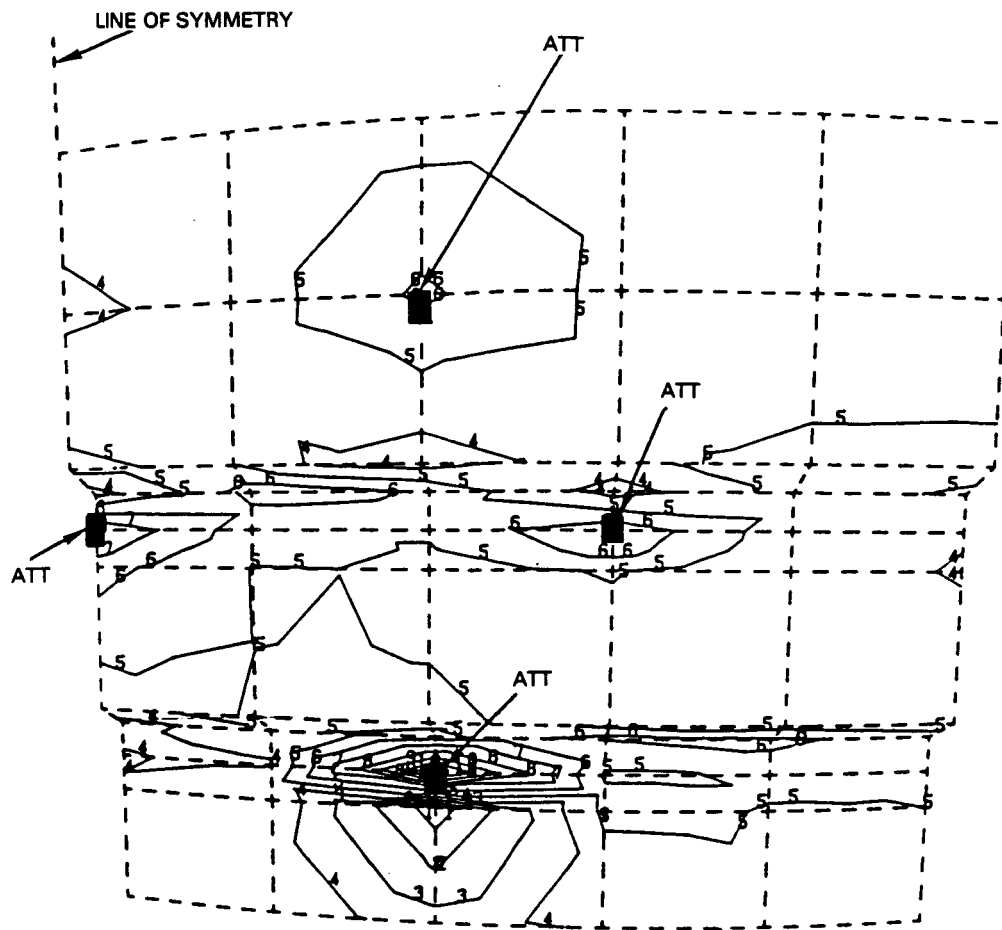


Figure 4-6 Circumferential Creep Strain Distribution at Hot Side Surface of Liner Segments

ATT = SEGMENT ATTACHMENT LOCATIONS



VON MISES STRESS

	MPa	KSI
1 =	-70.3	-10.20
2 =	-51.7	-7.50
3 =	-32.8	-4.75
4 =	-13.9	-2.01
5 =	5.04	0.73
6 =	23.9	3.47
7 =	42.8	6.20
8 =	61.6	8.94
9 =	80.6	11.70
10 =	99.4	14.40
11 =	118.8	17.20

Figure 4-7 Stress Distribution in Liner Shell

Analyses were also conducted to assess the possibility of buckling the shell of the outer combustor liner. There is a 2.5 percent, or equivalently a 0.07 Pa (10.5 psi) pressure drop across the liner to provide cooling air to the combustor liner. In conventional liners, the average temperature of the outer liner is high and time-dependent creep buckling can occur. The temperature of the shell of a segmented liner, however, is moderate and creep buckling is not a significant factor. Only elastic buckling need be considered and an analysis using an axisymmetric shell model indicated that a factor of safety of about 5.0 was available relative to the loading at which buckling would occur.

4.4 Cyclic Fatigue Life Analysis

With the stress levels in the liner segments and shells found to be moderate with respect to the carrying capacity of the selected materials, it was evident that crack growth through cyclic fatigue of the segments could be the dominant failure mechanism for the reference metallic combustor liner. After determining the critical sections in the segments from the temperature and creep strain distributions of Figures 4-2 and 4-6, the number of thermal cycles prior to crack initiation was estimated. The "strain range partitioning" method has been used for predicting crack initiation in ductile materials like Hastelloy X. However, the "ductility exhaustion approach" is more appropriate for relatively less ductile materials like Modified B-1900. This approach is based on the concept that materials have limited ductility and that failures occur when ductility is depleted. To account for creep-fatigue interaction, it is assumed that a decrement in available ductility resulting from a period of cycling could be represented directly as an increment of creep extension. The scheme for accumulating ductility decrement from such cycling and creep to the point where the initially available ductility is exhausted can be visualized as a stepwise progression of creep strain as a function of time.

The information from the stress analysis was used to calculate crack initiation life for the PW2037 design mission of 1.5 hours described in Section 3.0. Life was estimated for critical locations A through D on Figure 4-6 where creep strain and temperature were high. Calculated number-of-cycles-to-crack-initiation are listed on Table 4-II. The minimum crack initiation life is at the edge of the streak region of the panel with an attachment in the center of the streak where a crack would form in about 6,305 cycles.

Table 4-II

Number of Engine Cycles to Crack Initiation
at High Strain Locations on Segments

<u>Location on Figure 4-6</u>	<u>Cycles to Crack Initiation</u>
A	6,305
B	14,142
C	21,893
D	9,877

An elastic fracture mechanics analysis was used to compute the crack growth. The analysis was conducted based on an assumed initial crack length of 0.254 mm (0.010 in). The analysis used an edge crack model, and the stress field as a function of axial length was obtained from the MARC stress analysis output. The crack growth data for Modified B-1900 from Table 4-I were also input. Given this information, the Elastic Fracture Mechanics program calculated life from an initial flaw size to the final size.

The analysis indicated that a crack in the most critical region, i.e., location A of Figure 4-6, would grow to 6.6 mm (0.26 in) in 3,700 thermal cycles after crack initiation. This means that the segment would have one crack of about 6.6 mm (0.26 in) after the liner had been exposed to the program goal of 10,000 cycles. The total length of the panel is 35.6 mm (1.4 in). Since a crack of this length should not compromise integrity, it was concluded that the baseline metallic liner segment met the program life goal of 10,000 thermal or flight cycles.

4.5 Segment Oxidation Life

An estimate was made of the oxidation life of the liner segments based on available data on the rate of oxidation of Modified B-1900. The estimate was made by assuming that the 1.5 hour mission of Figure 3-4 could be represented by 1.5 minutes of operation at takeoff power level and the remainder at the cruise condition. This is a conservative assumption because the total mission also includes descent and idling time when the metal temperature is not as high as it is during cruise operation. Analysis indicated that in the local hot spots, where the metal temperature is 1049°C (1920°F) at takeoff and 880°C (1618°F) during cruise, a total of 0.285 mm (0.0112 in) of segment material or about 37 percent of the total segment thickness would be removed by oxidation over the 15,000 hour goal life of the segments. Using the same assumptions to predict oxidation effects in nonstreak regions, a total of 0.178 mm (0.007 in) of material would be removed. If this depletion rate were found to be excessive, the segments could be coated with oxidation retardation coating. Analysis indicates that a 0.076 mm (0.003 in) thick layer of NiCrAlY coating would survive the 15,000 hour design life of the segments. The need for coating the segments for oxidation resistance is seen at this point in the design to be marginal. Local material depletions to 37 percent are predicted and could cause additional stress risers in these areas. As will be shown in Section 8.0, the decision to coat the metallic segments is a significant factor in the overall cost-benefit assessment.

4.6 Dynamic Analysis of the Liner

Vibration of the panels itself is a concern in the design of segmented liners. To avoid this, the criteria that the natural frequency of the segments be at least higher than the maximum high rotor speed was established in order to avoid excitation by rotor imbalance. Panel mode frequency is a function of segment thickness, panel size, pin-fin weight, and the location and number of attachments. The NASTRAN computer program (Reference 6) with Quad 4 elements was used for the modal analysis. While a half segment was modeled for the static analysis, one entire 30-degree transverse width segment was modeled for this analysis in order to include all possible vibration modes. The pin-fins

that add weight but not bending stiffness were accounted for by adjusting the density of the material. The segment was radially constrained to the shell at the attachments, and sliding was assumed not to take place.

The analysis indicated that the fundamental natural frequency of the baseline segment of Modified B-1900 and mounted on the Hastelloy X shell was 484 Hz, which is slightly above the second harmonic of the maximum high rotor speed. The fundamental mode was a radial "flapping" of the portion of the panel outboard of the last attachment lug, as shown in Figure 4-8. Since the frequency of this oscillation is well in excess of the 220 Hz maximum high rotor rotational speed, it was concluded that when properly restrained the segment would not be excited in a damaging vibratory mode.

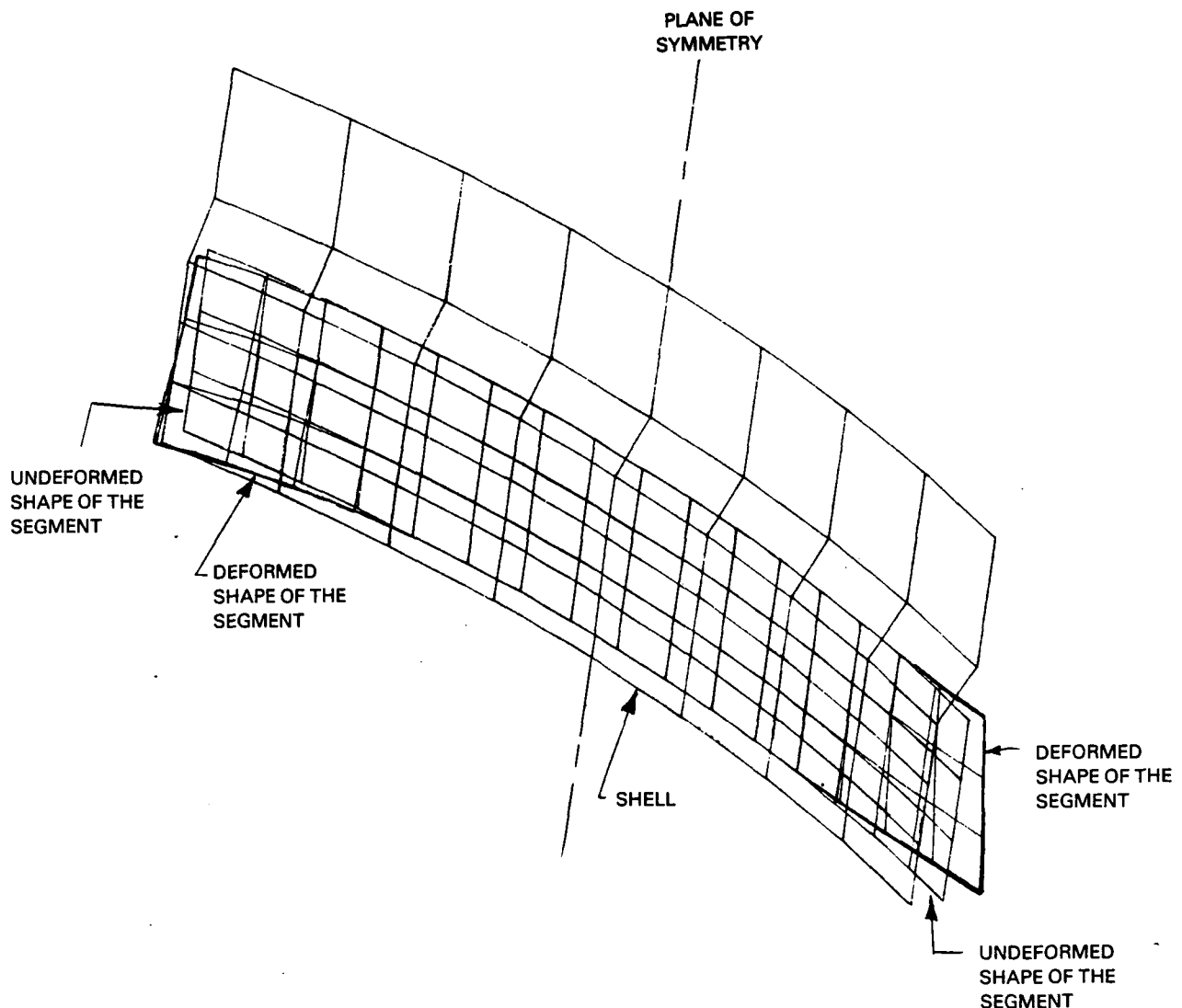


Figure 4-8 Flap Mode of Vibration of the Liner Shell

Modal analyses of the liner shell were conducted using a generalized shell analysis computer program. The program provides basic capability for linear elastic analysis of axisymmetric structures, which can be modeled as a collection of thin shells of revolution. The combustor was aft mounted with the shell cantilevered from the turbine inlet case and the weight of the segments was accounted for by adjusting the density of the material. The fundamental frequency was calculated to be 850 Hz at which the bulkhead bulges in and out axially as shown in greatly exaggerated form in Figure 4-9. This natural frequency is more than four times the maximum high rotor speed of the PW2037 engine and was judged to provide adequate margin from the usual excitation sources.

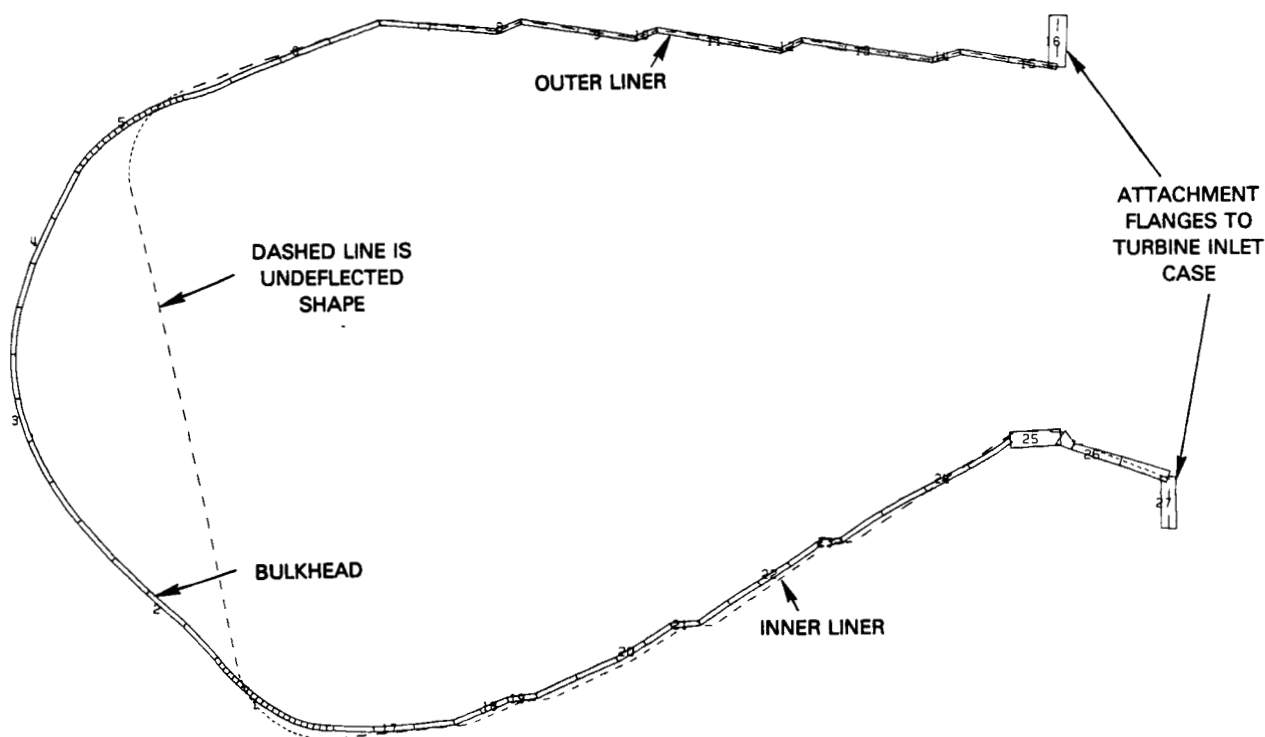


Figure 4-9 Mode Shape of the Combustor Liner Shell

4.7 Summation

On completion of the analysis of the baseline metallic liner it was concluded that this configuration is an aggressive design which exploits the most advanced metallic liner technology expected to be available in the late 1980s and meets the program goals for combustor performance and durability. As such it is a realistic and challenging reference for evaluating the potential of the composite combustor liner concept.

SECTION 5.0

SURVEY OF HIGH TEMPERATURE COMPOSITE MATERIALS

The definition and evaluation of the advanced composite combustor liner was initiated with a survey of available high temperature composite materials. Following identification of candidate composite materials, a literature survey was conducted to define comparable property data. The materials were screened and ranked on the basis of the most critical properties to select the best material for near term application in the combustor liner application.

5.1 Candidate Composite Materials

Three different types of high temperature composites were identified in the survey as potential combustor liner materials:

- o Fiber Reinforced Glass Ceramic

Glass ceramic materials have been recognized extensively for the capability of withstanding elevated temperatures but have the inherent liability of inadequate fracture toughness to withstand shock loading. However, fiber reinforcement of the brittle ceramic material offers the ability to achieve high impact resistance without unduly compromising the high temperature capability of the ceramic. A ceramic composite consisting of a lithium aluminosilicate (LAS) matrix reinforced with silicon carbide (SiC) fibers, is representative of a glass ceramic composite and was selected as one of the candidate materials. This SiC-LAS composite system has been under development at the United Technologies Research Corporation since 1976 under the tradename of Compglas®. This activity has been supported in part by the Office of Naval Research (References 7 through 11) and the Naval Air Systems Command (Reference 12) and has led to the development of a material that has properties that may be uniquely suited to use in high temperature combustor liner applications.

- o Wire Reinforced Superalloy

The use of wires of very high tensile strength to reinforce a superalloy with high temperature capability has been advocated as a means of producing turbine rotor blades with the capability of sustaining high centrifugal loads. Wire reinforced superalloy systems have been under investigation at the National Aeronautics and Space Administration-Lewis Research Center and a composite consisting of an oxidation resistant iron based alloy with chromium, aluminum and yttrium (FeCrAlY) as the matrix with thoriated tungsten reinforcing wires was selected as the second material for evaluation.

o Carbon-Carbon Composites

Composites fabricated with carbon yarns in a carbon matrix have demonstrated excellent high temperature capability when operated in an inert environment. While subject to oxidation at much lower temperatures that would preclude even their consideration as a combustor liner material, research activities are being conducted to develop oxidation inhibition and protective coatings for carbon-carbon composites. If successful, these developments could lead to an extremely viable combustor liner material and carbon-carbon composites were considered the third candidate material in the survey. The particular material evaluated consisted of two variations of a carbon-carbon composite produced by the Vought Corporation. These are designated Reinforced Carbon-Carbon (RCC) and Advanced Carbon-Carbon (ACC). While similar in formulation, the physical properties differ sufficiently that both were incorporated in the survey to be representative of the variation in properties in this family of composite materials.

5.2 Survey Procedure

The survey was conducted by establishing a list of physical properties important to the selection of a combustor liner material and its subsequent design. A literature survey was conducted to obtain data on these properties that would permit comparisons to be made of the relative merits of each material. Table 5-I presents a list of the material properties surveyed which were divided into six different categories. These categories obviously did not carry equal weight in the property selection process. In at least one case, High Temperature Applicability (Category I), failure to achieve some threshold of acceptability must be considered grounds for rejection of the material without consideration of other property categories. Likewise, a candidate material would be expected to score well in Categories II or V if economic advantages are to be derived from its use. Properties in Categories III and IV relate primarily to the conceptual definition and the thermal and structural design of the combustor liner. Screening these properties draws emphasis to the relative ease or difficulty of achieving particular design goals. For example, the lower thermal conductivity of ceramic materials relative to metallic liner materials implies greater difficulty in cooling liner surfaces by convection on the rear surface, thereby complicating the thermal design process. Similarly, a higher elastic modulus to density ratio in that material implies reduced susceptibility to vibratory distress.

The physical properties of the three composite materials evaluated were diverse and different from those of conventional metals; therefore, the corresponding properties of two metals were also collected. These materials were included in the screening process to provide a familiar frame of reference for the merits of the composite materials. The metals included were the Modified B-1900 turbine alloy selected in Section 4.1 for the segments of the reference metallic combustor liner and INCO-713 which had been an alternate for that application.

Table 5-I

Composite Material Properties Surveyed

Category I (High Temperature Applicability)

- Life Limiting Temperatures

Category II (Application Advantages)

- Density
- Use of Strategic Elements

Category III (Thermal Design)

- Thermal Conductivity
- Thermal Expansion

Category IV (Mechanical Design)

- Creep Strength
- Tensile Strength
- High Cycle Fatigue Strength
- (Elastic Modulus/Density)
- Thermal Fatigue
- Crack Propagation

Category V (Fabricability)

- Manufacturability
- Repairability

Category VI (Miscellaneous)

- Impact Energy
- Specific Heat

As the literature survey progressed it became evident that directly comparative data on the three composite materials were extremely limited. The majority of the data on the composite materials was also found to be obtained only from specimens with a unidirectional fiber orientation, whereas a multidirectional orientation was expected to be preferable in the combustor liner application. Consequently, it was evident that considerable extrapolation and qualitative judgments would be required in conducting the screening process. The principal references for information on the properties of the silicon carbide lithium aluminosilicate (SiC-LAS) composite were References 10, 11 and 12. Data on the tungsten reinforced FeCrAlY composite were obtained from References 13 through 17, while information on the carbon-carbon systems was obtained from References 18 through 23.

Table 5-II presents the results of the material property survey in which the physical properties of the three candidate composite materials, including the two variations of carbon-carbon, and the two reference metals are listed. (The assumptions involved in generating this tabulation and the implications of the property values will be discussed in Section 5.3.) With the definition of these physical property values completed, the screening process was started by assigning a numerical grade or rank to each material for the particular physical property. The grading was on a scale of one to four, with a grade of four being assigned to a material when the value of the physical property was such that it would be extremely advantageous to the combustor liner application. Conversely, the material was given a grade of one if the material property was such that its use would be detrimental. In situations where quantitative interpretation was not possible, the properties of the composites were assessed relative to metals at an arbitrary grade of two. Table 5-III lists the numerical grades assigned to all of the material-property combinations during this grading process.

Table 5-II
Comparison of Composite Material Properties

PARAMETER		ADVANCED FIBEROUS COMPOSITES				ISOTROPIC TURBINE ALLOYS	
		SIC-LAS	W-1 ThO ₂ FeCrAlY	CARBON-CARBON		MODIFIED B-1900	INCO-713
				RCC	ACC		
OXIDATION TEMPERATURE LIMITS °C (°F)	CATEGORY-I	1205 (2200)	APPROX 1095 (2000)	370-649 (700-1200)	370-649 (700-1200)	982-1095 (1800-2000)	982-1095 (1800-2000)
TEMPERATURE AT WHICH FIBER- MATRIX REACTION STARTS °C (°F)		982 (1800)	537-787 (1000-1450)	NOT APPLICABLE	NOT APPLICABLE	NOT APPLICABLE	NOT APPLICABLE
DENSITY -gm/cm ³ (LB/IN ³)	CATEGORY-II	2.50 (0.09)	12.48 (0.45)	1.38 (0.05)	1.66 (0.06)	8.20 (0.297)	7.90 (0.286)
USE OF STRATEGIC ELEMENTS		NONE	55%-W 11%-Cr 1%-Y	NONE	NONE	10%-Co 8%-Cr 6%-Mo 4.3%-Ta 1.5%-Hf	14%-Cr 4%-Mo 2%-Cb 1%-Ti
THERMAL CONDUCTIVITY W/m °C (BTU/FT HR °F)	CATEGORY-III	1.47 (0.85)	11.0 (6.35)	5.88 (3.4)	7.2 (4.2)	10.0 (5.8)	8.65 (5.0)
COEFFICIENT OF EXPANSION OF THE MATRIX °C ⁻¹ (°F ⁻¹) x 10 ⁶		1.08 (0.6)	16.2 (9.0)	6.4 (3.55)	6.4 (3.55)	11.7 (6.5)	11.9 (6.6)
CREEP RUPTURE STRENGTH AT 1095°C (2000°F) MPa (ksi.)		NOT AVAILABLE	242 MPa (35Ksi) AFTER 830 HRS.	NOT AVAILABLE	NOT AVAILABLE	62 MPa (9 Ksi) AFTER 100 HRS.	41.5 MPa (6 Ksi) AFTER 100 HRS.
TENSILE STRENGTH (ULTIMATE) MPa (Ksi.)		338 (49)	740 (107)	39 (5.6)	332 (48.0)	795 (115)	620 (90)
HIGH CYCLE FATIGUE STRENGTH MPa (ksi.)		262 (38) AT 800°C (1472°F)	552 (80) AT 760°C (1400°F)	27 (4.0)	232 (34.0)	290 (42) AT 760°C (1400°F)	304 (44) AT 760°C (1400°F)
$\left[\frac{\text{ELAS. MODULUS}}{\text{DENSITY}} \right]^{1/2}$ $\left[\frac{\text{GPa}}{\text{gm/cm}^3} \right]^{1/2} \left(\left[\frac{\text{Msi}}{\text{LB/IN}^3} \right]^{1/2} \right)$		7.45 (14.9)	4.03 (8.05)	2.58 (4.96)	8.4 (16.8)	4.95 (9.9)	5.1 (10.2)
HCF STRENGTH DENSITY $\frac{\text{MPa}}{\text{gm/cm}^3} \left(\frac{\text{Ksi}}{\text{LB/IN}^3} \right)$		105.5 (422) AT 800C (1472°F)	44 (177) AT 760°C (1400°F)	20. (80)	14 (570)	35 (141) AT 760°C (1400°F)	38.4 (154) AT 760°C (1400°F)
THERMAL FATIGUE NO CRACKING AFTER		100 CYCLES 22-982°C (72-1800°F)	1000 CYCLES 22-1095°C (72-2000°F)	NOT AVAILABLE	NOT AVAILABLE	NOT AVAILABLE	NOT AVAILABLE
CRACK PROPAGATION	CATEGORY-IV	NOT AVAILABLE				AVAILABLE	NOT AVAILABLE
MANUFACTURABILITY		LIMITED TO RELATIVELY SIMPLE SHAPES				CAN BE CAST OR MACHINED TO COMPLEX SHAPES	
REPAIRABILITY	CATEGORY-V	DIFFICULT				LESS DIFFICULT	
IMPACT ENERGY (CHARPY IMPACT) JOULES. (FT LB)		1.84 (1.36)	4.1 (3.02)	NOT AVAILABLE	NOT AVAILABLE	NOT AVAILABLE	10.8 (8.0)
SPECIFIC HEAT KJ/kg °C (BTU/LB/°F.)	CATEGORY-VI	1.05 (0.25)	NOT AVAILABLE	0.63 (0.15)	0.71 (0.17)	(0.42) (0.10)	(0.54) (0.13)

ALL PROPERTIES AT ROOM TEMPERATURE UNLESS INDICATED OTHERWISE

Table 5-III
Numerical Grading at Material Properties

PARAMETER		ADVANCED FIBEROUS COMPOSITES				ISOTROPIC TURBINE ALLOYS	
		SIC-LAS	W-1 ThO ₂ FeCrAlY	CARBON-CARBON		MODIFIED B-1900	INCO-713
				RCC	ACC		
OXIDATION TEMPERATURE LIMITS	CATEGORY-I	4	3	1	1	3	3
TEMPERATURE AT WHICH FIBER-MATRIX REACTION STARTS		3	2	1	1	3	3
DENSITY	CATEGORY-II	3	1	4	4	2	2
USE OF STRATEGIC ELEMENTS		4	1	4	4	2	2
THERMAL CONDUCTIVITY	CATEGORY-III	1	4	2	2	4	4
COEFFICIENT OF EXPANSION OF THE MATRIX		4	1	3	3	2	2
CREEP RUPTURE STRENGTH	CATEGORY-IV	2	4	2	2	2	2
TENSILE STRENGTH (ULTIMATE)		2	4	1	3	4	4
HIGH CYCLE FATIGUE STRENGTH		3	4	1	2	2	2
$\left[\frac{\text{ELAS. MODULUS}}{\text{DENSITY}} \right]^{1/2}$		4	2	2	4	2	2
$\left[\frac{\text{HCF STRENGTH}}{\text{DENSITY}} \right]$		4	2	2	4	2	2
THERMAL FATIGUE		2	2	2	2	4	4
CRACK PROPAGATION		4	4	4	4	2	2
MANUFACTURABILITY	CATEGORY-V	2	2	2	2	4	4
REPAIRABILITY		2	2	2	2	3	3
IMPACT ENERGY (CHARPY IMPACT)	CATEGORY-VI	1	2	1	1	2	2
SPECIFIC HEAT		2	2	2	2	2	2

GRADING RANGES FROM 1 FOR POOR TO 4 FOR EXCELLENT

5.3 Material Property Survey Results

The results of the material property survey and the grading of the property values relative to the combustor liner application are presented in the previously cited Tables 5-II and 5-III. Following is a discussion of the significance of the properties, the assumptions involved in constructing Table 5-II and the rationale of the grading process.

5.3.1 Temperature Limitations

If not precluded by mechanical failure or compositional changes at lower temperature levels, the temperature at which the material begins to oxidize will dictate the maximum usable temperature. The metals of Table 5-II generally encounter significant oxidation at temperatures in the 982°C to 1095°C (1800°F to 2000°F) range but, as indicated in Section 4.5, the life of these materials may be extended with oxidation resistant coatings. The threshold of oxidation of the SiC-LAS composite is dictated by the onset of oxidation of exposed silicon carbide fibers. While pure silicon carbide would not oxidize at the cited 1205°C (2200°F) temperature level, impurities in the fibers initiate oxidation at lower temperatures. This limit appears representative of current fiber materials but advances in fiber technology could raise this threshold in the future. The tungsten-FeCrAlY composite is similarly susceptible to oxidation of exposed fibers with the threshold for oxidation of the thoriated tungsten wires being about 1095°C (2000°F). While it could be intended that the fibers in both of these composites be totally immersed in the matrix to avoid exposure to the oxygen bearing atmosphere in the combustor, it would be unrealistic to assume this will always be the case because it would require extreme precision in fabrication. Hence, these temperatures, while possibly not immediate life limiting, must be considered indications of a constraining upper limit on the temperature these materials can withstand.

As indicated in Section 5.1, in the absence of a failsafe coating to isolate it from an oxygen bearing environment, carbon-carbon composites will readily oxidize at temperature levels far below those encountered in the combustor liner. While this precluded them from consideration in this study, they were included in the remainder of the screening process to demonstrate the potential of this material if an effective coating or inhibition process could be developed.

Composite materials can also be temperature limited by the onset of chemical reactions between the fiber and the matrix that reduce the strength of either component or that of the bond between them. Such reactions are known to occur in the SiC-LAS composite at temperatures above 982°C (1800°F) and tend to weaken the fibers. A similar reduction in fiber strength can occur in the thoriated tungsten-FeCrAlY system, but in this case the mechanism can be recrystallization of the tungsten at temperatures in the range of 537°C to 787°C (1000°F to 1450°F). However, in both of these materials the degradation in fiber strength does not appear to be large enough to constitute a life limiting constraint on the material.

Following evaluation of the properties of the materials in the context of the survival temperature limits in Category I, it is evident that the SiC-LAS composite material is the only candidate offering potential for near term use at temperature levels higher than those tolerated by the reference metals. It is also recognized that the development of a failsafe protective coating or inhibition process to prevent oxidation of carbon-carbon could make it an attractive candidate in this respect.

5.3.2 Density

Component weight can be a strong consideration in engine design and other factors being equal, low density materials are favored. Both the carbon-carbon and the SiC-LAS systems are shown to offer significant weight advantages relative to the reference metals. Carbon-carbon is about one-fifth the density of these metals, while the density of SiC-LAS is about 30 percent of that of the metals. Conversely, the tungsten reinforced FeCrAlY is about 50 percent heavier than the reference metals. This is a consequence of the high density of the tungsten fibers. Both SiC-LAS and carbon-carbon offer decided advantages in terms of the potential for producing a lightweight component.

5.3.3 Strategic Materials

Silicon carbide-lithium aluminosilicate and carbon-carbon composite systems also offer the distinct advantages of being fabricated from readily available raw materials. On the other hand, the Modified B-1900 turbine airfoil alloy selected in Section 4.1 for the segments of the reference metallic liner in this study contains high concentrations of strategically critical raw materials with the total chromium and columbium content alone being 18 percent. The alternative reference metal in Table 5-II, INCO-713, is not much better with the total content of these two materials reaching 16 percent. The thoriated tungsten-FeCrAlY composite is also at a distinct disadvantage because the tungsten wire, which comprises 55 percent of the material volume, is costly in itself and the superalloy used for the matrix is about 20 percent chromium.

5.3.4 Thermal Conductivity and Expansion

High thermal conductivity, at least in the through thickness direction of the material, is a desirable property for combustor liner concepts in which extensive use is made of heat transfer from the cold side surface of the liner as in the metallic liner construction of Section 4.0. Conversely, a low coefficient of thermal expansion is desirable because it reduces the thermal stress associated with temperature gradients in the material. As examination of Table 5-II indicates, there are strong parallels in the magnitude of these properties for the various materials. The thermal conductivity and coefficient of expansion of carbon-carbon and SiC-LAS are both lower than those of the reference metals. In the case of the carbon-carbon both of these properties are of the order of 40 to 70 percent of those in the metals, while in SiC-LAS they are both about 10 to 15 percent of the metal property values. Consequently, while the extraction of heat through one of these lower thermal conductivity materials will generate larger temperature gradients, the proportionately

Lower coefficient of expansion will result in less propensity for differential expansion and, to a first approximation, no significant change in the associated thermal stress. Of course, there are other implications of low thermal conductivity and thermal expansion coefficient that influence the combustor liner design. Low conductivity still makes the thermal design more difficult because alternative cooling approaches, other than internal or cold side convection, may be required. While low thermal expansion is an advantage on accommodating temperature gradients within the composite structure, the difference in thermal expansion at the point where the composite material is attached to the surrounding metallic structure must also be recognized as a potential design problem.

5.3.5 Static Strength

Table 5-II lists the ultimate tensile strength of unidirectionally reinforced specimens of the composite materials and the corresponding reference metals at room temperature. The strength of the metals was defined by direct tensile loading, while that of the composites was deduced from the tensile side of beam specimens loaded in flexure (c.f. Section 6.0). The data show the tungsten-FeCrAlY composite has a tensile strength comparable to the advanced turbine alloys, while the SiC-LAS and the advanced carbon-carbon have about half the tensile strength of the metals. There is evidently considerable variation in tensile strength within the carbon-carbon system because the reinforced carbon-carbon was found to have only about one-tenth the ultimate strength of the advanced carbon-carbon.

While there were no available comparable data on the SiC-LAS and carbon-carbon materials, the creep rupture strength of the tungsten-FeCrAlY demonstrates one of the major advantages of the composite construction. The data of Table 5-II indicate that the 100 hour creep rupture strength of the reference metals at 1095°C (2000°F) are only about 7 or 8 percent of their ultimate strengths at room temperature, whereas the tungsten reinforced FeCrAlY retains more than one-third of its ultimate strength after a much longer exposure to the same temperature levels.

5.3.6 Dynamic Strength

The dynamic strength of a material may be significant when the component is subject to vibration and other oscillatory loads. The ratio of elastic modulus to density is significant in vibratory loading because it is a measure of the stiffness of the material resisting motion to the inertia of excited components. A higher stiffness to inertia ratio implies a higher natural frequency with less propensity for excitation by engine speed related forces. SiC-LAS and advanced carbon-carbon are shown on Table 5-II to have square root elastic modulus to density ratios about 1.5 and 1.7 times higher than the reference metals, respectively. Reinforced carbon-carbon, despite having a low density comparable to advanced carbon-carbon, is inferior to the metals in this category because it has a low elastic modulus.

While the elastic modulus to density ratio provides a measure of the risk of exciting a dangerous vibratory mode, the high frequency fatigue strength or the ratio of this strength to material density determines its ability to withstand the oscillatory loading. Table 5-II lists the high cycle fatigue strength and its ratio to material density for failure of the test specimen after one million mechanical load cycles. As in the case of the static strength tests cited in Section 5.3.5, the metals were tested in a direct tensile loading mode, while the composite materials were evaluated in flexure. While the carbon-carbon composites were evaluated only at room temperature, the other materials were tested at comparable elevated temperatures. When the high frequency fatigue strength is compared with the ultimate strength at room temperature, the composite materials are shown to have considerably greater relative fatigue strength than the metals. While the elevated temperature fatigue strength of the metals is of the order of 35 to 50 percent of the room temperature ultimate strength, the corresponding ratios for both the SiC-LAS and tungsten-FeCrAlY composites are 75 percent or more. These strength ratios are not as high for the carbon-carbon systems, and in this case the fatigue data were also obtained at room temperature.

5.3.7 Thermal Fatigue

As the analysis of Section 4.4 indicated, the life limiting mechanism in the reference metallic combustor liner is expected to be cracking due to thermal fatigue. After a number of thermal cycles, cracks will develop in highly stressed areas of the liner segments, and with continued thermal cycles these cracks will propagate to greater length at which the risk of breaking becomes excessive. Data on thermal fatigue crack initiation and propagation in both the metals and the composite materials are very limited. SiC-LAS and tungsten-FeCrAlY composites have been subjected to limited thermal cycling between room temperature and 982°C to 1095°C (1800°F to 2000°F) with no evidence of crack initiation, but these tests are considered too short and limited in scope to be conclusive. Composite materials may enjoy a unique advantage in resisting crack development and propagation by being able to orient the fibers in progressively varying directions in each layer of the material, but this property has yet to be quantified.

5.3.8 Workability

Metals can readily be cast or machined into the shapes required for combustor liner components. Composites require the layering of the reinforcing fibers within the matrix material followed by some form of processing, generally at elevated temperatures and pressures, to solidify the matrix and establish bonds to the fibers. This fabrication process limits the complexity of composite parts. Once a composite part has sustained damage to the extent that internal fibers are broken or dislocated in critical areas, the part must generally be replaced. Alternatively, in some situations, metal parts may be repairable by welding.

5.3.9 Miscellaneous Properties

Other properties defined during the literature survey but not of significant import to the combustor liner design or material screening processes are the impact resistance and specific heat of the materials. The Charpy impact resistance of SiC-LAS and tungsten-FeCrAlY composites to loads applied normal to the direction of the fibers has been measured and is shown on Table 5-II to be about 20 and 40 percent respectively of that of INCO-713 metal. While low relative to the reference metals, the impact resistance of either of these materials is more than adequate for the combustor liner application. For comparative purposes silicon nitride, a monolithic ceramic, has been found to have a Charpy impact resistance of only 0.4 joules (0.3 ft lb) which is less than one-fourth that of SiC-LAS.

The specific heat of combustor liner materials is significant only in transient events in which there could be concern over the rate of thermal expansion of adjacent and attached components. As shown on Table 5-II, the specific heat of carbon-carbon composites is of the order of 50 percent higher than the reference metals, while SiC-LAS has about twice the specific heat of the metals. Consequently, on a mass basis the temperature of these composites will respond slower to a thermal transient than adjacent metals. However, these composite materials are also less dense and, particularly in the case of the SiC-LAS, on the basis of equal component volumes the temperature response rate would be more nearly equal to that of the metals.

5.4 Material Screening and Selection

As indicated in Section 5.2, while the data on the physical properties of the composite materials and the reference metals were being accumulated, the materials were being graded on the basis of the merit of that particular property to the combustor liner application. Grading had been on a scale of one to four for detrimental through highly advantageous characteristics respectively. Based on the discussion of Section 5.3, these grades are listed on Table 5-III. It was also indicated in Section 5.2 that the merits of some physical properties are more important than those of others and, hence, the surveyed properties had been grouped in the six categories defined on Table 5-I. In evaluating the potential of the composite materials and selecting the most appropriate near term material for the remainder of this study, it was necessary to weight these categories when appraising the grades in Table 5-III. Consequently, weighting factors were defined for each category, and the grades assigned in Table 5-II were multiplied by these factors before an overall grade for each material was computed by summing the weighted grades. Table 5-IV lists the multiplicative weighting factors for each category, while Table 5-V presents a summary of the total scoring.

Table 5-IV
Weighting Factors for Material Property Categories

<u>Category</u>	<u>Factor</u>
I - High Temperature Applicability	5.0
II - Application Advantages	4.0
III - Thermal Design	3.0
IV - Mechanical Design	2.0
V - Fabricability	1.0
VI - Miscellaneous	0.5

Table 5-V
Overall Grading of Materials Based on Physical Properties

<u>Category</u>	<u>Advanced Fibrous Composites</u>				<u>Isotropic Turbine Alloys</u>	
	<u>SiC-LAS</u>	<u>W-1ThO, FeCrAlY</u>	<u>Carbon-Carbon</u>		<u>Modified B-1900</u>	<u>INCO-713</u>
			<u>RCC</u>	<u>ACC</u>		
I	35	25	10	10	30	30
II	28	8	32	32	16	16
III	15	15	15	13	16	16
IV	42	44	28	44	38	38
V	4	4	4	4	7	7
VI	1.5	2	1.5	1.5	2	2
Total All Categories	125.5	98	90.5	104.5	119	119
Total Categories I and II only	63	33	42	42	46	46

The scoring of Table 5-V indicate that the silicon carbide reinforced lithium aluminosilicate (SiC-LAS) ceramic composite is the only composite material to score higher than the reference metals. The total scoring is shown to be dominated by the first two property categories - High Temperature Applicability and Application Advantages. The selection of SiC-LAS as the reference material for the remainder of this study is based in its apparent capability to withstand higher temperature levels than the reference metals while having only one-third the density and not requiring costly strategically critical raw materials. Carbon-carbon composites have been rejected from this study only because of their lack of oxidation resistance. With future development of fail-safe antioxidation coatings or oxidation inhibition procedures, carbon-carbon composites could become an even more attractive combustor liner material. It is even less dense than SiC-LAS and has thermal conductivity and expansion coefficients that are not as much different from metals.

SECTION 6.0

EXPERIMENTAL EVALUATION OF COMPOSITE MATERIAL PROPERTIES

The composite material screening process described in Section 5.0 was, of necessity, based on mechanical property data from composites having unidirectional fiber orientations. However, in the combustor liner application, there is no preferred orientation of the fibers for maximum strength. To the contrary, the uncertainties in the locations of regions of high temperature gradients and their direction dictate that the material layup be selected so as to provide an essentially isotropic composition in the in-plane directions. Consequently, in the initiation of the liner design process to be described in Section 7.0, a SiC-LAS (silicon-carbide reinforced lithium aluminosilicate) composite with a $0^\circ/+45^\circ/-45^\circ/90^\circ$ sequence of fiber orientation in the layup was selected. Due to the lack of mechanical and thermal property data on material of this structure, the program included an experimental evaluation activity in which this type of material could be fabricated and tested to establish some of the most critical property characteristics. These tests consisted of evaluation of the static load carrying capability and the creep characteristics of the material in flexure; investigation of the mechanical and thermal fatigue resistance of the composite; and assessment of critical thermal design parameters including expansion, conductivity and surface emissivity. The procedures and results of these tests are described in this section.

6.1 Test Specimen Fabrication

All of the specimens used in the experimental investigation were fabricated at United Technologies Research Center and the majority of the tests were also conducted at that facility. The silicon-carbide fiber used to fabricate the specimens was obtained in continuous length (approximately 500 m) tows of 250 fibers/tow with an average fiber diameter of 12 microns. The average tensile strength and elastic modulus of this fiber, as measured at United Technologies Research Center, is 2060 MPa (300 ksi) and 193 GPa (28×10^6 psi), at room temperature respectively. The lithium aluminosilicate (LAS) matrix material used in these specimens was a chemically modified form of Corning Glass commercial 9608 LAS. This material is obtained from Corning Glass as glassy powder.

The composite specimens were fabricated by passing the silicon-carbide yarn through an agitated slurry of glass powder, water and an acrylic binder, and then wound onto a rotating drum. The resultant tape was then cut into the appropriate dimensions and fiber orientations, heated in air to 600°C (1112°F) to remove the binder, and stacked in a graphite hot-press die in the desired sequence and number. The per ply thickness of the material was about 0.13 to 0.15 mm (0.005 to 0.006 in); hence, a typical panel 2.3 mm (0.090 in) thick contained 16 layers. The stacked material was hot-pressed in a vacuum furnace at elevated temperatures and pressure. The resulting composite panels were fully dense (2.5 gms/cc) with nominal dimensions of 7.6 cm (3.0 in) square with thickness ranging from 1.15 mm (0.045 in) to 6.3 mm (0.25 in) depending upon the intended use. Following hot-pressing, all panels were heat treated at above 900°C (1650°F) to crystallize (ceramic) the matrix to provide high temperature matrix stability.

A total of nine panels were used to fabricate the test specimens. Table 6-I provides a listing of the layups of each of the panels, which had been identified by a four-digit serial number at fabrication. Panels of three different thicknesses were made to meet the requirements of the specific tests. All of the panels were made with the selected $0^\circ/+45^\circ/-45^\circ/90^\circ$ sequence of fiber orientation in successive layers and the layup was maintained symmetrical with respect to the central plane. In establishing the thicknesses of the test specimens, the number of layers was allowed to change in increments of eight so as to include only entire sequences of the four fiber orientations as shown on the table.

Table 6-I

Fiber Orientation in SiC-LAS Panels Used to Make Test Specimens

<u>Panel</u>	<u>Nominal Thickness mm (in)</u>	<u>Number of Layers</u>	<u>Fiber Orientation by Layer Progressing Outward From Center</u>
2398 2437 2438	1.15 (0.045)	8	0/+45/-45/90
2348 2349 2350 2351	2.3 (0.090)	16	0/+45/-45/90/0/+45 -45/90
2352 2353	6.3 (0.250)	40	0/+45/-45/90/0/+45 -45/90/0/+45/-45/90 0/+45/-45/90/0/+45 -45/90

The majority of the composite panels were cut with diamond edge cutters into a number of beam type test specimens having nominal widths of 5 and 10 mm (0.20 and 0.40 in). These individual specimens are identified by the number of the panel from which it was cut followed by a dash and another identifying digit (e.g., 2349-2). An effort was made to obtain specimens for each test from a number of different panels so that panel-to-panel variations, which might be caused by minor differences in layup technique, could be investigated.

6.2 Evaluation of Static Load Characteristics

The objective of these tests was to determine the stress-strain characteristics of the SiC-LAS composite material including the elastic modulus, elastic limit and ultimate strength over the range of temperatures from ambient to 1037°C (1900°F). Due to the difficulty of making end attachments for a conventional tensile test specimen in the composite material, this information was obtained from measurement on the side of a beam that was loaded in flexure in the apparatus shown on Figure 6-1. A total of twenty specimens were tested in

this ceramic bend test facility. Consisting of all ceramic test fixtures, this system is capable of operating in air up to temperatures of approximately 1200°C (2200°F). The loading rams and specimen holders are made of siliconized silicon-carbide while the actual loading pins are alumina. The specimens were 7.6 cm (3.0 in) long and had a rectangular cross section of 2.3 by 10.0 mm (0.09 by 0.40 in) with the plane of the fibers parallel to the 10.0 mm dimension. The tests were conducted in a four point flexural mode as shown on Figure 6-2 with the major and minor spans being 6.35 and 1.91 cm (2.50 and 0.75 in) respectively and the load being applied normal to the plane of the fibers. All of the tests were conducted in an air environment.

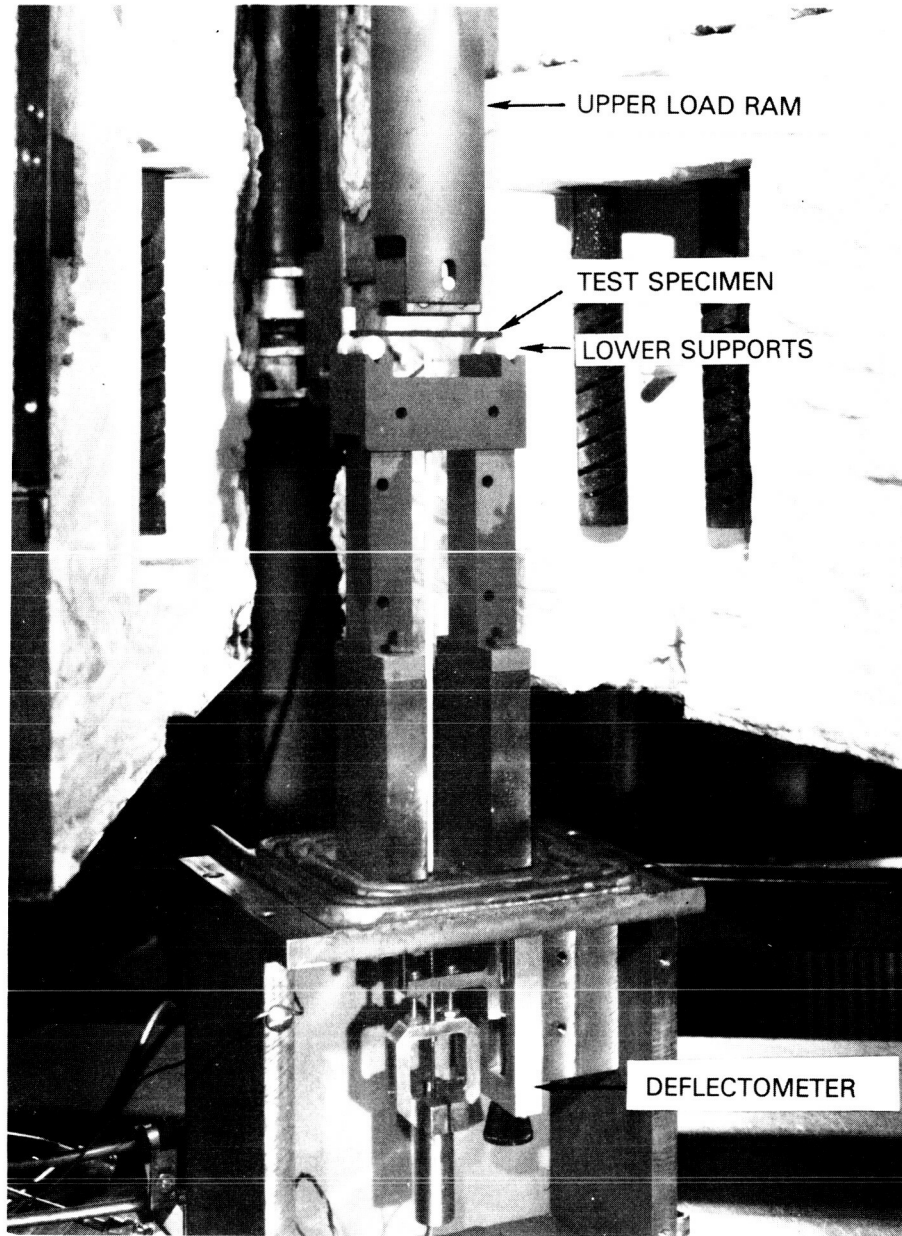


Figure 6-1 High Temperature Flexural Test Facility

The initial tests were conducted at room temperature, and the strain on the top and bottom surfaces of the specimens was measured with strain gages. During the elevated temperature tests, the midspan deflection of the specimen was measured with a remotely situated linear variable differential transformer that was in contact with the specimen through a ceramic extension rod. The strain in the specimen was deduced from prior calibration of this deflectometer against strain gages on a similar specimen. The stress in the top and bottom surfaces of the test specimen at the midspan location was calculated from the equation:

$$S = \pm \frac{3}{2} \frac{(L - \ell) P}{bh^2} \quad (6-1)$$

where the nomenclature is defined on Figure 6-2.

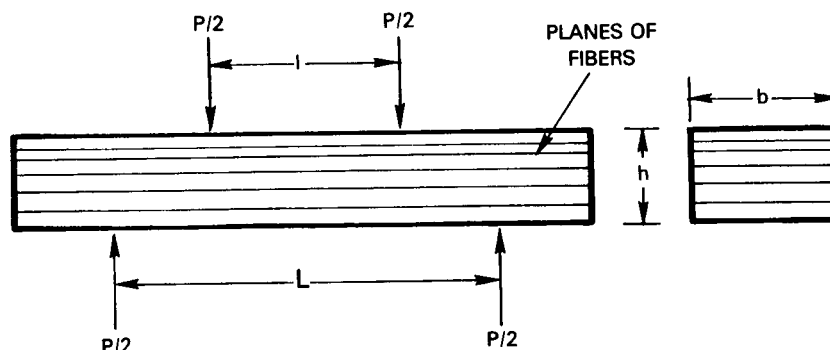


Figure 6-2 Four Point Flexural Test Geometry

Figure 6-3 shows the stress-strain characteristics of one of the specimens evaluated at room temperature with strain gages on the tension and compression surfaces. As anticipated, both sides exhibit an almost identical strain history. Following an initial linear region extending to about 100 MPa (15 ksi) applied stress, the material exhibits a shift in slope or apparent decrease in elastic modulus that defines a second region of nearly linear response to a stress level of about 225 MPa (34 ksi). This second linear regime occurred only in some of the specimens tested at room temperature and was replaced by a progressive departure from linearity in specimens tested at elevated temperatures. Table 6-II presents a summary of the results from the four strain gaged test specimens evaluated at room temperature. The elastic moduli were determined from a curve fit of data obtained at strains below 0.15 percent which was considered to be the proportionality limit. With the exception of the data from Specimen 2348-1, the elastic modulus based on strain of the tensile and compressive surfaces are in agreement within 6 percent. The ultimate strength and strain at failure in specimen 2348-1 were also somewhat lower than that observed with the other three specimens.

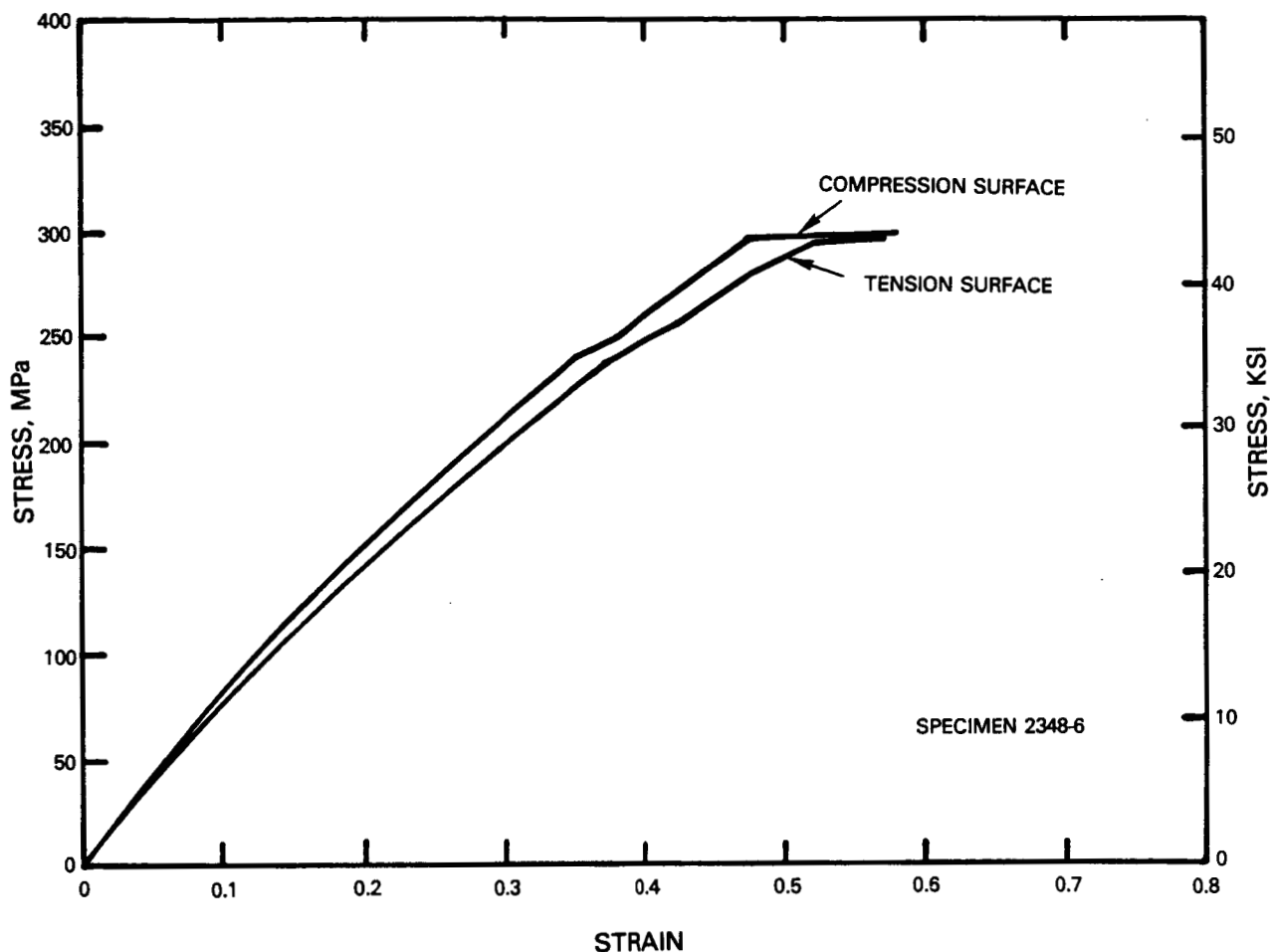


Figure 6-3 Stress-Strain History in Flexural Test at Room Temperature

Table 6-II

Strain Gaged Composite Room Temperature Flexure Test Data
(0/+45/90) SiC Reinforced LAS)

Composite Panel	Specimen Number	Flex. Strength MPa (ksi)	Tension Side		Compression Side	
			El. Modulus GPa (Msi)	Fail Strain %	El. Modulus GPa (Msi)	Fail Strain %
2348	1	240 (34.8)	69.8 (10.1)	0.53	80.6 (11.7)	0.37
2348	6	296 (43.0)	76.3 (11.1)	0.57	81.1 (11.8)	0.58
2349	1	308 (44.7)	69.8 (10.1)	0.58	72.8 (10.6)	0.51
2350	2	335 (48.6)	70.3 (10.2)	0.59	74.2 (10.8)	0.67

Figure 6-4 shows the effect of increasing temperature on the stress-strain history in the SiC-LAS material. Data are presented from the testing of five specimens, all cut from the same panel. The testing was conducted at temperatures between room temperature and 1038°C (1900°F). The data indicate no pronounced change in the load carrying characteristics between room temperature and 594°C (1100°F). Even at a temperature of 871°C (1600°F), the response to loading is nearly identical to that at room temperature up to stress levels of about 150 MPa (22 ksi). Further increases in temperature are then shown to diminish the strength of the material over the entire range of load and reduction in the elastic modulus as evident from Figure 6-4. The extent of the regime of elastic behavior appears to be independent of temperature with the proportionality limit being about 100 MPa (15 ksi) at all of the temperature levels investigated. Beyond the proportionality limit, the stress-strain histories show progressively greater departures from linearity as the temperature is decreased. It is suspected that these departures are caused by microscopic level internal failures in the material; the first of which to be encountered are slippage at the matrix-fiber interfaces and microcracking of the matrix.

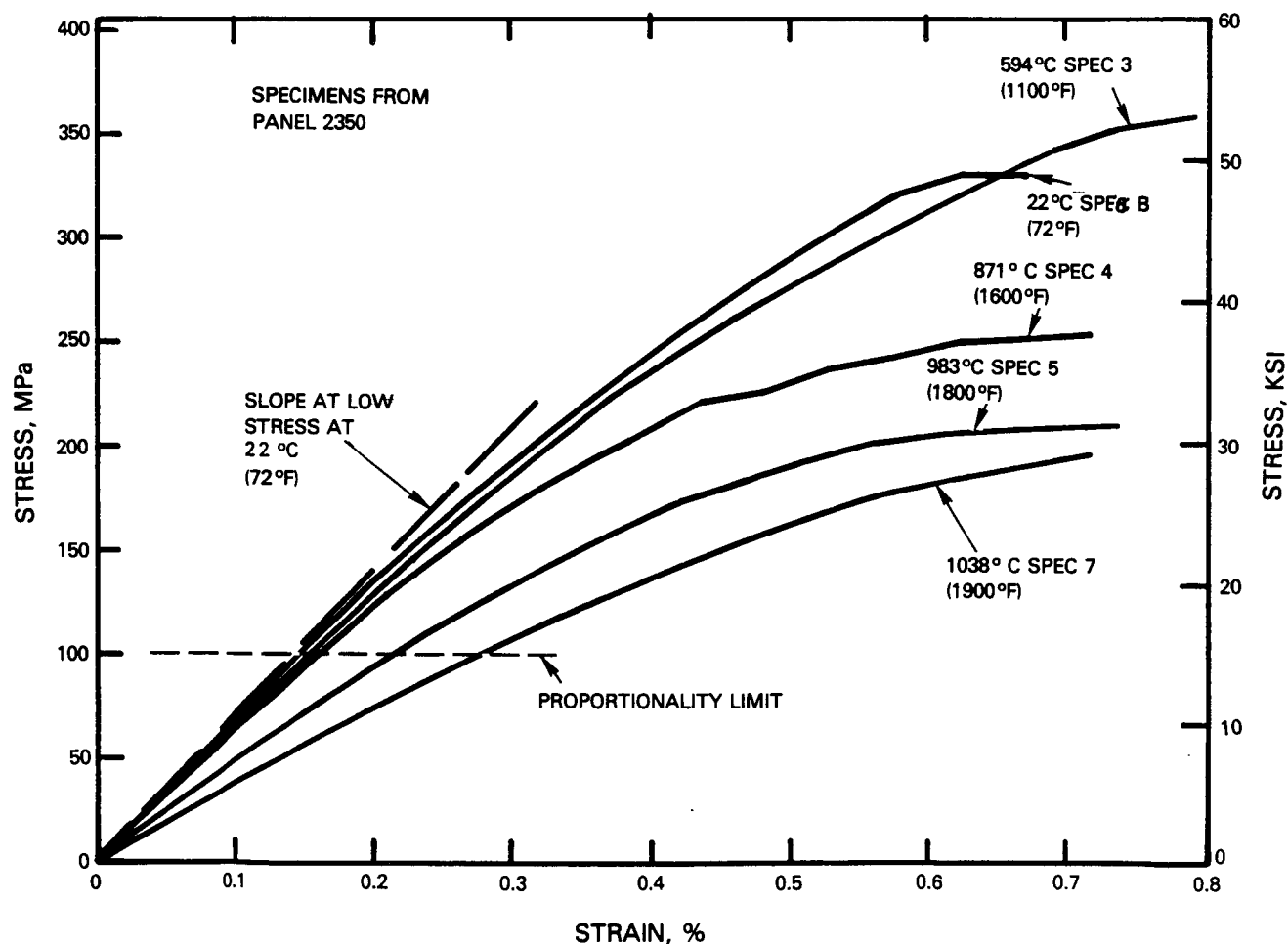


Figure 6-4 Stress-Strain Data for SiC-LAS Composite Material Over a Range of Temperature

Table 6-III provides a listing of the important strength parameters from all of the specimens evaluated which included three specimens at each temperature level. The ultimate strength and elastic moduli of the specimens are shown graphically as a function of temperature on Figure 6-5. This figure also includes data from the specimens evaluated at room temperature with strain gages listed on Table 6-II. The trends demonstrated by the entire body of data parallel and reinforce those deduced from the results from the set of five specimens on Figure 6-4. In particular, the elastic modulus remains constant at a mean level of about 75 GPa (10.9 Msi) to a temperature of 871°C (1600°F) after which it declines significantly. The ultimate strength of the SiC-LAS material is about 320 MPa (46 ksi) at room temperature and appears to increase slightly as temperature increases to 871°C (1600°F) before it also begins to decline. However, at 1038°C (1900°F) it retains a strength of nearly 200 MPa (29 ksi) or more than 60 percent of its strength at room temperature.

Table 6-III

Composite Flexure Test Data
(0/+45/90 SiC Reinforced LAS Testing in Air)

Composite Panel	Specimen Number	Test Temperature °C (°F)	Ultimate Strength MPa (ksi)	Elastic Modulus GPa (Msi)	Tensile Side Failure Strain %	Failure Type**
2349	7*	22 (72)	316 (45.8)	79.5 (11.5)	0.74	T+C
2350	6	22 (72)	331 (47.9)	77.4 (11.2)	0.67	T+C
2351	1	22 (72)	234 (34)	61.1 (8.86)	0.60	C
2351	7*	22 (72)	257 (37.3)	65. (9.43)	0.64	T+C
2348	2	594 (1100)	323 (46.8)	74.7 (10.8)	0.71	T+C
2349	2	594 (1100)	323 (46.9)	70.6 (10.2)	0.75	T+C
2350	3	594 (1100)	361 (52.3)	72.9 (10.6)	0.79	T+C
2348	3	871 (1600)	222 (32.1)	77.8 (11.3)	0.42	T
2349	3	871 (1600)	255 (36.9)	74.7 (10.8)	0.50	T
2350	4	871 (1600)	254 (36.9)	69.5 (10.1)	0.72	T
2348	4	983 (1800)	245 (35.6)	57.9 (8.4)	0.69	T
2349	6	983 (1800)	227 (32.9)	51.5 (7.47)	0.88	T
2350	5	983 (1800)	211 (30.6)	54.3 (7.87)	0.74	T
2348	5	1038 (1900)	305 (44.2)	49.1 (7.12)	1.10	T
2349	5	1038 (1900)	357 (51.8)	49.5 (7.17)	1.10	T
2350	7	1038 (1900)	197 (28.5)	40.8 (5.91)	0.72	T

* These two specimens were 5 mm wide as compared to the standard 10 mm width for all other specimens.

** T = Tensile failure apparent
C = Compression failure apparent

Table 6-III contains a listing of the mode of failure of the specimens which indicates two distinct regimes. At temperatures of 594°C (1100°F) and below, failure was generally evident on both the tensile and compressively loaded surfaces of the specimen. At higher test temperatures, there was no evidence of compressive failure and all of the specimens failed on the tensile side. The low temperature compressive failures had consisted of localized crushing or powdering of the matrix material.

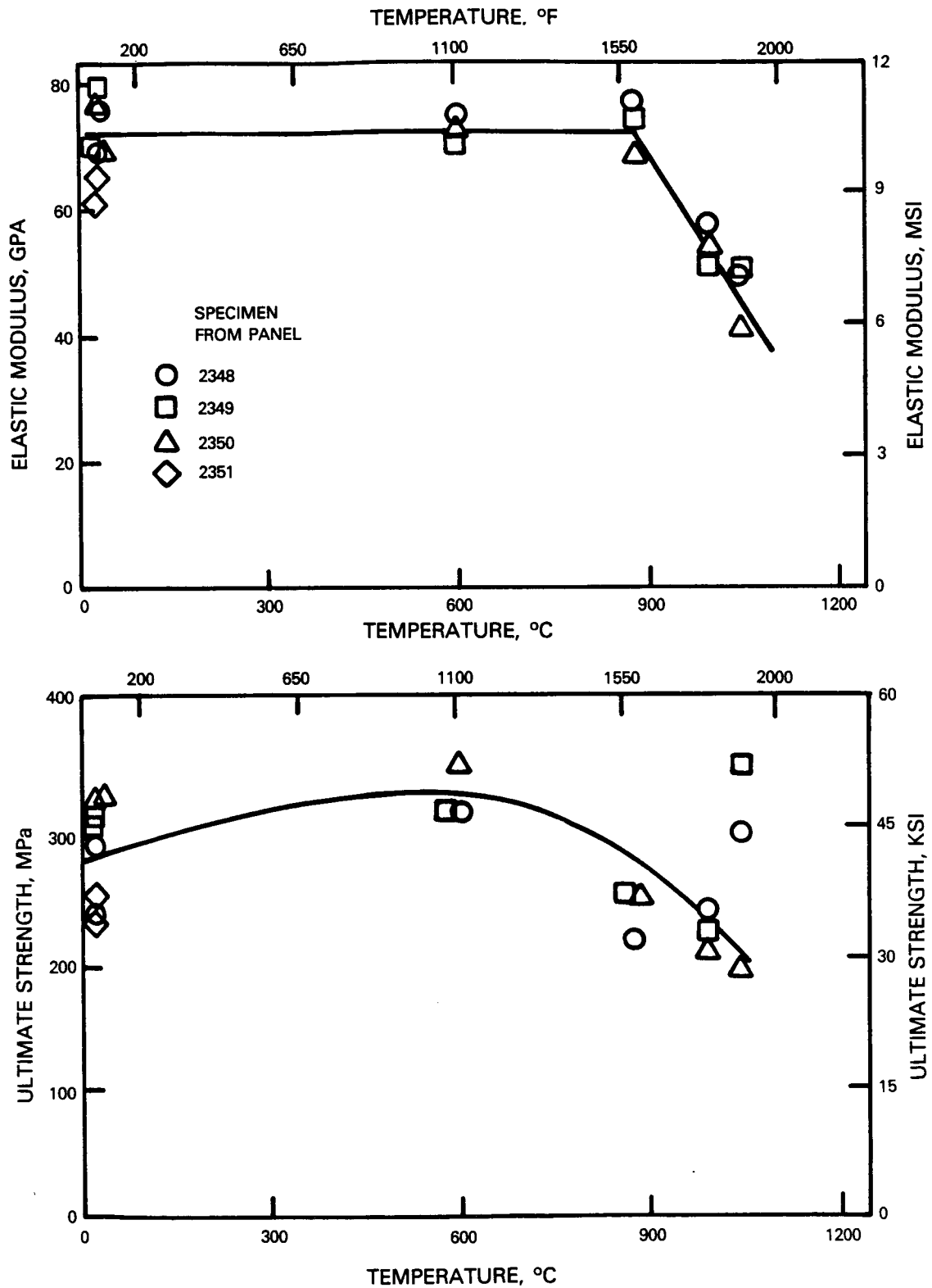


Figure 6-5 Effect of Temperature on the Strength Characteristics of the SiC-LAS Composite Material

Comparing the properties of the multidirectional layup of the SiC-LAS composite with those cited for unidirectionally reinforced material in Section 5.0 indicates that, as expected, the ultimate strength has been reduced. At room temperature the 0/+45/90 layup material had an ultimate strength of about 320 MPa (46 ksi); whereas ultimate strengths of 620 to 700 MPa (90 to 100 ksi) were reported in Section 5.0 for SiC-LAS composites with all the fibers in the direction of the applied load. Likewise, the modulus of elasticity of the multidirectional composite at 75 GPa (10.9 Msi) is about half that of the material with unidirectional fiber orientation. The loss in strength encountered in changing to the multidirectional layup is not considered a disadvantage in the combustor design application in which a quasi-isotropic in-plane material structure is desirable. The available ultimate strengths of the order of 200 MPa (30 ksi) at temperatures of 1038°C (1900°F) are also attractive for the combustor design.

6.3 Creep Strength Characteristics

The tests to assess the creep strength characteristics of the SiC-LAS material were conducted in the same four point flexural mode as the static strength tests of Section 6.2 and using specimens of the same size. Specifically, the specimens were 7.6 cm (3.0 in) long and had a rectangular cross section nominally 2.3 by 10.0 mm (0.09 by 0.4 in) with the fiber in planes parallel to the 10.0 mm dimension. The tests were conducted in the same size four point loading fixture used in the static strength tests shown on Figure 6-1. The spans between the load points were retained at 6.35 and 1.91 cm (2.50 and 0.75 in) as in those tests. The tests were conducted in an Instron load controlled testing machine. Due to the use of tungsten heater elements, the tests were conducted in an argon environment. As in the static strength tests at elevated temperature, the stress in the surfaces of the specimens was calculated from Equation 6-1 while the strain in those surfaces was deduced from the previously calibrated deflectometer in the test fixture.

A total of four specimens were subjected to creep loading with each test having a nominal duration of 140 hours. Two specimens were evaluated at a temperature of 926°C (1700°F) and two at 1037°C (1900°F). At each temperature one specimen was loaded to about 86 MPa (12.5 ksi) stress in steps over a 20 to 40 hour period, then maintained at that load for the remainder of the test period. The other specimens were subjected to a constant and higher nominal load level of 138 MPa (20 ksi) over the entire test duration. These load levels were selected because they are of the order of half the ultimate strength of the material at these temperatures and represent a working stress in some applications.

Figure 6-6 shows the results of two of these tests in which the total (i.e., static and creep) strain in the tensile surface of the specimen is presented as a function of time. At each load increment the SiC-LAS material exhibits a primary-secondary mode of creep with the secondary mode being essentially linear with time. This steady state creep rate was determined graphically over the long term essentially linear domain at the high loading as shown on this figure.

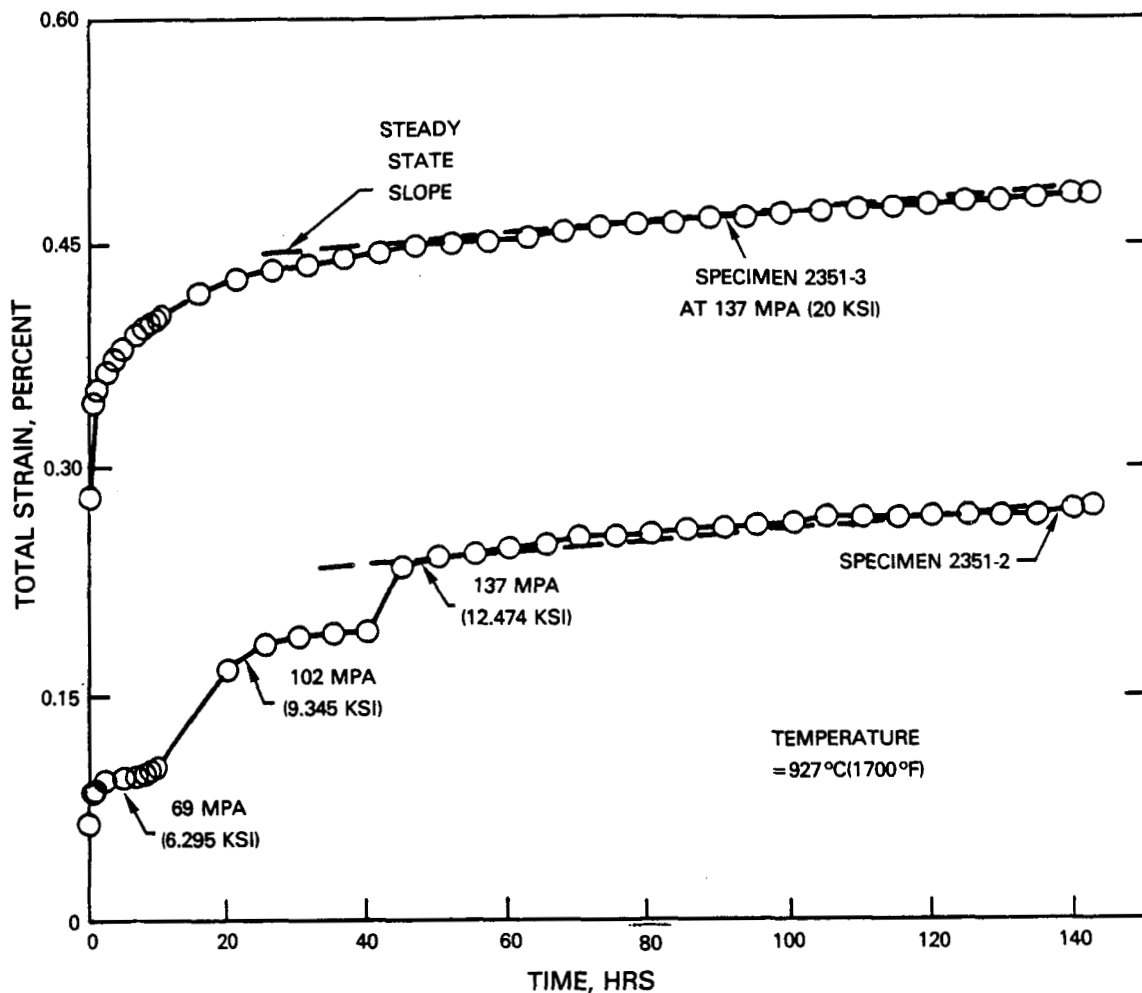


Figure 6-6 Strain Histories During Creep Tests of the SiC-LAS Composite Material

Following completion of the creep tests, the four specimens were tested to failure in a flexural mode to determine their residual strength. The test configuration was also identical to that used in the static strength tests of Section 6.2 in order to compare the results to that data.

Table 6-IV provides a summary of the loading histories of the four specimens, the graphically determined creep rate at the highest loading, and the residual strength of each specimen. The steady state creep rates are comparable to those of high quality cast alloys. In particular, comparison to data from the Modified B-1900 turbine airfoil material used for the segments of the reference liner design of Section 4.0 indicate the creep rates are essentially equal at the 927°C (1700°F) condition; and that of the SiC-LAS composite has a

considerably lower creep rate than that metal at 1038°C (1900°F). While this observation must be tempered with the realization that load histories are more difficult to control in the flexure type test than in the direct tensile loading tests of the metals, the results are still encouraging.

Table 6-IV

Results of Flexural Creep Testing of
SiC-LAS Material in Argon

Specimen	Temperature °C (°F)	Applied Stress MPa (ksi)	Time (hrs)	Steady State Creep Rate (hr ⁻¹)	Residual Strength at 22°C (70°F) MPa (ksi)
2351-2	927 (1700)	43.5 (6.3)	0-20	-	278 (40.3)
		64.1 (9.3)	20-45	-	
		86.2 (12.5)	45-143	3.8 x 10 ⁻⁶	
2351-3	927 (1700)	138 (20.0)	0-138	4.3 x 10 ⁻⁶	275 (39.8)
2351-5	1038 (1900)	42.9 (6.2)	0-20	5.0 x 10 ⁻⁶	292 (42.2)
		86.2 (12.5)	20-137		
2351-6	1038 (1900)	10.4 (15.0)	0-154	3.7 x 10 ⁻⁶	282 (40.8)

The measurement of residual strength of the creep loaded specimens is particularly interesting because two of the specimens used in the static strength tests of Section 6.2 were cut from the same panel of SiC-LAS as those used in the creep test, thereby eliminating that variable. Those specimens, Specimens 2351-1 and 2351-7, had ultimate flexural strengths of 235 and 258 MPa (34.0 and 37.3 ksi) respectively, while the specimens that had been creep loaded had higher residual strength reaching 276 MPa (40 ksi) or more. The specimens that had been creep loaded at 927°C (1700°F) were of further interest because the failure mode was different. Other specimens, both virgin and creep exposed, tended to fail in combination of compression and tensile failure at room temperature; whereas the dominant failure mode in these two specimens was interlaminar shear at a higher loading than the compression-tensile failure was encountered in the corresponding virgin specimens.

6.4 Mechanical Fatigue Tests

A series of tests was conducted to investigate the fracture toughness of and mechanical fatigue mechanisms in the SiC-LAS composite material. The specimens used in these tests had nominal dimensions of a 6.35 mm (0.25 in) square cross section and 7.6 cm (3.0 in) in length and consisted of a forty layer layup in the same 0/+45/90 fiber orientations used in all other test specimens. The majority of the specimens were notched to 45 percent of the specimen depth in

the center using a 0.153 mm (0.006 in) thick cutting wheel. The tests were conducted in a three point flexural bending mode with the applied load in a plane parallel to the composite layers, as shown in Figure 6-7. The span of flexural apparatus was 5.08 cm (2.0 in) with the load being applied centrally opposite the notch. Tests were conducted at room temperature and at 982°C (1800°F) with the latter in an argon environment. The stress at the base of the notch (or with c set equal to zero at the tensile surface of an unnotched specimen) was calculated from the equation:

$$S = \frac{3}{2} \frac{PL}{b(h-c)^2} \quad (6-2)$$

where the nomenclature is defined on Figure 6-7. The deflection of the specimen under load was determined with a deflectometer similar to that used in four point loading tests of the preceding sections but located off the center plane of the loading apparatus.

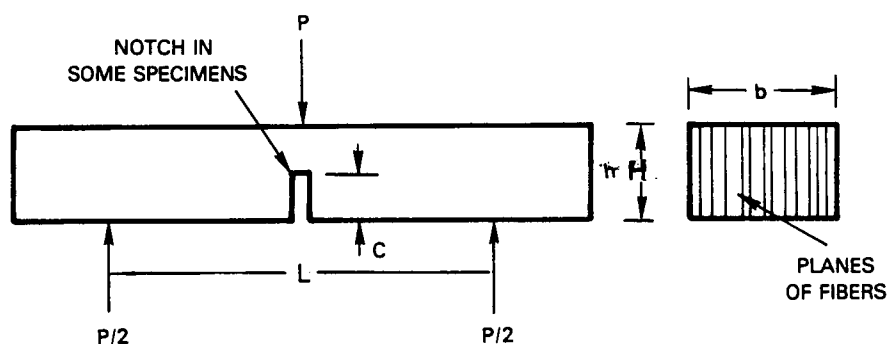


Figure 6-7 Geometry for Mechanical Fatigue Tests

The first series of tests consisted of monotonic loading of notched and unnotched specimens to determine the fracture toughness of the SiC-LAS material. A total of ten specimens were tested to failure. Figure 6-8 shows representative load-deflection characteristics for specimens loaded at room temperature and at 982°C (1800°F). At both temperatures the load-deflection curve was somewhat rounded prior to maximum load and then showed a gradual decrease in load with increasing deflection illustrating a considerable resistance to crack growth. After testing, the specimens were found to still not have fractured in two and crack growth was along a very irregular path as shown on the photograph of Figure 6-9.

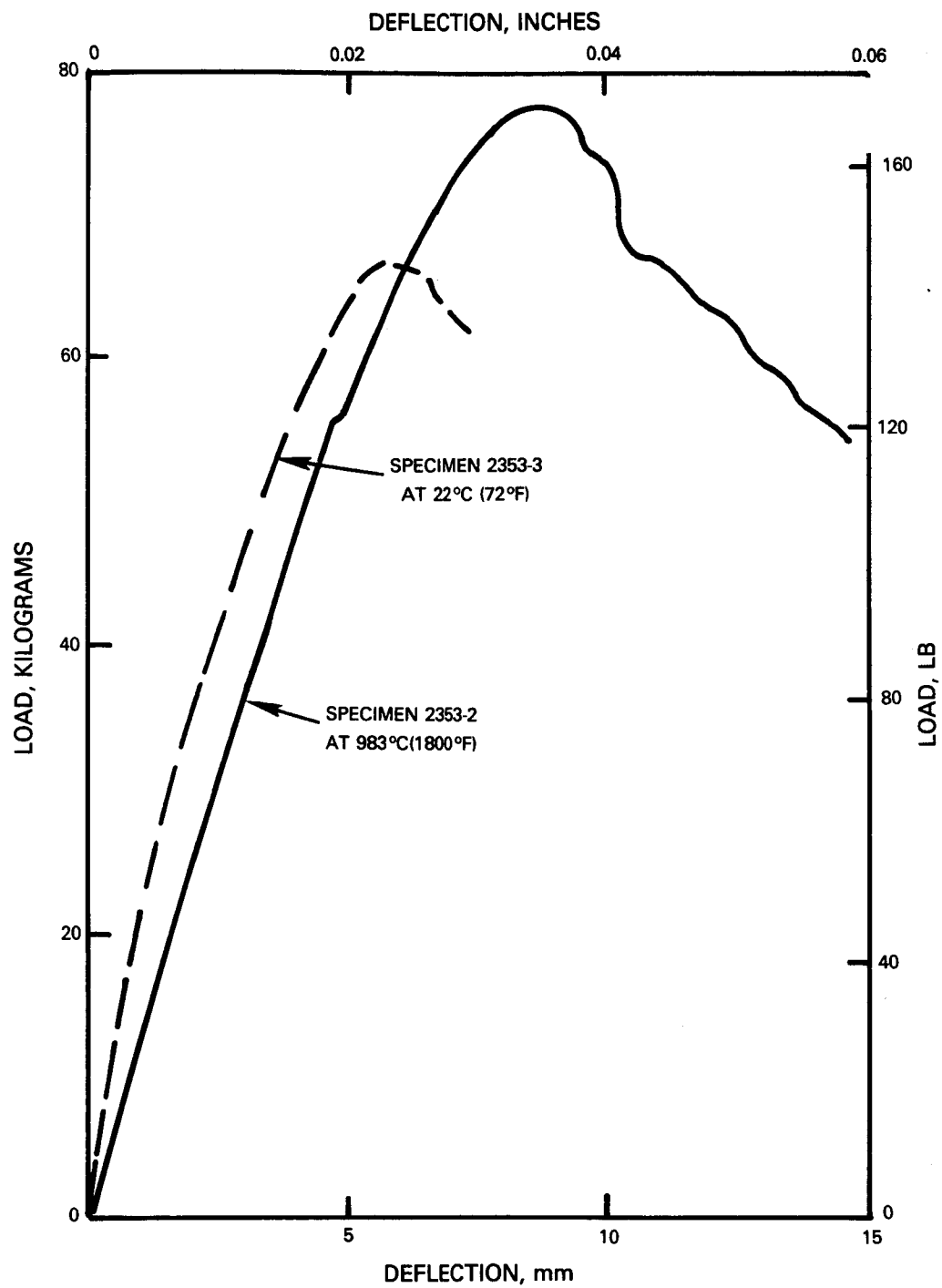
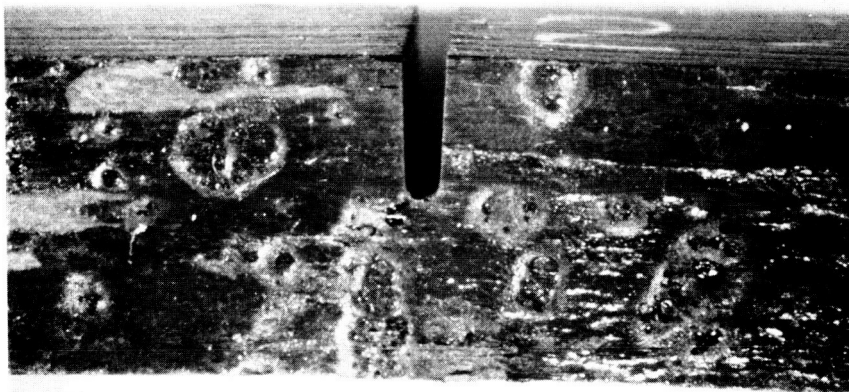
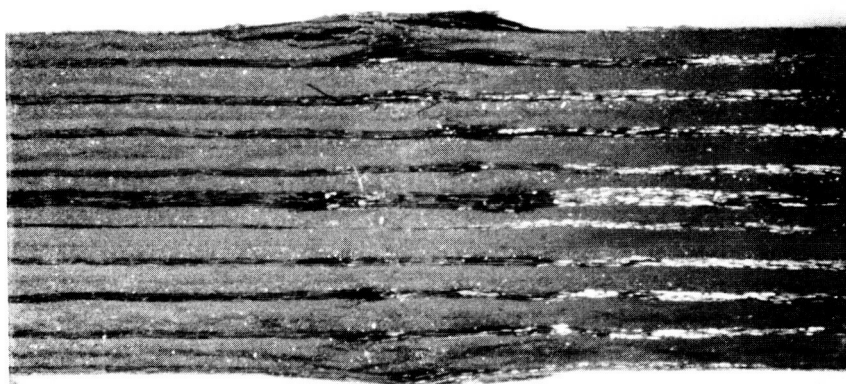


Figure 6-8 Typical Load-Deflection Characteristic for Notched SiC-LAS Specimens in Three Point Bending



Side view of specimen



View of loaded surface

Figure 5-9 Specimen 2353-2 After Bend Testing To Failure at 983°C (1800°F)

Table 6-V presents a summary of the failure load capacity of each of the test specimens. The flexural strength was calculated on the basis of the remaining cross sectional area of the specimen below the notch. At both temperature levels it appears that specimen strength is not degraded by the presence of the notch, and, in fact, the calculated stresses indicate an increase in notched specimen strength. This may relate to a combination of effects. First, the specimens are truly notch insensitive, as indicated by the crack path. Second, the 45° fibers extend up into the specimen notch shoulders and this may add additional resistance to specimen bending. It is also noteworthy that specimens tested at the 982°C (1800°F) test condition had higher strength and toughness than those evaluated at room temperature.

Table 6-V
Three Point Bend Strength of SiC-LAS Material

Specimen Number	Notch	Test Temperature °C (°F)	Flexure Stress at Failure MPa (ksi)
2352-4	No	22 (72)	378 (54.9)
2352-9	No	22 (72)	398 (57.6)
2352-1	Yes	22 (72)	566 (82.1)
2352-2	Yes	22 (72)	564 (81.7)
2353-3	Yes	22 (72)	631 (91.6)
2353-9	No	982 (1800)	449 (65.0)
2353-10	No	982 (1800)	433 (62.8)
2353-1	Yes	982 (1800)	664 (96.3)
2353-2	Yes	982 (1800)	680 (98.6)
2352-3	Yes	982 (1800)	590 (85.6)

The fatigue tests on the notched specimens were also conducted in the three point flexural test apparatus. The load on the specimens was varied cyclically with a maximum to minimum load ratio of ten at a frequency of about 5 Hz for test durations up to 10,000 cycles. Tests were conducted at both room temperature and at 982°C (1800°F). The maximum of the cyclic load applied on the specimen was between 50 and 85 percent of that producing failure in a similar notched specimen during the preceding static tests. In each case traces of the specimen load-deflection curve were recorded on initial loading and at specified intervals. These traces, and net unnotched specimen dimensions, were used to calculate effective composite elastic moduli. Thus, the relative specimen stiffness could be tracked as a function of fatigue. Table 6-VI presents a summary of the results of this sequence of tests.

Table 6-VI
Results of Notched SiC-LAS Specimen Fatigue Tests

Specimen Number	Test Temperature °C (°F)	Stress at Maximum Loading MPa (ksi)	Specimen Stiffness at Cycle				Cycles to* Failure Nf Cycles	Residual Strength MPa (ksi)	
			1	100	1000	10,000			
2352-5	22 (72)	353 (51.2)	30.4 (4.4)	25.6 (3.7)	25.6 (3.7)	25.6 (3.7)	Run Out	544 (78.8)	
2352-6	22 (72)	400 (58.0)	32.5 (4.7)	31.0 (4.5)	29.7 (4.3)	28.3 (4.1)	Run Out	534 (77.4)	
2352-7	22 (72)	446 (64.6)	29.0 (4.2)	27.6 (4.0)	27.6 (4.0)	26.2 (3.8)	Run Out	575 (83.3)	
2352-8	22 (72)	483 (70.0)	31.8 (4.6)	25.6 (3.7)	24.2 (3.5)	22.1 (3.2)	Run Out	537 (77.8)	
2353-4	982 (1800)	331 (48.0)	25.6 (3.7)	22.1 (3.2)	20.7 (3.0)	19.3 (2.8)	Run Out	566 (82.0)	
2353-5	982 (1800)	372 (54.0)	24.2 (3.5)	21.4 (3.1)	20.0 (2.9)	-	5,940	-	
2353-6	982 (1800)	415 (60.2)	26.9 (3.9)	-	-	-	1,000	-	
2353-7	982 (1800)	374 (54.2)	20.7 (3.0)	24.2 (3.5)	-	-	480	-	
2353-8	982 (1800)	326 (47.2)	31.0 (4.5)	21.4 (3.1)	20.7 (3.0)	-	4,440	-	

*Run Out indicates completed the 10,000 cycle test duration without failure.

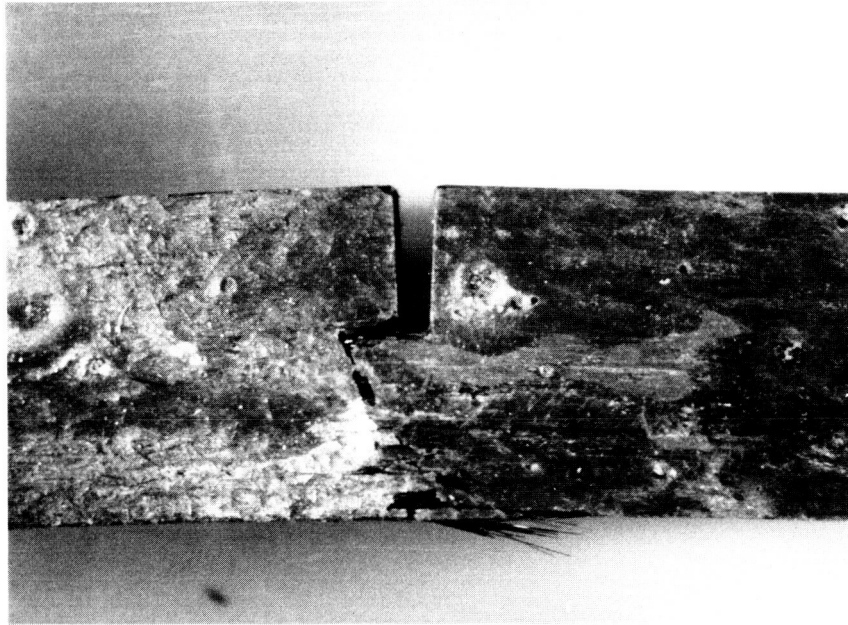
The results indicate that all of the specimens tested at room temperature survived the 10,000 cycle maximum test duration while only one of the four specimens evaluated at the 982°C (1800°F) temperature level did so. The data also indicate a gradual reduction in the stiffness with number of cycles for the specimens evaluated at both temperature levels. The major reduction occurred in the first few cycles and was followed by a much more gradual reduction. At room temperature this decrease in stiffness is probably relatable to the occurrence of matrix and interlaminar microcracking, but not to any major structural change since all room temperature test specimens survived the 10,000 fatigue cycles imposed.

Measurements were made of the residual strength of the specimens that did not fail during the cyclic fatigue tests, and the results are also listed on Table 6-VI. Comparison with the corresponding data for nonfatigued specimens on Table 6-V indicates that specimens which were fatigue tested at room temperature did not experience any significant decline in ultimate strength. Conversely, the single specimen that survived the 10,000 cycle duration of the fatigue test at 982°C (1800°F) had a residual strength about ten percent less than unfatigued specimens tested at the same temperature.

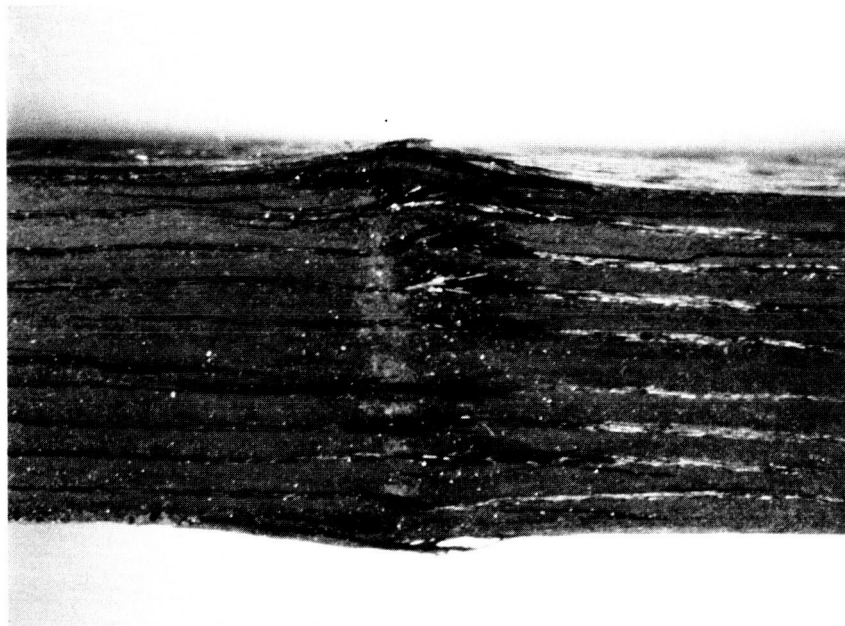
Figure 6-10 shows one of the specimens after failure in the residual strength measurement after having sustained 10,000 cycles of fatigue loading. The fracture morphology is typical of specimens which were examined for residual strength after surviving the fatigue tests in that it was comparable to that of the monotonically loaded nonfatigued specimens (such as that of Figure 6-9) and showed no evidence of large scale fatigue damage. These results show the very tough and fibrous nature of the crack path indicating good retention of crack growth resistance.

6.5 Thermal Fatigue Tests

Thermal fatigue tests were conducted on specimens of the SiC-LAS composite material on a test rig located in the Materials Engineering Laboratory at Pratt & Whitney. This apparatus, shown schematically on Figure 6-11, has the capability to substantially reproduce localized creep-buckling failures (bulges) similar to those observed in engine operated burner liners. Testing involves repetitive creation of a small diameter high temperature hot spot in the center of a rotating 7.62 cm (3.0 in) diameter test specimen using a focused oxy-acetylene torch. The cyclic heating is caused by shuttling the torch laterally into and out of position in front of the specimen. The frequency of the shuttling depends on the properties of the test material and the desired temperature excursions but is typically one to eight cycles per minute.



Side view of specimen



View of loaded surface

Figure 6-10 Specimen 2352-5 After 10,000 Cycles at Room Temperature and Residual Strength Test

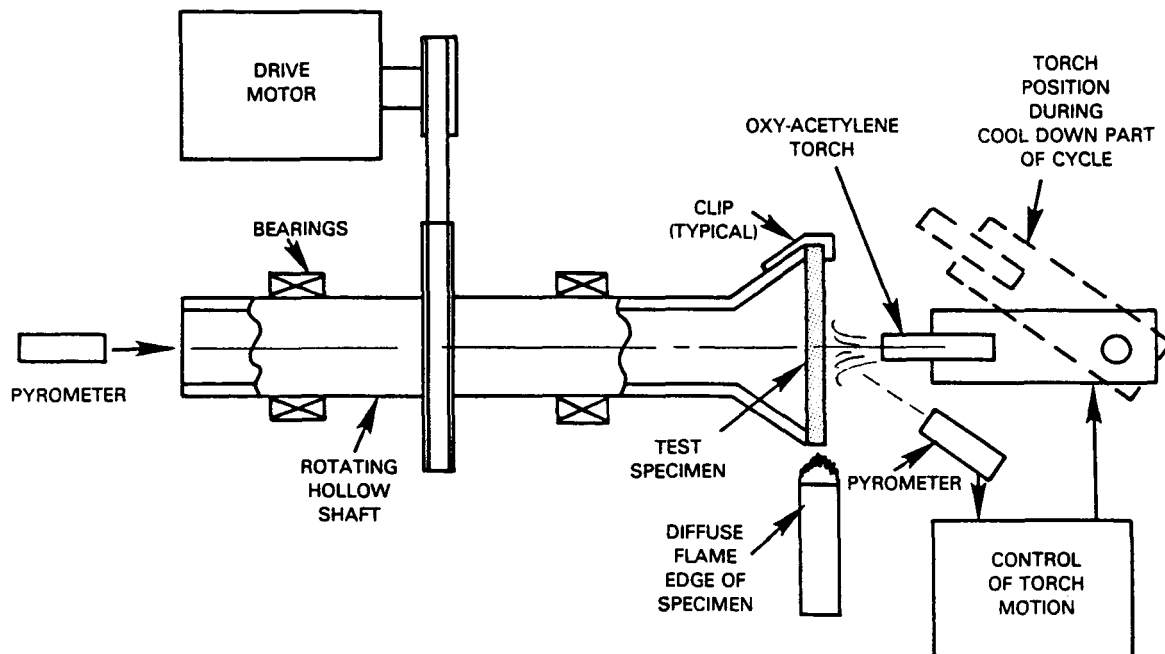


Figure 6-11 Schematic View of Thermal Fatigue Test Apparatus

The temperatures of the hot and cold surfaces of the specimen are measured by Irkon pyrometers - one sighting the front face of the specimen disk and another sighted through the bore of the specimen holder at the back side of the rotating disk. The periphery of the disk is heated with a diffuse gas-air flame and is controlled to a temperature of the order of 540°C (1000°F). The rotation of the specimen provides an axisymmetric temperature distribution. The speed of rotation is typically 400 rpm.

During company sponsored tests with metallic materials, cycling the center of the disk from the 540°C (1000°F) temperature maintained at the periphery to a maximum temperature in the range of 870°C to 1090°C (1600°F to 2000°F) was found to produce a progressive permanent deflection of the disk surface which was measured periodically by a recording profilometer. The total accumulated amount of deflection is a function of the number of thermal cycles experienced, the disk edge-to-center maximum temperature difference and the physical and mechanical properties of the disk material. To date this test has been used to provide relative measurement of the capability of metallic sheets to resist localized buckling when subjected to cyclic thermal conditions in a combustor environment.

A total of six specimens of SiC-LAS were evaluated on the thermal fatigue rig. The operating conditions of the rig, test durations and comments on the condition of the specimens after test are summarized on Table 6-VII. Three of the specimens were evaluated under the contract reported herein while the others were tested under a concurrent company sponsored program. One of these specimens was fabricated with a different LAS matrix composition that was expected to lead to improved high temperature capability. Table 6-VII lists the tests in the order in which they were conducted and the results are discussed below in that order.

Table 6-VII

Results of Thermal Cyclic Fatigue Test on
0°/45°/-45°/90° SiC-LAS Composite

Specimen	Configuration	Thickness mm (in)	Max Hot Side Temperature °C (°F)	Max Through Thickness Temp Difference °C (°F)	Thermal Cycles Tested	Total Time At Hot Surface Temp Above 980°C (1800°F) Minutes	Comments
1	Base	1.15 (0.045) (8 layers)	1095 (2000)	222 (400)	1000	18.5	Surface distress limited to slight discoloration and glass beading on hot side.
2*	Base	1.15 (0.045) (8 layers)	1150 (2100) 1150 (2100)	108 (195) 145 (260)	500 1900	144.1	Surface distress limited to slight discoloration and glass beading on hot side. Sectioning revealed no internal distress.
3*	Base	1.15 (0.045) (8 layers)	1150 (2100)	108 (195)	3500	175.0	Surface distress included minute surface cracks, discoloration and glass beading on hot side. Sectioning revealed slight internal microcracking.
4*	Slotted	1.15 (0.045) (8 layers)	1150 (2100)	72 (130)	2400	85.0	Surface distress limited to slight discoloration and glass beading on hot side. More extensive internal microcracking near slot edge.
5	Base	2.30 (0.090) (16 layers)	1095 (2000) 1150 (2100) 1205 (2200)	340 (610) 322 (580) 333 (600)	100 1000 138	45.3	Surface damage incurred during exposure at 1205°C (2200°F) to depth of 0.13 mm (0.005 in). More extensive glass beading of hot surface at larger radii around hot spot.
6	Improved LAS	2.42 (0.095) (16 layers)	1150 (2100) 1205 (2200) 1261 (2300) 1317 (2400)	256 (460) 278 (500) 278 (500) 396 (712)	500 500 500 2500	412.5	Surface distress limited to slight cracking, and discoloration of hot side with minimal glass beading.

*Tested under contract

The first test specimen was evaluated by subjecting it to cyclic operation between 537°C (1000°F) and 1095°C (2000°F) during which the through thickness temperature differential at the center of the disk was 222°C (400°F) at the time of peak front surface temperature. (For reference purposes, the prior company sponsored research indicated that at peak hot side surface temperatures of the order of 1040°C (2000°F) Hastelloy X specimens developed sizable central deflections after only five or ten thermal cycles and that cracks developed on the hot side surface after about 500 cycles. Due to its higher thermal conductivity, the temperature differential through the Hastelloy X specimen was also an order of magnitude less than that in the SiC-LAS specimen.) Conversely, no such distress was encountered in the evaluation of the first SiC-LAS specimen and the test was terminated after 1000 thermal cycles. Profilometer measurements indicated no deflection or change in thickness of the specimen and the only evidence of its exposure was a local discoloration of the surface of the specimen. The color change appeared as a light grey against the darker grey normal color of the material. The discoloration was limited to an area of about 12.7 mm (0.5 in) diameter where the hot jet impinged. This was surrounded by a ring that appeared to consist of minute beads of glassy material. Figure 6-12 shows the surface of Specimen 2 after more extensive testing and is representative of the surface distress incurred on Specimen 1.

The second specimen evaluated in the thermal fatigue rig was subjected to more severe conditions in that the maximum hot side temperature was increased 55°C (100°F) above that encountered by Specimen 1 and the test was extended to 2400 thermal cycles. While the through thickness temperature differential was not as severe as in Specimen 1, the thermal cycle was modified to provide an order of magnitude higher total time at surface temperatures above 980°C (1800°F). The results of the tests were comparable to those of Specimen 1 in that there was no deflection or change in thickness of the specimen, and the only evidence of its thermal exposure was the surface discoloration and glass bead formation shown on Figure 6-12. After testing, this specimen was sectioned along a diameter and photomicrographs were taken of the exposed surface. As shown on Figure 6-13, photographs at 50 and 100 times magnification reveal no internal distress in the composite material.

The remarkable performance of the SiC-LAS specimens relative to metallic materials in the thermal fatigue rig is attributable to the lower thermal stress associated with its low coefficient of thermal expansion. However, Specimen 2 was also exposed to temperatures of more than 125°C (250°F) higher than those at which material deterioration is known to begin as cited in Section 5.0. Its survival at higher temperatures for even the short exposure period in the thermal cycling rig gives reason for optimism that this material may have useful life at considerably higher temperature levels.

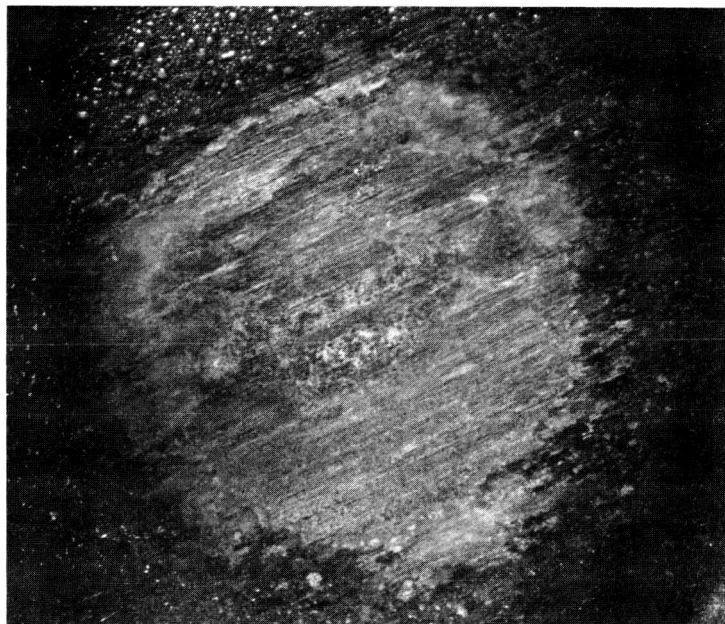
ORIGINAL PAGE IS
OF POOR QUALITY



COLD
SIDE



HOT
SIDE



HOT SIDE (CENTER)

3X

Figure 6-12 Surface of Specimen 2 After Thermal Fatigue Testing for 2400 Cycles

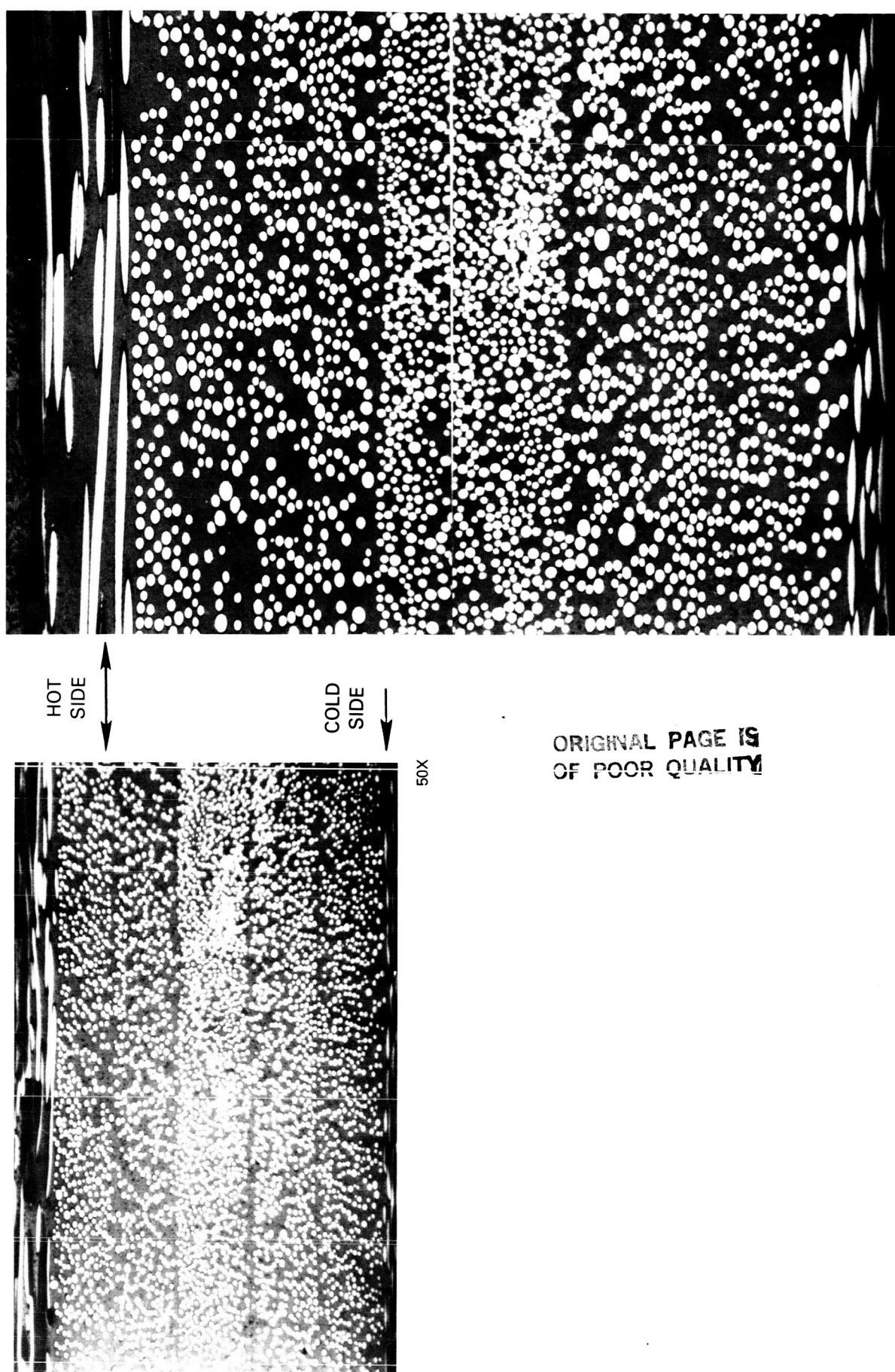


Figure 6-13 Photomicrographs of Diametral Section of Specimen 2 After Thermal Fatigue Testing

The third specimen was subjected to the same thermal cycling as the second but the duration was extended to 3500 cycles in an attempt to induce internal thermal fatigue distress in the specimen. At the conclusion of the test there was still no evidence of deflection or change in thickness of the specimen. However, visual examination revealed what may have been surface cracks rather than just discoloration in the jet impingement area in the center of this disc. Following the test, this specimen was also sectioned along a diameter and examined by photomicrography. As shown on Figure 6-14, this specimen was found to have a few internal microcracks.

The fourth thermal cyclic test specimen was made with a 5.08 cm (2.0 in) long by 1.27 mm (0.050 in) wide diametral saw cut through the center of the disk. When tested in the thermal cycling rig this specimen simulated the downstream end of a liner panel. Relative to the preceding specimens the conditions were more rigorous because the periodically heated area was less constrained and the edge of the material was directly exposed to the cycling high temperature environment. This specimen was tested over the same thermal cycle as Specimens 2 and 3 for a total test duration of 2400 cycles. Visual examination at the conclusion of the test indicated that the response of this specimen was essentially identical to the first in that the only evidence of its being subjected to the thermal cycling was the discoloration of the hot side surface in the jet impingement area. However, after sectioning near the diametral cut, photomicrography of the exposed ends of the material revealed more extensive microcracking between the first two layers of the material at the hot side surface as shown on Figure 6-15.

On completion of these thermal cycling tests, Specimens 3 and 4 were cut into a series of strips that could be tested in flexure to determine the residual strength of the SiC-LAS after thermal exposure. As shown on Figure 6-16, after removing a section for examination by photomicrography and discarding the ends, the remainder of the disc was cut into seven strips, each 5.08 mm (0.20 in) by 1.15 mm (0.045 in) in cross section with the silicon-carbide fibers in the surface layers aligned parallel to the length of the specimen. Each specimen was tested to failure at room temperature in three point flexure in a loading geometry identical to that of the mechanical fatigue tests of Section 6.4. The specimens were alternated in positioning the surface which had been the hot surface in the thermal fatigue test rig as the tension or compression side in the flexure test. The results of Section 6.4 indicated that unnotched specimens had surface failure stresses of 378 and 398 MPa (54.9 and 57.6 ksi) when loaded at room temperature. By comparison, the residual strength of most of the specimens cut from the thermal fatigue test discs, and in particular those from near the center of the disc which had been exposed to the highest temperatures, had considerably higher residual strengths. This lends further support to the observation of Section 6.3 in which specimens that had been exposed to high temperatures during creep tests were stronger than unheated virgin specimens. However, it must also be noted that the cross section shape of the strips cut from the discs was different from the specimens of Section 6.4 which may have also influenced their load carrying capacity.

ORIGINAL PAGE IS
OF POOR QUALITY

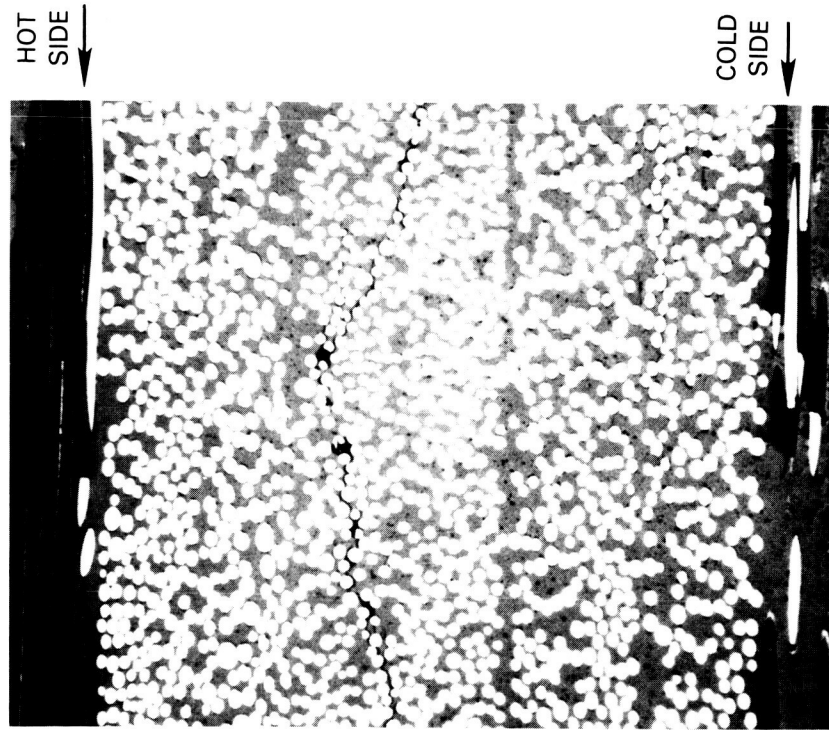
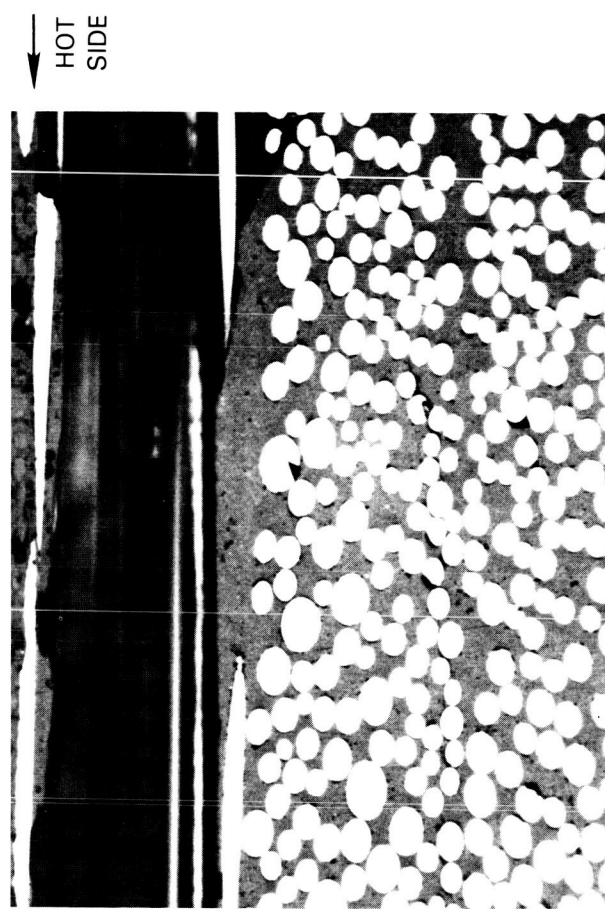
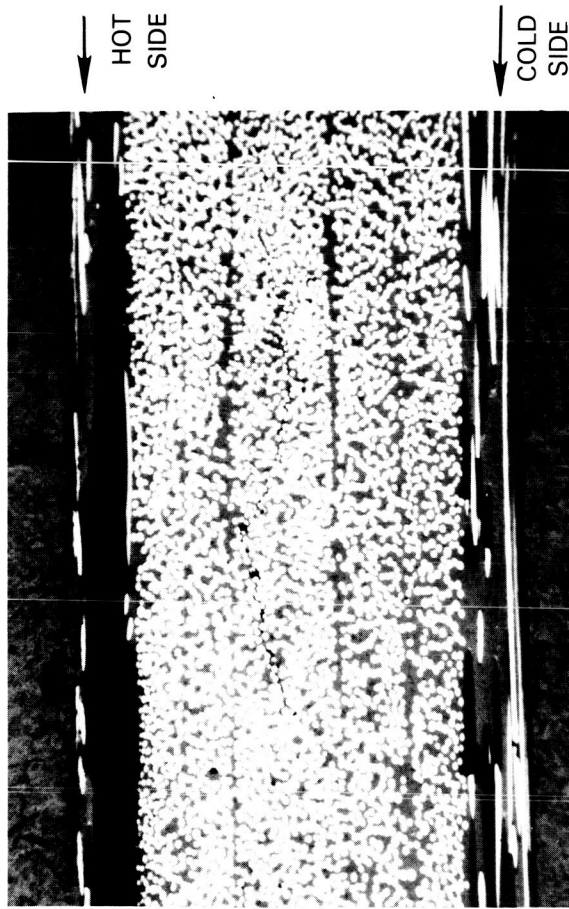
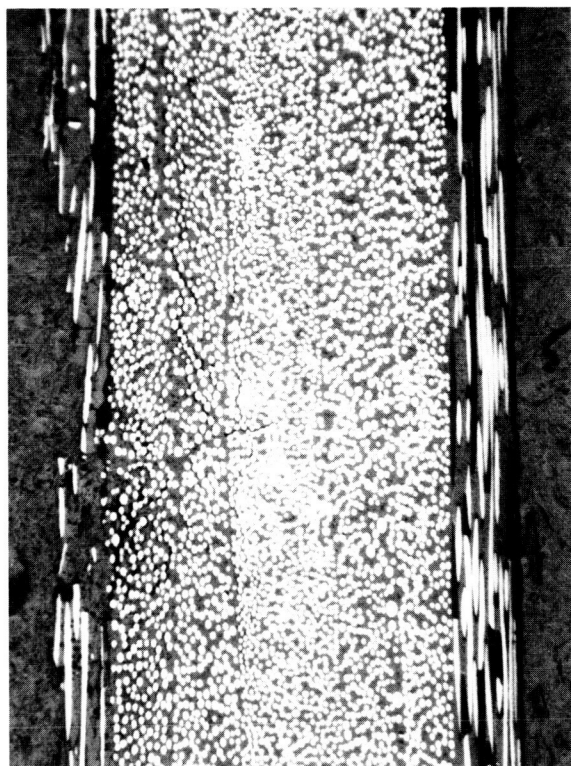


Figure 6-14 Photomicrographs of Diametral Section of Specimen 3 After Thermal Fatigue Testing

ORIGINAL PAGE IS
OF POOR QUALITY

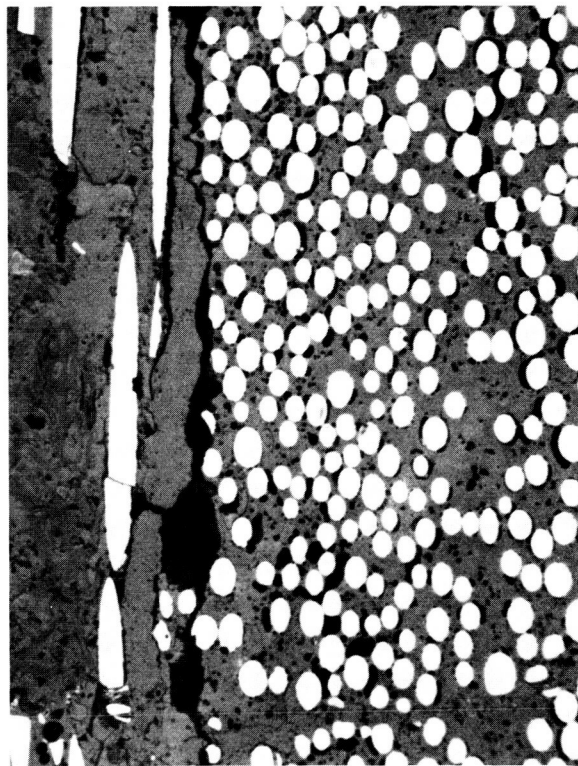
→ HOT
SIDE



50X

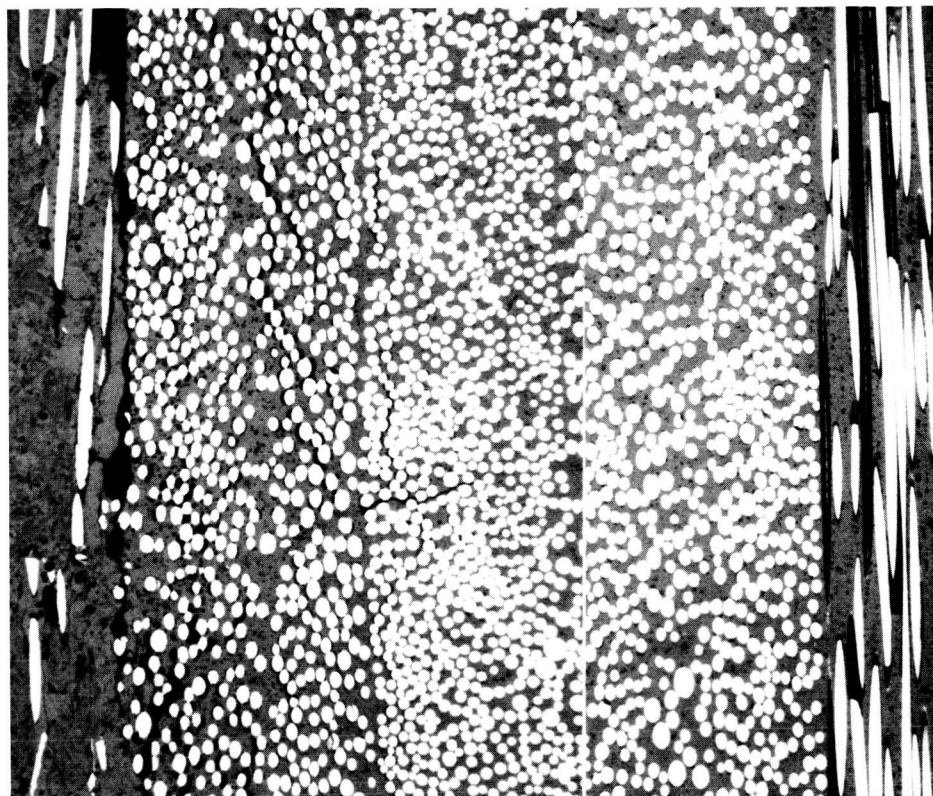
COLD
SIDE →

→ HOT
SIDE



200X

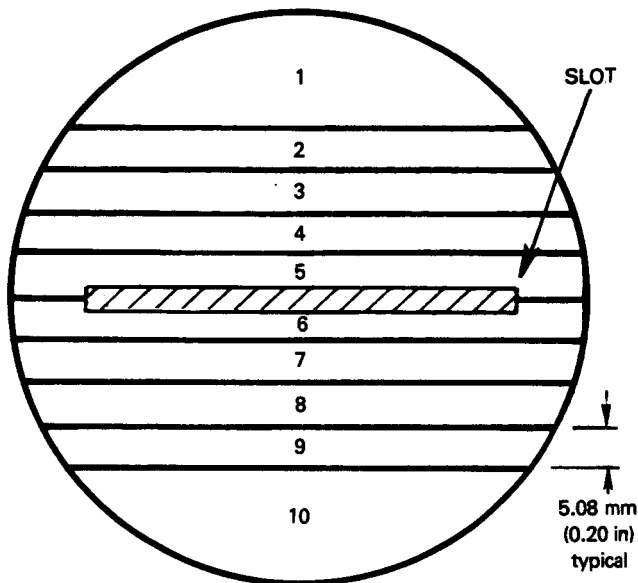
→ HOT
SIDE



100X

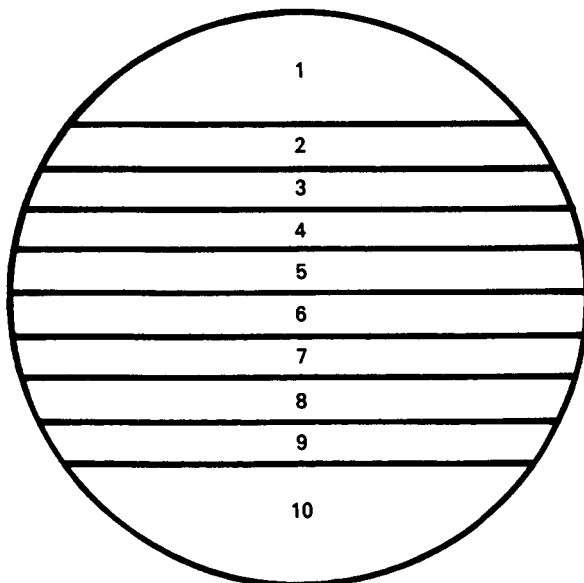
COLD
SIDE →

Figure 6-15 Section of Thermal Fatigue Specimen 6 Near Edge of Slot



SPECIMEN 4

SAMPLE	TENSION SIDE	RESIDUAL STRENGTH,	
		KSI	MPa
2	HOT	74	510
3	COLD	57	393
4	HOT	81	559
5	COLD	78	538
6	—	SECTIONED	
7	HOT		
8	COLD	71	490
9	HOT	63	435



SPECIMEN 3

SAMPLE	TENSION SIDE	RESIDUAL STRENGTH,	
		KSI	MPa
2	HOT	49	338
3	COLD	38	262
4	HOT	72	496
5	—	SECTIONED	
6	COLD		
7	HOT	68	469
8	COLD	33	228
9	HOT	58	400

Figure 6-16 Residual Strength of SiC-LAS Panels Cut from Thermal Fatigue Test Specimens

Despite having operated at instantaneous surface temperatures as high as 1150°C (2100°F), the distress on the hot side surface of the first four thermal fatigue test specimens evaluated was limited to only discoloration of that surface. The test sequence for the fifth specimen was extended to higher temperature levels to determine the threshold at which significant surface distress would occur and the nature of this distress. As shown on Table 6-VII, after initial exposure to maximum surface temperatures of 1095°F to 1150°C (2000°F to 2100°F) for 1100 thermal cycles, the maximum hot side surface temperature in the cycle was increased to 1205°C (2200°F). After 138 additional cycles of operation, the test was terminated when a small area at the center of the disc began to glow. Inspection revealed that cracks had developed in the surface in this area and the glow was suspected of coming from an exposed silicon-carbide fiber. The cracks were found to locally lift the surface of the material about 0.13 mm (0.005 in) as determined by a profilometer. The region of discoloration of the surface and the surrounding ring of glassy beads found on previously tested specimens was still present around the cracked area but extended to larger radii than on those specimens. The greater extent of surface distress experienced by this specimen must be attributed to mechanisms that occurred at temperatures between 1150°C and 1205°C (2100°F and 2200°F) because prior specimens operated for considerable times at maximum temperatures of 1150°C (2100°F) without encountering surface cracking. It is estimated that during the 138 cycles of operation at a peak surface temperature of 1205°C (2200°F) Specimen 5 encountered surface temperatures in excess of 1150°C (2100°F) over about 3.3 minutes. The cracking of the surface must have developed during this time interval.

The final specimen evaluated had a different matrix composition than those previously tested. The lithium aluminosilicate used for the matrix was of a different composition which was thought to lead to higher temperature capability. The test sequence for this specimen was established to explore this capability. As shown on Table 6-VII, after initial operation at a maximum hot side temperature of 1150°C (2100°F) for 500 cycles, the severity of exposure was increased in increments of 55°C (100°F) of maximum hot side temperature until 1317°C (2400°F) was attained. Finally, after 2500 thermal cycles of operation at this maximum hot side temperature, distress was observed on the hot side surface of the specimen. The distress appeared as minute surface cracks in the center of the torch jet impingement area which had the characteristic light grey discoloration. The formation of a ring of glass beads around the discolored area as on the previously tested specimens was also evident, but the beads appeared to be considerably fewer in number and smaller than on the other specimens.

Based on the results of the evaluation of Specimen 6, it appears that the improved lithium aluminosilicate material used in this specimen has potential for substantially improving the thermal capability of SiC-LAS composites. While in the early stages of material development at the time the contracted program was conducted, it appears to have the capability of withstanding temperatures 100°C to 125°C (200°F to 250°F) higher than the SiC-LAS constructed with the current matrix composition.

6.6 Surface Radiant Emissivity

To assure that the pyrometers used to determine the specimen surface temperatures in the thermal cyclic rig were providing accurate measurements with the SiC-LAS material, parallel measurements were made with several types of pyrometers operating at different wavelengths. These measurements not only confirmed that the surface temperatures quoted in Section 6.5 were accurate within $\pm 14^{\circ}\text{C}$ (25°F) but also provided definition of the radiant emissivity of the surface of the material-information that was needed for thermal analyses during the design studies of Section 7.0. Figure 6-17 shows the spectral distribution of surface emissivity of the SiC-LAS material which exhibits a slight decrease with increasing wavelength. An average value of 0.86 was selected for the thermal analyses.

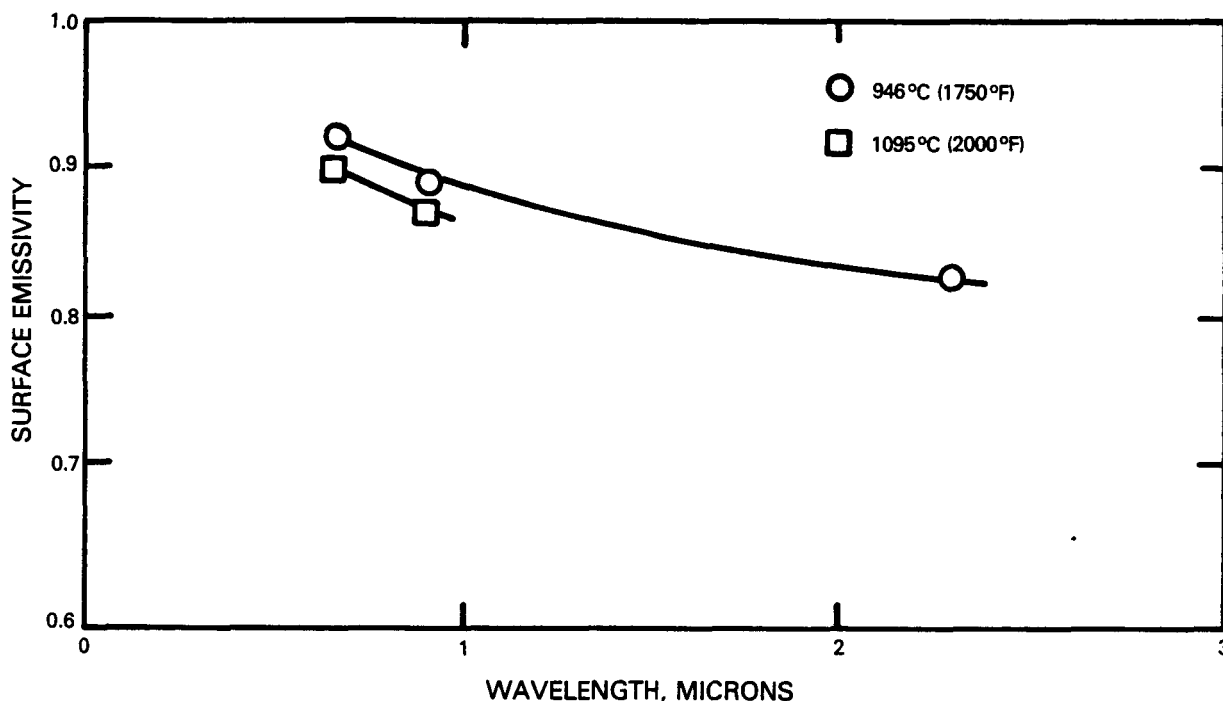


Figure 6-17 Surface Emissivity of SiC-LAS Composite Material

6.7 Thermal Expansion

A Theta Industries differential mode dilatometer was used to measure the change in specimen length as a function of temperature over the ambient temperature to 995°C (1825°F) range. The measurements were made in the plane parallel to the layers of fibers on two specimens 5.08 cm (2.0 in) long. Figure 6-18 shows the thermal expansion characteristic of a representative specimen and indicates that the expansion is linear to about 700°C (1290°F) above which it tends to expand at a greater rate. Each of the specimens was evaluated three times over the heating and cooling cycle of Figure 6-18, and the mean coefficients of expansion between room temperature and 995°C (1825°F) are listed on Table 6-VIII. The low levels measured are consistent with the data of Section 5.0 and, as demonstrated in the cyclic thermal fatigue tests of Section 6.4, are conducive to low thermal stress levels.

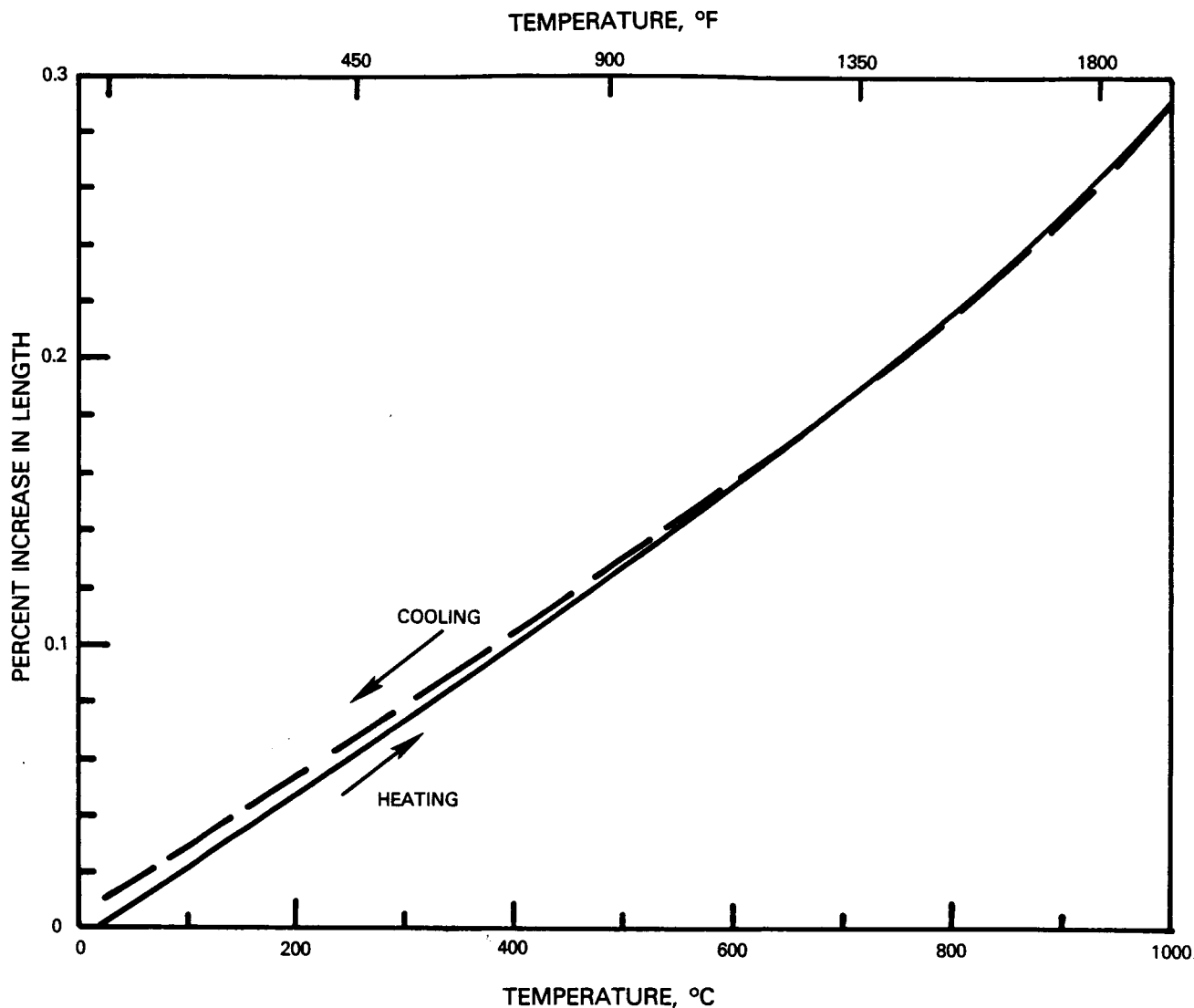


Figure 6-18 Thermal Expansion of SiC-LAS Composite Material

Table 6-VIII

Coefficient of Thermal Expansion of SiC-LAS Composite Material

	Specimen 1		Specimen 2	
	Per °C	Per °F	Per °C	Per °F
Run 1	2.96×10^{-6}	1.65×10^{-6}	2.99×10^{-6}	1.66×10^{-6}
Run 2	2.87×10^{-6}	1.60×10^{-6}	2.94×10^{-6}	1.63×10^{-6}
Run 3	2.76×10^{-6}	1.53×10^{-6}	2.97×10^{-6}	1.65×10^{-6}
Average	2.863×10^{-6}	1.593×10^{-6}	2.967×10^{-6}	1.646×10^{-6}

6.8 Thermal Conductivity

Measurements were made of the thermal conductivity of the SiC-LAS composite in the through thickness direction, i.e., perpendicular to the plane of the fibers. The measurements were made at Virginia Polytechnic Institute using a laser flash diffusivity technique. The specimens used for these measurements were cut from 2.35 mm (0.0925 in) thick panels. Direct transmission of the laser beam was prevented by coating the specimen surfaces with carbon. The transient temperature response of the specimen rear surface was monitored by optical means. For measurements above room temperature, the specimens were heated in a carbon resistance furnace with a nitrogen atmosphere. In the evaluation of the thermal diffusivity from the transient temperature response, corrections for heat loss were made and changes in specimen thickness with temperature due to thermal expansion were taken into account.

The specific heat of the fibers and the glass-ceramic matrix have been determined by differential scanning calorimetry using a Dupont 990 Thermal Analyzer. From the measured value of the thermal diffusivity, the corresponding value of the composite thermal conductivity (K) was calculated from:

$$K = k\rho C \quad (6-3)$$

where k is the thermal diffusivity, ρ is density and C is the specific heat. The specific heat of the composite was calculated from existing measured values for the specific heat of the fibers and the matrix by means of the rule of mixtures. The thermal conductivity of two specimens was evaluated over the temperature range from ambient to 995°C (1825°F). The results confirmed the low level of thermal conductivity of this material projected in Section 5.0. At 25°C (77°F) the conductivities of the two specimens were 1.69 and 1.73 W/m°K (0.976 and 1.00 BTU/hrft°F), while at 995°C (1825°F) they were 2.32 and 2.33 W/m°K (1.34 and 1.346 BTU/hrft°F). The data demonstrated a linear variation between these temperatures and comparable levels were observed when the specimen was being progressively heated toward the 995°C (1825°F) temperature level and during the subsequent cooldown as shown on Figure 6-19.

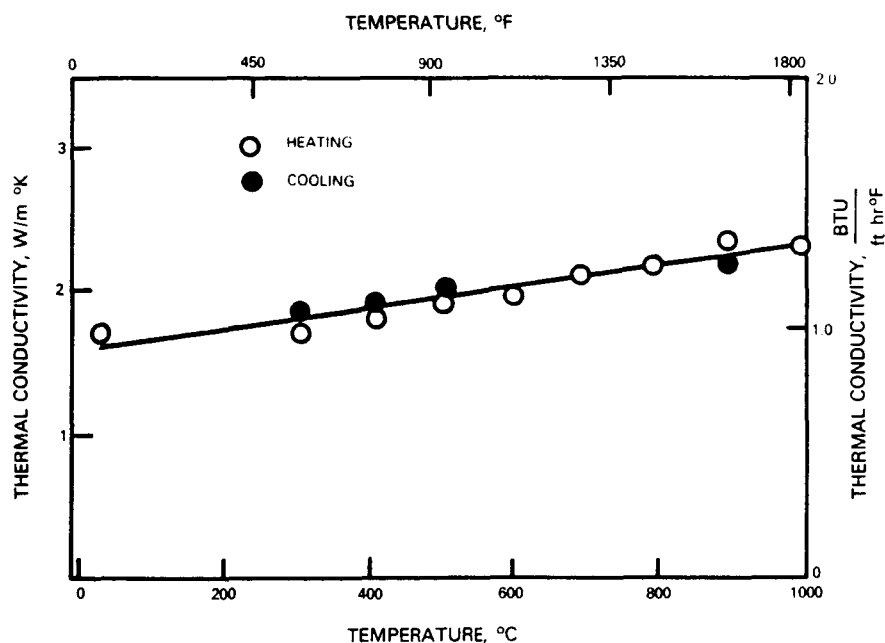


Figure 6-19 Thermal Conductivity of SiC-LAS Composite Material

SECTION 7.0

COMPOSITE COMBUSTOR LINER DEFINITION AND ANALYSIS

This section describes the conceptual definition of the combustor liner fabricated from the SiC-LAS composite and the subsequent thermal and structural analyses conducted to define its structural integrity and performance potential. Due to the unique thermal properties of the ceramic SiC-LAS material, and in particular its low thermal conductivity with respect to metals, it was apparent from the onset that different aerothermal design approaches would be required in incorporating this material in a combustor liner. Consequently, this effort was initiated with a fundamental aerothermal study to establish the optimum thermal design approach. This led to the identification of four different combustor liner design concepts which were screened to select the most promising configuration consistent with design constraints and near term composite fabrication capabilities. Extensive thermal and dynamic as well as static structural analyses were conducted of this configuration and a composite liner life prediction model was formulated.

7.1 Preliminary Aerothermal Study

From the data presented in Section 5.0 and 6.0 it is recognized that the thermal conductivity of SiC-LAS, being typical of nonmetallic composites, is low, of the order of 15 to 20 percent of that of the metals normally used in combustor liners. Consequently, the ability to cool the segment by convection on the back surface, which was the dominant cooling mechanism for the metallic segmented liner of Section 4.0, is doubtful and a preliminary thermal analysis of this and other cooling approaches was initiated with the objective of defining the best overall aerothermal design approach consistent with the use of this material.

The study was initiated by applying the thermal analysis to a convective-film cooled segmented liner construction geometrically identical to the baseline metallic liner of Section 4.0. However, the segments were assumed to be fabricated from the SiC-LAS composite material and the thermal calculation of Section 4.0 was merely repeated with the requisite physical properties of SiC-LAS substituted for those of the Modified B-1900 segment. During the studies of Section 4.0, the thermal analysis had indicated that the nominal circumferential average surface temperature at the downstream end of the metallic liner segment would be about 968°C (1775°F). This temperature was projected to increase to about 1315°C (2400°F) with the use of the composite material. Obviously, the ability to cool segments by convection on the rear surface is severely impeded by the low thermal conductivity. Furthermore, despite the reduced heat flux through the segment, the through thickness temperature differential in the liner segment was predicted to be about 375°C (670°F) across the thickness as opposed to 25°C (45°F) in the segments of the baseline metallic liner. The analysis also revealed that, due to the low thermal conductivity, the pin-fin extended surface employed for heat transfer augmentation in the metallic liner was completely ineffective when the segment was made of the

composite material. Since this extended surface also could not be readily fabricated in the composite material, when the direct material substitution was considered as one of the candidate liner configurations, it was done so with the assumption that the pin-fins were eliminated and replaced with more readily fabricated axial ribs to maintain adequate segment to shell gaps. The resultant configuration is shown on Figure 7-1.

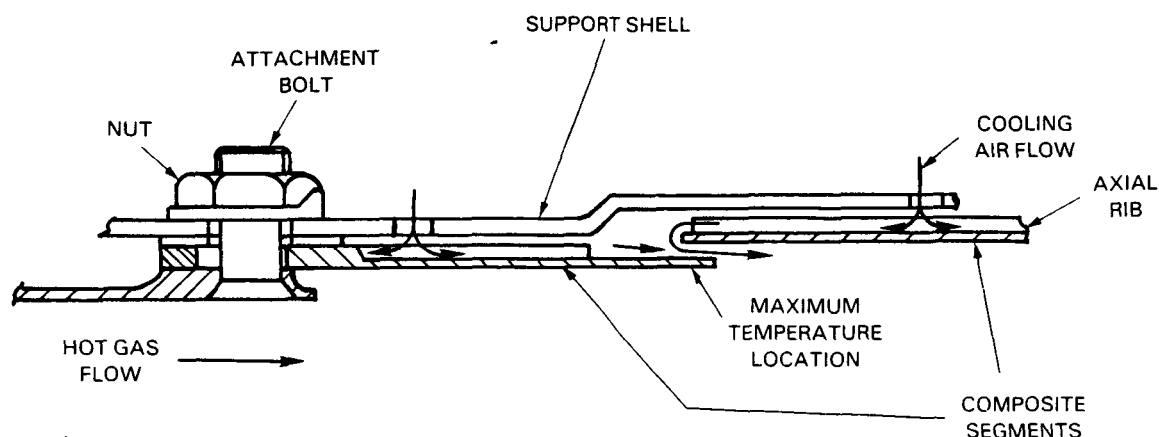


Figure 7-1 Segmented Liner Design Using Composite Material Substitution (Subsequently Designated Concept 1)

While the magnitude of the through thickness temperature gradient in the lip of the composite segment in this configuration is extremely high, it must be noted that the coefficient of thermal expansion of SiC-LAS is an order of magnitude less than that of metals and the elastic modulus is about one-half that of the metals. Both of these factors will proportionally reduce the thermal stress associated with the through thickness temperature gradient. Furthermore, the thermal cyclic fatigue tests reported in Section 6.5 provide an indication of the ability of the SiC-LAS material to sustain high through thickness temperature gradients. At this point in the study, the predicted high levels of gas side surface temperature are a greater concern than are the gradients through the thickness.

Due to the limited ability to cool the composite liner segments by extracting heat from the rear surface, the thermal analysis was directed at evaluating means of isolating the liner from the hot combustion gases by enhancing the film cooling of the gas side surface. A parametric analysis was conducted to assess the trade-off of emphasis on film cooling the gas side as opposed to convective cooling of the rear surface of the low conductivity segment. The analysis was conducted for liner panels having a cooled length of 3.56 cm (1.40 in) which is identical to that of the segments in the baseline metallic liner defined in Section 4.0. The composite panels were assumed to have a nominal thickness of 1.14 mm (0.045 in) because this corresponded to the eight ply layup of the SiC-LAS material as it was fabricated for the experimental phase of this program. As described in Section 6.1 this was the minimum thickness consistent with a symmetrical distribution of the $0^{\circ}/+45^{\circ}/-45^{\circ}/90^{\circ}$ fiber layup. The flow rate of cooling air to the panel was maintained equal to that

defined for the metallic segment in Section 4.2. Table 7-I presents the computed circumferential average gas side surface temperature at the lip of the liner panel and the through thickness temperature differential at that location for combinations of six different design parameters. Two variations of rear surface convective cooling are considered and are depicted in Figure 7-2. In the first case the heat removal from the rear surface is low and corresponds to a configuration with tangential flow of the cooling air behind the lip of the louver. Alternatively, higher heat removal could be achieved by admitting the cooling air radially through holes in the support shell to impinge on the rear surface of the louver lip and produce a higher heat transfer coefficient. (In the case of the metallic segment liner, the use of extended heat transfer surfaces led to an additional degree of enhancement of rear surface cooling not attainable with the low conductivity composite material.)

Table 7-I
Effect of Film and Rear Surface Heat Transfer
on Temperatures in Composite Liner

		Rear Surface Convection	
		Tangential Flow Low Heat Removal °C (°F)	Impingement High Heat Removal °C (°F)
Coolant Film Initiation	Ideal	T = 1187 (2170) ΔT = 194 (350)	T = 1120 (2050) ΔT = 316 (570)
	Realistic Advanced Technology Design Approaches	T = 1314 (2400) ΔT = 222 (400)	T = 1231 (2250) ΔT = 372 (670)
	Prior State of the Art Design Approaches	T = 1453 (2650) ΔT = 294 (530)	T = 1370 (2500) ΔT = 440 (792)

T = Average Gas Side Lip Temperature
 ΔT = Through Thickness Temperature Difference at Lip

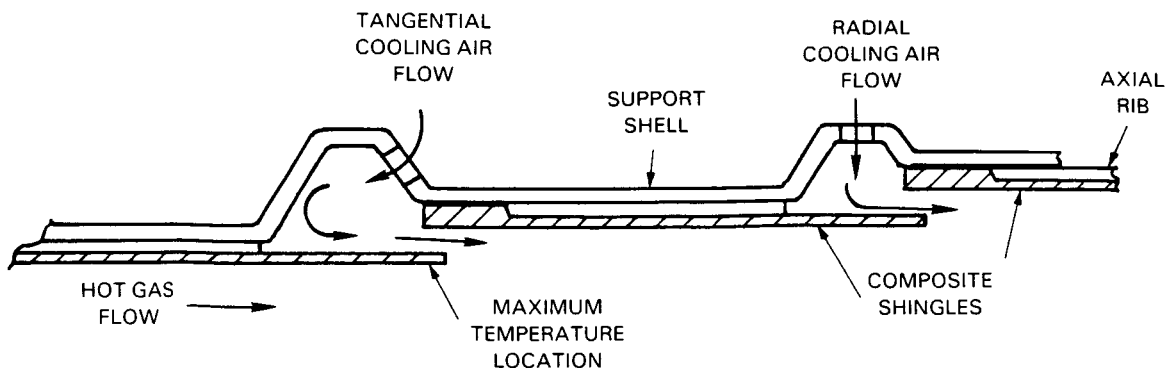


Figure 7-2 Floating Shingle Design Approach for Composite Liner

The effectiveness of the film cooling of the gas side of the panel depends on maintaining the integrity of the coolant film over the length of the panel. This is accomplished by introducing the coolant film in the most uniform possible state; the success of which is represented by three different design approaches in Table 7-I. The prior state-of-the-art is representative of sheet metal liner constructions in which cooling air is introduced to the louver through a multitude of circumferentially spaced holes. With short louver lips, the jets from the individual holes did not coalesce before discharging and the integrity of the film was low. Recent advanced technology design approaches have led to improved film cooling effectiveness by providing a means for the individual circumferentially spaced jets of cooling air to dissipate within the louver lip cavity so as to discharge as a more uniform layer. The "tangential cooling air flow" configuration of Figure 7-2 might approach this level of performance because the cooling air jets impinge on the opposite wall of the cavity before being discharged as a film. Finally, even higher film effectiveness levels have been achieved in laboratory experiments in which the coolant film is introduced from a large supply plenum through an aerodynamically smooth entrance channel. This last case is not considered realistic for the liner design study but was included in the analysis to reflect an upper limit for any future improvements.

The results of the analysis listed in Table 7-I indicate that, while the surface temperature of the louver lip may be reduced by increasing the rear surface convective heat transfer rate, greater reduction in surface temperature is achieved with improvements in the gas side coolant film effectiveness. Consequently, emphasis must be placed on the aerodynamic design of the coolant film introduction. The basic segmented liner design concept has evolved in a scenario where, with the use of high thermal conductivity metallic segments, the rear surface convection is the primary cooling mechanism and the film provides a secondary cooling function. Reversing this emphasis requires the use of a floating shingle type of liner construction such as shown in Figure 7-2. Like the segmented liner, the composite shingles consist of circumferential sectors that are attached to a support shell but are free to move relative to the shell to accommodate differential expansion. The shell of the liner in combination with the downstream ends of the shingles form cavities for the formation of the coolant film. As shown in Figure 7-2, cooling air can be admitted into these cavities to either swirl and provide a tangential flow over the rear surface of the composite panel or to impinge radially on that surface depending upon the extent of rear surface convective cooling desired. While the segmented liner concept of Figure 7-1 is constructed to allow convective cooling over the entire rear surface of the segment, only the downstream end of the panel is cooled on the rear side in the floating shingle design. However, the overall cooling is adequate because with film cooling the surface temperature of the panel increases in the axial direction and the rear surface cooling is concentrated in the regions which would otherwise have the highest temperature.

Based on the data of Table 7-I with the assumption that a film cooling effectiveness consistent with advanced technology liner design approaches can be maintained and that the rear surface of the louver lip will be impingement cooled, the average gas side lip temperature will still be about 1231°C (2250°F) and local hot streaks to 1254°C (2300°F) must be anticipated. In establishing a realistic design temperature limit for the SiC-LAS composite material, a review of the data accumulated during the Materials Screening phase of this task (as reported in Section 5.0) indicates that, as temperature is increased, the first degrading mechanism occurs at about 1000°C (1830°F) at which an interaction between the fibers and the matrix starts to weaken the fibers. Due to the presence of free carbon in the silicon carbide fibers, further increases in temperature could initiate oxidation of exposed fibers at temperatures of about 1200°C (2200°F). Finally, fusion of the current LAS matrix will occur at about 1300°C (2370°F). However, in setting a design temperature limit it must be recognized that distress caused by the onset of property degradation does not necessarily constitute a "failure" of the component involved because the progress of the deterioration mechanisms can be slow or the deterioration noncritical. Combustor liners, in particular, have accommodated local temperatures and stress levels at which oxidation occurs and/or cracks are initiated but do not progress to the severity of a "failure" over the service life. On the basis of this argument and the encouraging results obtained in the cyclic thermal fatigue tests described in Section 6.5 of this report, it does not appear overly optimistic to assume that the current SiC-LAS composite material can withstand local temperatures approaching 1200°C (2200°F) for extended periods of time. Furthermore, in view of the current rate of development in the field of ceramic composites, it appears that more advanced materials including derivatives of the current SiC-LAS with even higher temperature capability will be evolved in the period required to complete the development of a composite combustor liner. As an example, the improved SiC-LAS material evaluated in the cyclic thermal fatigue test sequence of Section 6.5 was not available at the initiation of this study but demonstrated exceptional cyclic fatigue and thermal exposure resistance at temperatures 110°C (200°F) higher than the current material. Consequently, for the purposes of defining composite combustor liner design concepts for this study, it is very reasonable and realistic to assume that the composite material will be capable of withstanding hot side surface temperature levels of 1250°C (2300°F) for significant periods of time. As will be shown in Section 7.3, this will permit designing of composite shingle type combustor liners with the same panel lengths and cooling air flow rates as the reference metallic segmented liner.

7.2 Composite Liner Concept Definition

The definition of the composite combustor liner was established by a process of screening multiple design concepts to select the best configuration. A total of four different design concepts were defined. For continuity purposes, the first of these involved simply material substitution in the segments of the reference metallic liner as described in Section 7.1. The other three concepts are basically new designs evolved from the point of view of a shingle type construction with enhanced film cooling of the hot side surfaces as advocated in the thermal analysis of Section 7.1.

The four liner design concepts are described below and the major advantages and disadvantages of each are discussed.

Concept 1 - Material Substitution in Reference Segmented Liner

As indicated above, Concept 1 was the basic convective-film cooled segmented liner construction defined in Section 4.0 with the SiC-LAS substituted for the cast metallic segments. The thermal analysis of the preliminary aerothermal studies described in Section 7.1 revealed that the pin-fin extended surface employed for heat transfer augmentation in the metallic liner was completely ineffective when the segment was made of the low conductivity composite material. Since this extended surface also could not be readily fabricated in the composite material, it was replaced with axial ribs to the extent needed to maintain adequate segment to shell gaps. This configuration is shown in Figure 7-1.

The multiple thickness configuration of the segment, with the axial spacing ribs and raised lugs at the attachment locations, introduces some fabrication complexities but they are within the capabilities of current ceramic composite forming techniques. The major drawback of this configuration is the incompatibility of the cooling approach with the low conductivity composite material. While some convective cooling would be achieved by the airflow behind the segments, the design offers limited opportunity for control of the critical coolant film on the hot side. The gap between overlapping segments controlling the thickness of the coolant film will vary substantially as the segments are loaded and distort. While such variations are acceptable in a metallic segment construction in which the dominant cooling mode is convection on the cold side of the segment, they could not be tolerated with a composite liner segment that relies on hot surface film cooling to a much greater extent.

The use of metallic attachment bolts bearing on the SiC-LAS material in a region of high temperature also gives rise to concern with this design. SiC-LAS is known to react chemically with some nickel-base alloys at elevated temperature levels (i.e., 800°C (1470°F) and above) reducing their ability to withstand oxidation. Locating the attachment in the hottest region of the segment also aggravates any complications associated with the differences in the thermal expansion of the two materials.

Concept 2 - Initial Film Cooled Liner Concept

Figure 7-3 shows the initial film cooled liner design concept in which the composite shingles are simple, single thickness cylindrical or conical sectors readily fabricated by current layup techniques. They are attached to the Hastelloy X shell by pins in the midlength region. Spacing between the shell and the shingle is maintained by direct contact at the upstream edge and a bushing or collar around the pin. Local clips at the pin locations provide some constraint of the upstream end of the panel to prevent blockage of the coolant film passage should the panel begin to curl. The shingle attachment pin is shown as being retained by a spring clip which accommodates some relative radial motion between shingle and shell. Alternatively, a more rigid attachment could be achieved by using the bolt and nut attachment as in Concept 1. Cooling air is admitted radially inward so as to impinge radially on the lip of

the louver and provide the desired high local heat transfer rate on this surface after which it can be discharged to form the desired film on the hot surface of the downstream panel. While the design would appear to meet the intent of the requirements derived from the preliminary aerothermal analysis, there are several limitations on its suitability. The retention clips block the cooling air flow immediately downstream of the attachment pin and would locally inhibit the cooling of the lip of the upstream panel as well as the formation of a strong film on the downstream panel at these circumferential positions. In addition, the rather long cantilevered length of the segment could lead to large deflections of the downstream end that would change the height of the coolant film initiation slot. Finally, while locating the attachment pins in the midlength region of the panel does reduce the temperature to which they are exposed relative to their being located at the downstream end of the segment as in Concept 1, they are still vulnerable to the same problems only to a lesser degree. An attractive feature of this concept is that individual segments of the liner may be removed for repair or replacement without having to disassemble other parts of the liner as would be required with Concept 1.

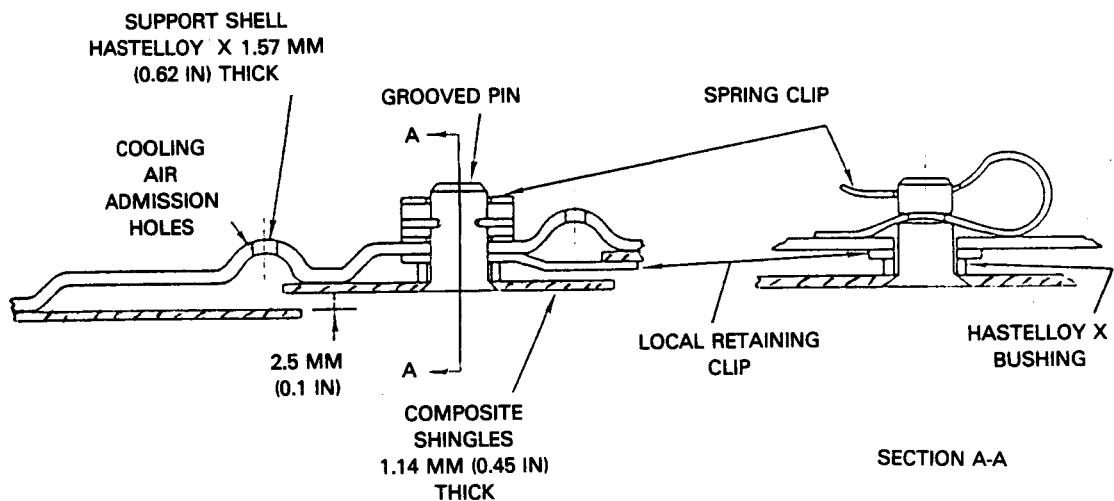


Figure 7-3 Composite Liner Design Concept 2

Concept 3 - Integral Attachment Liner Concept

This design concept is shown on Figure 7-4 and also incorporates multiple circumferentially separated shingle sectors. However, rather than being retained to the Hastelloy X shell by pins or bolts, the attachment is built into the shingle in the form of T-shaped ribs that fit into axial slots in the shell. With reference to Figure 7-4, the shell is stepped and the shingles are slid into place from the downstream direction after which a Hastelloy X strip is tack welded over the downstream end of the slot to retain the shingle. The major advantage of this concept is the elimination of all interference with the admission of cooling air to the liner. The radial jets of cooling air are allowed to impinge on the downstream lip of the shingle and discharge in a well defined film over the downstream panel, in the manner advocated in Section 7.1, without any circumferentially spaced interruptions for attachment pins, clips or the like.

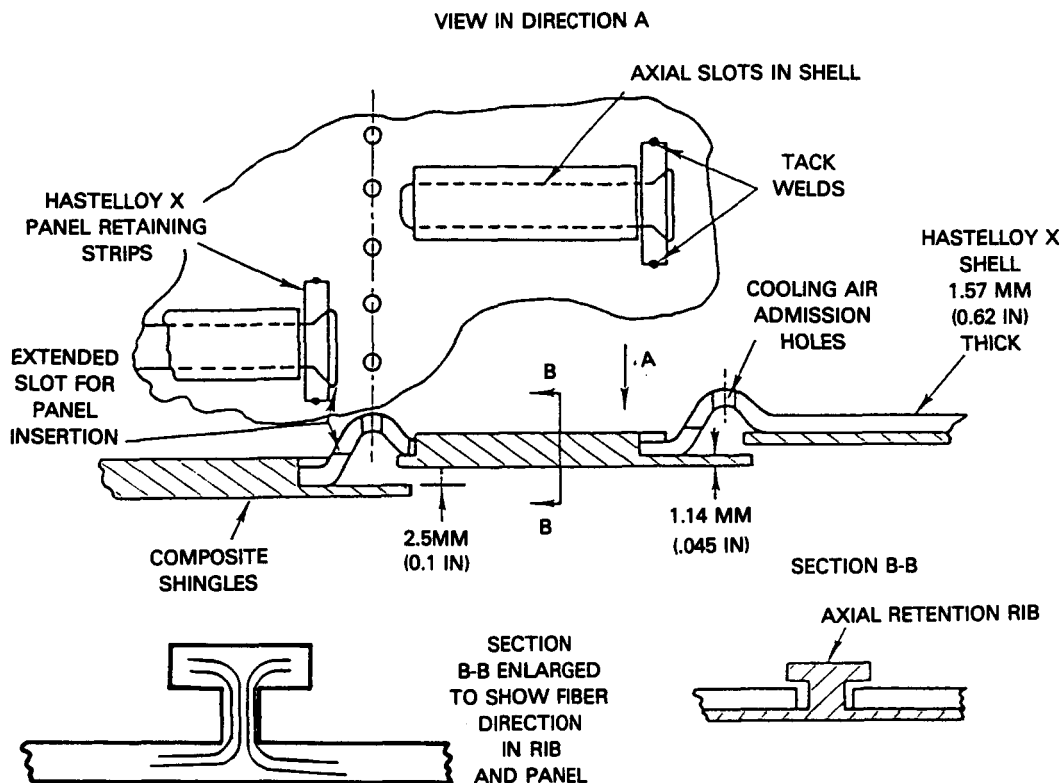


Figure 7-4 Composite Liner Design Concept 3

The major difficulty with this concept would be in the fabrication of the composite segments. To carry the attachment forces into the T-shaped ribs, complex fiber layups like those sketched in the auxiliary Section B-B of Figure 7-4 would be required. Stress concentrations would also be high in the vicinity of the ribs and the ribs themselves would be subjected to high radial thermal gradients because the base of the T would be exposed to the combustor internal heat load while the top would be surrounded by the cool air in the shroud surrounding the combustor. Temperature differences of as much as 555°C (1000°F) could readily be envisioned across the radial height of the rib. In addition, because of the attachment configuration the replacement of a damaged panel would necessitate removal of all downstream panels during repair of the liner. The application of this design concept to noncylindrical liners was also considered questionable. In summary, while it was ideal from the thermal design viewpoint, the complexities of the attachment of the segment to the shell precluded further consideration of Concept 3.

Concept 4 - Revised Film Cooled Design Concept

Concept 4, shown on Figure 7-5, was evolved to define an improved version of the basic film cooled, pin attached composite shingle liner construction of Concept 2. This configuration retains the simple, single thickness composite panel shape of that concept so as to be readily fabricable with current techniques. To alleviate concern over the temperature levels and differentials in the attachment region the pin has been relocated in the cool region under the louver lip. While this sheltered the attachment from high temperatures, it

also precluded removal of a single shingle without first removing the shingle upstream. This was circumvented by cutting axial slots in the Hastelloy X shell. The slot is covered with a small plate that is retained by a tab and the shingle attachment bolt. When the nut is loosened on the bolt, the entire bolt, cover and shingle assembly may be slid aft for removal. Locating the attachment directly under the louver lip precluded the use of impingement cooling of the lip in the immediate circumferential proximity of the attachment. However, the cooling air admission scheme shown allows for a long louver cavity in which a circumferentially uniform cooling film can be generated. Hence, while this design does not allow for impingement cooling of the louver lip, it will assure high film cooling effectiveness of the downstream panel. Circumferential variation of the cooling effectiveness is expected to be minimal with the domed head on the attachment bolt being the only obstruction in the film entry passage. While the cantilevered length of the downstream end of the segment could lead to deflections that alter the height of the coolant film initiation slot, it is not as long as in Concept 2 and the heads of the attachment bolts would tend to act as stops if the lip deflection became severe.

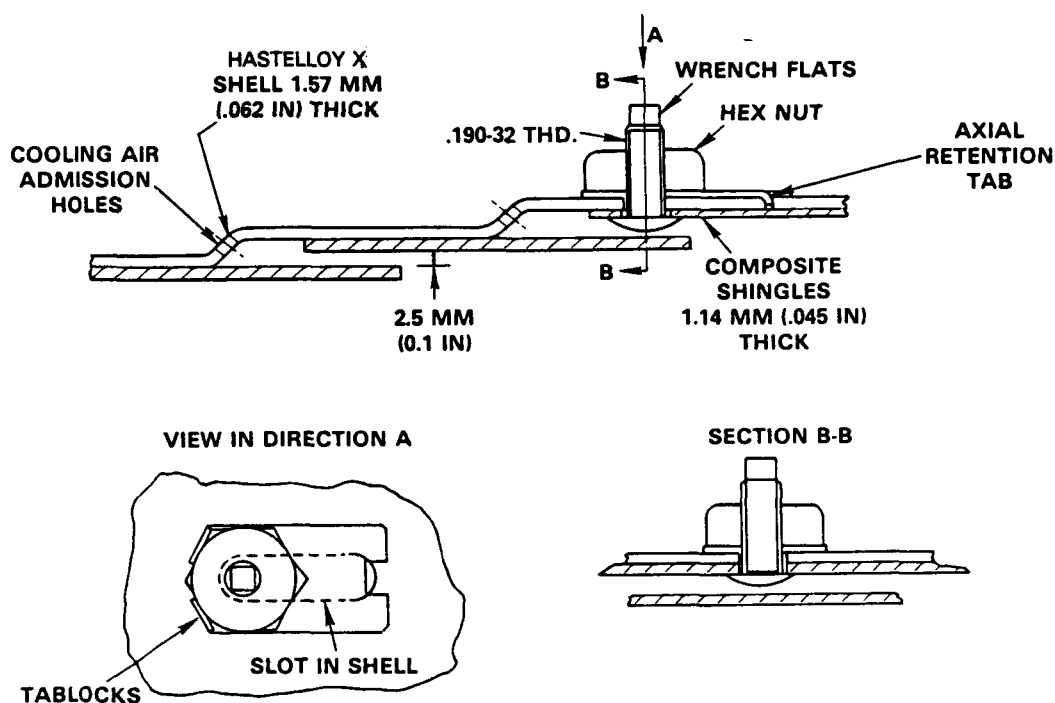


Figure 7-5 Composite Liner Design Concept 4

At the conclusion of the screening process it became evident that the conceptual definition of the configuration of the composite combustor liner had been one of evolution as opposed to the screening of independent design concepts. Concept 2 had evolved from the need to go beyond mere material substitution with a more readily fabricable composite segment that attempted to incorporate the cooling design philosophy of Section 7.1. After an excursion to Concept 3, which was ideal from the aerothermal point of view but required extremely complex attachment to the shell, the evolutionary process concentrated on refinement of the simpler Concept 2. This led to Concept 4 which eliminated many of the shortcomings of Concept 2 and offers the greatest potential for meeting the program objectives. It will be the configuration of the composite combustor liner that will be analyzed in detail in the remainder of this section.

7.3 Thermal Analysis of Composite Liner

The analysis of the SiC-LAS composite combustor liner was initiated with a detailed thermal analysis of the composite panel and Hastelloy X shell to define the internal temperature distribution for the structural analysis. A finite element computer program was used to calculate the temperature distribution in planar sections representative of axial cuts through a segment and the adjacent shell. As in the analysis of the reference metallic segment liner in Section 4.2, the combustion gas and cooling air temperatures were those of the reference advanced PW2037 engine at the takeoff operating condition which would produce the highest component temperatures encountered during a typical flight cycle. The thermal boundary connectors or heat transfer coefficients were established for a panel of the liner enclosing the primary combustion zone of the reference MARK IV combustor with an overall cooling air flow rate equal to that of the reference metallic liner defined in Section 4.2.

Figure 7-6 shows the results of the thermal analysis in terms of the temperature distribution in the liner assembly. The distribution is shown at three different circumferential positions including that at the center of a high temperature streak of combustion gases presumably caused by fuel rich combustion, at the edge of such a streak where the gas temperature is more moderate, and between streaks where it is "average". The results indicate that the maximum hot side surface temperature of the composite panel and the maximum through thickness temperature gradient occur under the hot gas streak at the downstream lip of the panel. The 1261°C (2303°F) maximum temperature and the 258°C (465°F) through thickness temperature difference at this position are both consistent with expectations based on the preliminary thermal analysis of Section 7.1. The results also indicate that the entire surface of the composite panel exposed to the combustion gases is hot. While the cooling effectiveness of the film is higher immediately downstream of the louver (for example, at the location having a surface temperature of 1226°C at the center of the hot gas streak on Figure 7-6), the heat rejection from the cold side of the panel is limited to radiation to the shell at this axial position. Conversely, further downstream cold side heat rejection is enhanced by the convective effect of the cooling air flow entering the louver and offsets the deterioration in cooling effectiveness of the louver film. As a result, the greatest difference in the temperature of the part of the hot side of the composite segment

that is exposed to the hot gases is less than 167°C (300°F). There is also an inflection in the axial temperature distribution in the composite panel because the heat rejection from the cold side of the panel is higher in the central area where the cooling air jets admitted through the shell impinge on the panel than it is further downstream. These variations in the axial temperature distribution in the panel and, in particular, the localized effect of the impingement of the cooling air on the cold side of the panel are more evident in the graphical presentation of these data in Figure 7-7.

The temperature variations in the Hastelloy X shell are minimal except for a band of 83°C to 111°C (150°F to 200°F) higher temperature upstream of the step. This is due to the radiant heat transfer from the hot composite panel in this area. Radial temperature differences through the Hastelloy X shell were computed to be very small, of the order of 1°C (2°F).

In situations where the time of exposure to elevated temperatures is critical to component life, the temperature levels at the cruise flight condition can be significant. The thermal analysis was repeated using gas and cooling air temperatures and other boundary conditions consistent with cruise operation of the advanced PW2037 engine. Figure 7-8 shows the resultant temperature distribution in the liner in the center of a hot gas streak region and indicates that the maximum liner temperature is 967°C (1775°F) at the start of cruise.

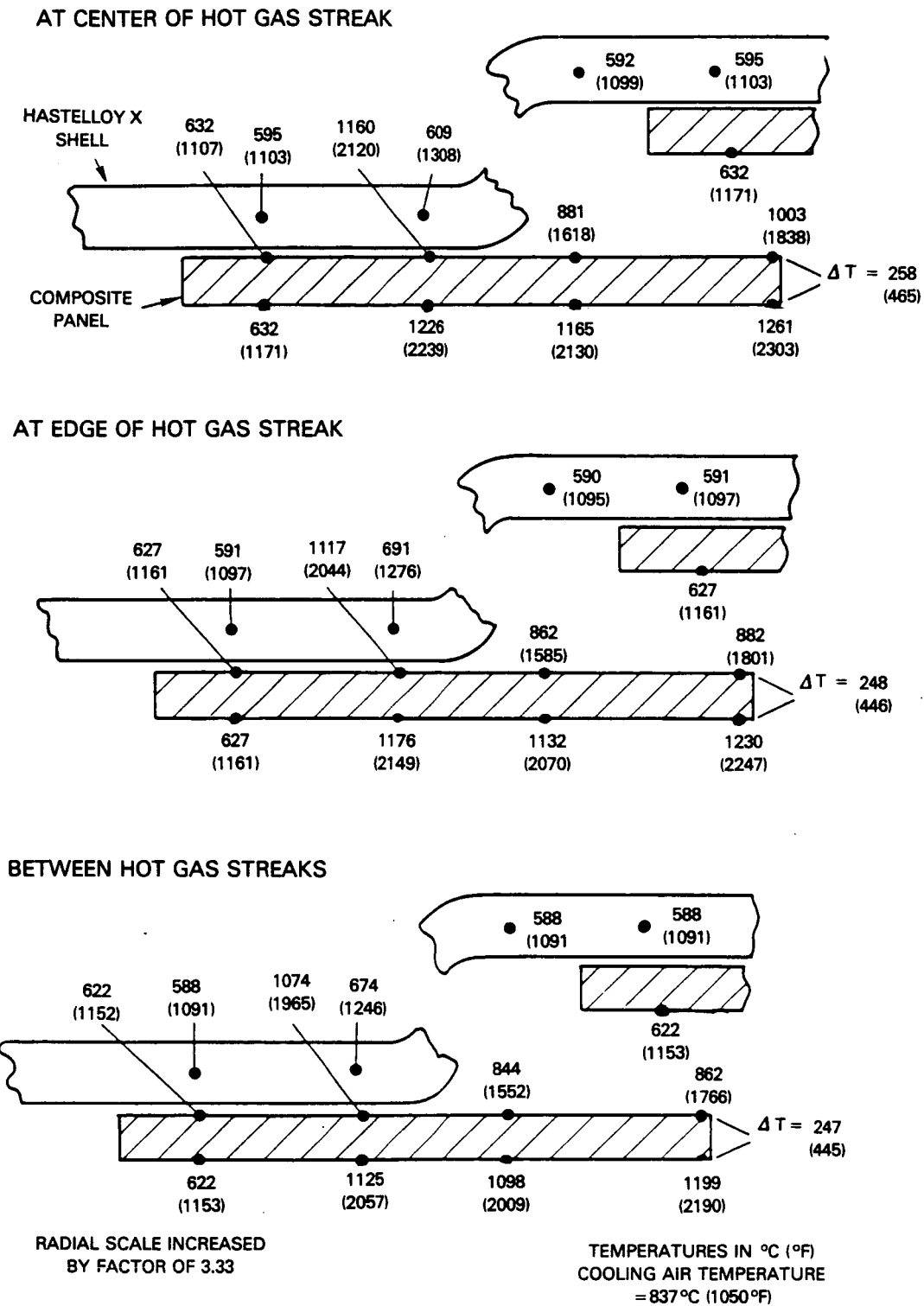


Figure 7-6 Temperature Distribution in Composite Combustor Liner at Takeoff Condition

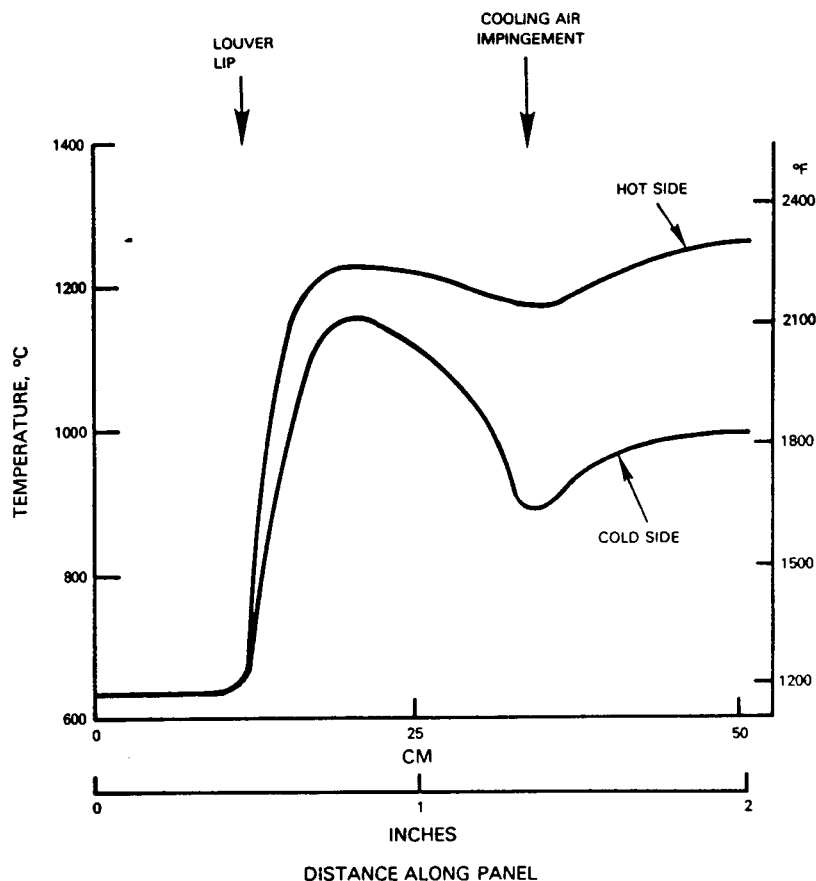


Figure 7-7 Axial Temperature Distribution in Composite Panel at Hot Streak Location During Takeoff Operation

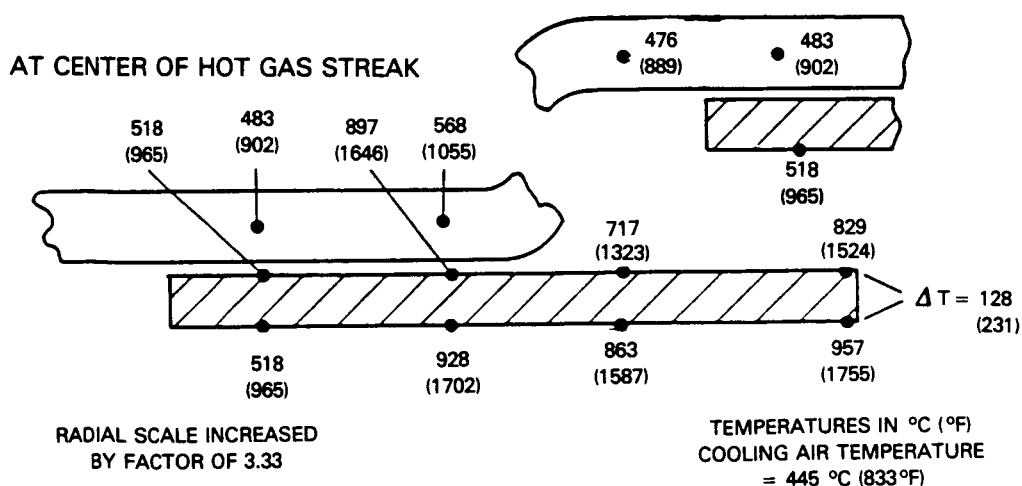


Figure 7-8 Temperature Distribution in Composite Combustor Liner at Cruise Condition

7.4 Structural Model of the Composite Liner

From the microscopic point of view, the composite material consists of multiple fibers immersed in the ceramic matrix. The structural properties of the material are dependent on the strengths of each component and involve extremely complex interaction and interfacial mechanisms that defy analytical modeling. On the macroscopic level, the composite can be envisioned as multiple layers of material having anisotropic property variations consistent with the direction of fiber orientation in that layer. While structural models of composite materials have been formulated on the basis of this laminar approach, their applicability is limited to the simplest of configurations and they would be incapable of analyzing the complex mechanical and thermal loading on the combustor liner. Consequently, the structural analysis of the composite combustor liner has been based on a more global constitutive model in which bulk mechanical properties were employed but the anisotropic nature of the composite material was also recognized.

The NASTRAN (Reference 6) computer program was used for the structural analysis of the composite liner, and an operating mode was selected that considered the composite liner shingle to be a single element thick but recognized gradients in stress, strain and temperature across this thickness. Figure 7-9 shows the finite element breakup that was used for this elastic stress analysis. The individual composite shingles were assumed to be 30 degrees in circumferential width which was identical to that of the segments of the reference metallic liner. The panels are symmetrical and the domain of the structural analysis consisted of one-half the panel width. Each half panel experiences a streak of elevated gas temperature associated with the 15 degree spacing of the air admission modules in the combustor. The panel is attached to a 1.14 mm (0.045 in) thick Hastelloy X shell which was also modeled over the same domain.

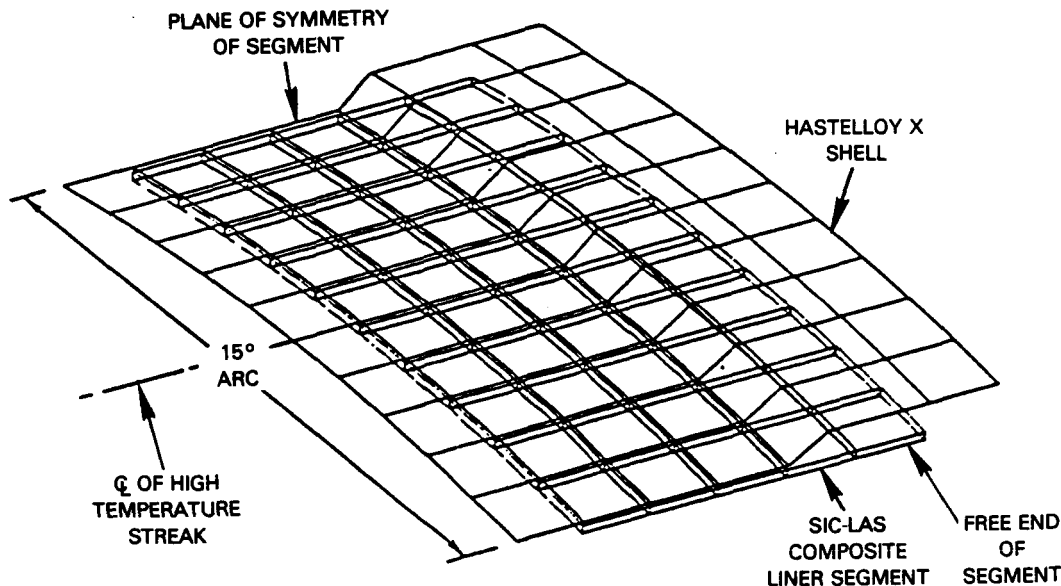


Figure 7-9 Structural Model of SiC-LAS Composite Liner

The SiC-LAS composite segment was modeled using a six-sided isoparametric element (Hexa) in the NASTRAN program. It is a twenty-noded element with eight corner nodes and twelve edge nodes. The Hexa element allows through thickness and in-plane temperature, stress and strain variation, as well as the use of temperature dependent anisotropic material properties. The Hastelloy X support shell is not subjected to the through thickness thermal gradients experienced by the composite panels and consequently was modeled with the simpler quadrilateral flat shell elements (QUAD4). This is a four-noded element with five degrees of freedom per node which include three displacements and two rotations. The 15 degree arc was modeled with boundary conditions to simulate a full hoop construction.

To describe the distribution of temperature and stress state in the plane of the panel, a total of fifty solid elements were used to model the panel and another seventy plate elements were used to describe the shell. The complete finite element breakup is shown in Figure 7-9.

As shown in Figure 7-5, the SiC-LAS composite segments are attached to the shell with Hastelloy X bolts that were modeled using beam elements in the NASTRAN code. These are linear elements whose properties and behavioral variables are continuously distributed along a segment that joins two grid points and can provide resistance to all six degrees of freedom at a geometric grid point. The panels were connected to the shell in the radial direction but could move relative to the shell in the axial and circumferential direction to simulate clearance in the bolt hole. Modeling of this attachment was achieved by using the multipoint constraint option in NASTRAN. A multipoint constraint is a linear equation that relates the displacement degrees of freedom. The use of this option made it possible to analyze extreme cases of segment to shell attachment constraints.

In formulating a constitutive model for the SiC-LAS composite material in the NASTRAN program, it was recognized that the $0^\circ/+45^\circ/-45^\circ/90^\circ$ sequence of layup of the fiber layers would produce a material that would have little variation in mechanical properties in the plane of the layers but would have entirely different laminar characteristic properties in the radial or through thickness direction. This led to the use of a transversely isotropic material definition in which the stress-strain relation assumes the form:

$$\begin{Bmatrix} \sigma_1 \\ \sigma_2 \\ \sigma_3 \\ \tau_{23} \\ \tau_{31} \\ \tau_{12} \end{Bmatrix} = \begin{bmatrix} C_{11} & C_{12} & C_{13} & 0 & 0 & 0 \\ C_{12} & C_{11} & C_{13} & 0 & 0 & 0 \\ C_{13} & C_{13} & C_{33} & 0 & 0 & 0 \\ 0 & 0 & 0 & C_{44} & 0 & 0 \\ 0 & 0 & 0 & 0 & C_{44} & 0 \\ 0 & 0 & 0 & 0 & 0 & (C_{11} - C_{12})/2 \end{bmatrix} \begin{Bmatrix} \epsilon_1 \\ \epsilon_2 \\ \epsilon_3 \\ \gamma_{23} \\ \gamma_{31} \\ \gamma_{12} \end{Bmatrix} \quad (7-1)$$

where the 1 and 2 directions are in the plane of the fibers and 3 is orthogonal to that plane and the coefficients are:

$$C_{11} = \frac{1 - \nu_{23}\nu_{32}}{E_2 E_3 \Delta}$$

$$C_{22} = \frac{1 - \nu_{13}\nu_{31}}{E_1 E_3 \Delta}$$

$$C_{12} = \frac{\nu_{21} + \nu_{31}\nu_{23}}{E_2 E_3 \Delta} = \frac{\nu_{12} + \nu_{32}\nu_{13}}{E_1 E_3 \Delta}$$

$$C_{23} = \frac{\nu_{32} + \nu_{12}\nu_{31}}{E_1 E_3 \Delta} = \frac{\nu_{23} + \nu_{21}\nu_{13}}{E_1 E_2 \Delta}$$

$$C_{13} = \frac{\nu_{31} + \nu_{21}\nu_{32}}{E_2 E_3 \Delta} = \frac{\nu_{13} + \nu_{12}\nu_{23}}{E_1 E_2 \Delta}$$

$$C_{33} = \frac{1 - \nu_{12}\nu_{21}}{E_1 E_2 \Delta}$$

$$C_{44} = G_{23}$$

$$C_{55} = G_{31}$$

where

$$\Delta = \frac{1 - \nu_{12}\nu_{21} - \nu_{23}\nu_{32} - \nu_{31}\nu_{13} - 2\nu_{21}\nu_{32}\nu_{13}}{E_1 E_2 E_3}$$

Definition of the material properties, i.e., the moduli and Poisson's ratios, in this system of equations required some approximations and the use of related experimental data from Section 6.0. The elastic modulus E_1 of the $0^\circ/+45^\circ/-45^\circ/90^\circ$ composite was measured in the flexure tests described in Section 6.2, and a mean value of 71.6 GPa (10.4 Msi) at room temperature was selected. By symmetry of the transversely isotropic material E_2 was defined equal to E_1 . The elastic modulus E_3 in the through thickness direction perpendicular to the plane of the fibers was assumed to be equal to that measured transverse to the fibers in a unidirectional SiC-LAS composite (Reference 7). In both cases the properties of the matrix would dominate the elastic characteristics of the material. Pursuing the same rationale, the shear moduli in the planes normal to that of the fibers, G_{13} and G_{23} , were assumed equal to the transverse shear modulus of the unidirectional SiC-LAS composite. Thereafter, the values of Poisson's ratios $\nu_{13} = \nu_{31}$ and $\nu_{23} = \nu_{32}$ were evaluated from the relationship:

$$\nu_{ij} = \sqrt{\frac{E_i E_j}{2G_{ij}}} - 1 \quad (7-2)$$

Finally, the Poisson's ratio in the plane of the fibers, $\nu_{12} = \nu_{21}$ was estimated as being the volume weighted average of that of the matrix and the fibers, and the in-plane shear modulus G_{12} was determined from Equation 7-2 on the basis of this estimate.

In summary, the following material property values were determined at room temperature:

$$\begin{aligned} E_1 &= E_2 = 71.6 \text{ GPa (10.4 Msi)} \\ E_3 &= 46.9 \text{ GPa (6.8 Msi)} \\ G_{12} &= 21.4 \text{ GPa (3.1 Msi)} \\ G_{13} &= G_{23} = 22.1 \text{ GPa (3.2 Msi)} \\ \nu_{12} &= \nu_{21} = 0.48 \\ \nu_{13} &= \nu_{31} = \nu_{23} = \nu_{32} = 0.30 \end{aligned}$$

Temperature dependence of the elastic and shear moduli were assumed in the structural analysis of the composite liner. Figure 6-5 shows the measured variation of the elastic modulus E_1 or E_2 of the $0^\circ/+45^\circ/-45^\circ/90^\circ$ SiC-LAS composite and indicates that the modulus remained constant from room temperature through 871°C (1600°F) after which it began to decline. In modeling the temperature dependence of the moduli E_1 and E_2 , the arguments at the conclusion of Section 7.1 regarding the rate of development in the field of ceramic composites were recognized and the material was assumed to be improved somewhat from the current SiC-LAS used to generate the data of Figure 6-5. In particular, while the decline in the elastic modulus was assumed to start at the 871°C (1600°F) threshold of that figure, the rate of decline was reduced to be consistent with the projected 1254°C (2300°F) useful temperature of the material. This was accomplished by assuming that the 45 GPa (6.5 Msi) nominal level of the elastic moduli measured at 1038°C (1900°F) with the current SiC-LAS composite would be achieved at a temperature of 1200°C (2200°F) with near term improvement of this basic material. The temperature dependence of the other moduli, i.e., E_3 and the shear moduli, were assumed to follow parallel trends of declining proportionately from the above listed room temperature values at temperatures above 871°C (1600°F).

7.5 Dynamic Structural Analysis

A dynamic analysis was conducted to investigate the panel mode vibrations of the composite segments. The objectives of this analysis were twofold: the first was to optimize the number and locations of the segment to shell attachments. The second objective was to assure that the segments would not be excited to vibrate during engine operation. This would be accomplished if their natural frequency was well above the 220 Hz maximum rotation speed of the PW2037 engine high rotor. After completion of this dynamic analysis, the more complex static structural analysis could be conducted with the appropriate number of attachments between the segment and the shell.

The NASTRAN computer program was also used for the modal analysis. To reduce the complexity of the computational procedures a simpler QUAD4 plate element was used rather than the solid elements of the structural model described in Section 7.4. (The solid element model was used for the static structural analysis that will be discussed in Section 7.6.) While the solid element approach allowed transversely isotropic material modeling with different material properties in the through thickness direction, use of the plate element model requires the assumption of isotropicity in all directions. To assess the impact of this simplification on the dynamic analysis an independent investigation was conducted in which a beam in three point flexure was analyzed using

the six-sided solid elements on NASTRAN. The results indicated that the compliance of the SiC-LAS material modeled as a completely isotropic material was 75 percent of that computed with the transversely isotropic properties of Section 7.4. Since the natural frequency varies inversely with the square root of the compliance, the assumption of material isotropicity needed to use the simpler plate element model leads to overprediction of the natural frequency of the panel by about 12 percent. No attempt was made to correct the subsequent analysis for this factor and it must be recognized in establishing margins based on the computed natural frequency.

While only a half segment was modeled for the static analysis, one entire 30-degree, transverse width segment was modeled for this analysis in order to include all possible vibration modes. The panel was also assumed to be rigidly attached to the shell in the radial direction at the attachment points.

The initial dynamic analysis was conducted on a segment that was very rigidly attached to the shell having ten circumferentially spaced attachments. The analysis predicted a fundamental natural frequency of 813 Hz for this configuration which satisfied the segment vibration design criteria of being greater than 220 Hz by a wide margin. This frequency is also nearly twice the natural frequency of the baseline metallic segment defined in Section 4.0 partially because of the lower density of the composite material. As shown on Figure 7-10, the vibratory mode consisted of flapping of the downstream corners of the segment.

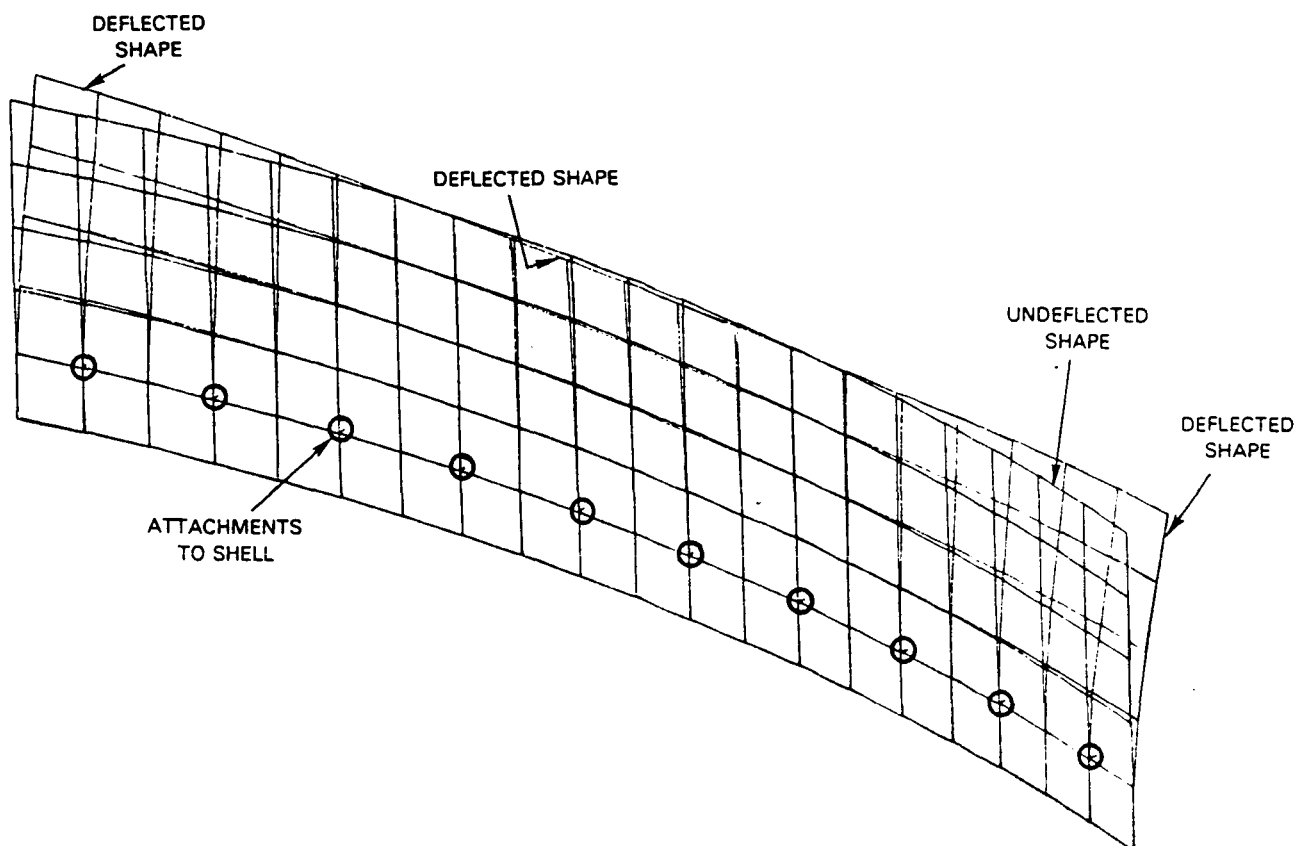


Figure 7-10 Mode Shape for Natural Vibration of Composite Liner Segment Rigidly Attached to Shell

The analysis was continued with the evaluation of two configurations incorporating six rather than ten attachments to the shell. As shown on Figure 7-11, one of these featured attachments at relatively evenly spaced transverse positions, while the second had the attachments paired to provide some redundancy at the ends of the segment. The dynamic analysis indicated that the removal of four attachments did not have a significant effect on panel mode vibration with the natural frequencies of both six attachment schemes remaining well in excess of 700 Hz.

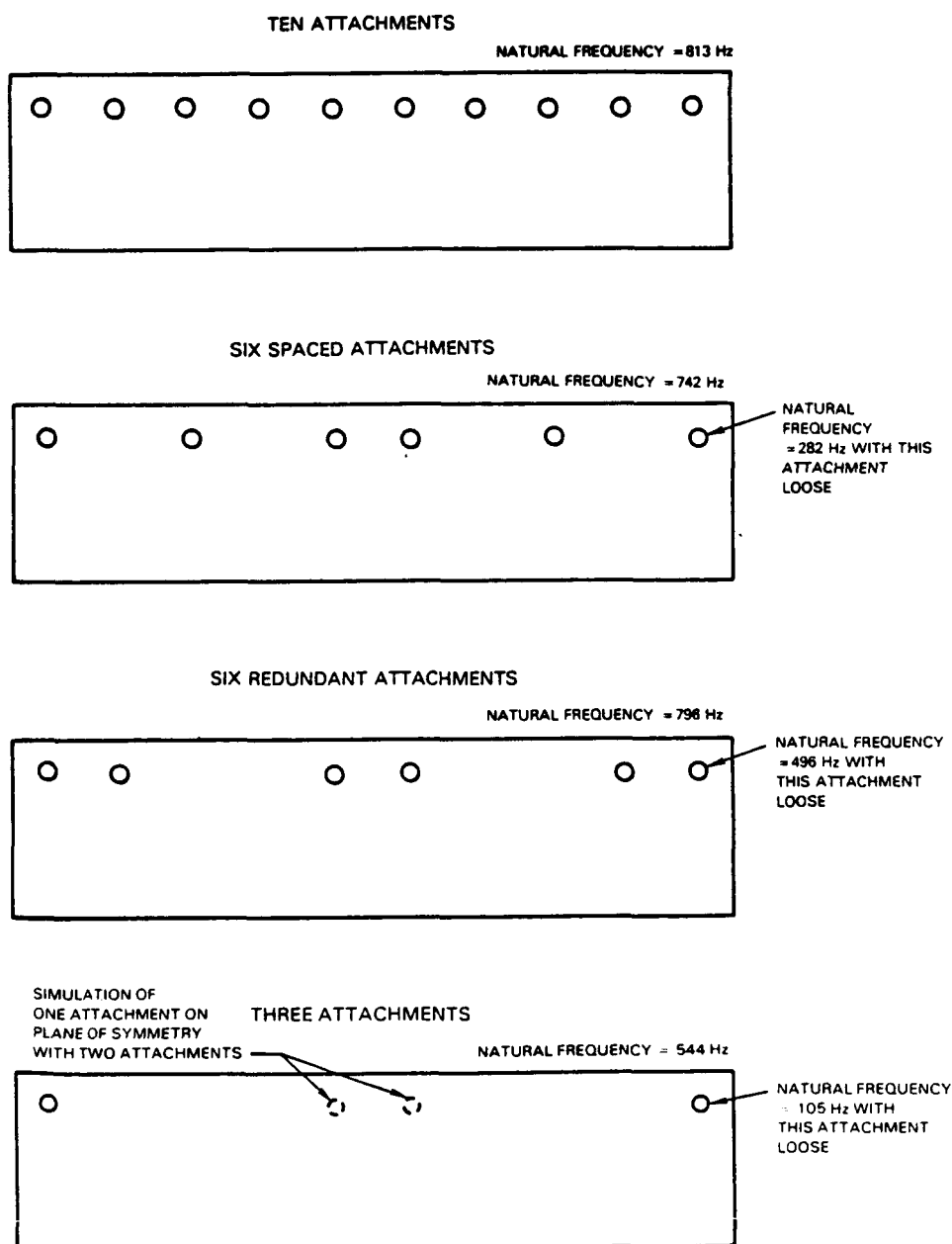


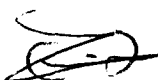
Figure 7-11 Effect of Attachments on Natural Frequency of Composite Liner Panel

Carrying the analysis a step further, both of the six attachment configurations were evaluated for the situation in which the attachment nearest one end was loose or broken so as to permit unrestrained radial motion. This resulted in significant reductions in the natural frequency of the segment in both configurations. The configuration with paired attachments near the ends of the segment has an obvious advantage because of the redundancy of this scheme which maintains an adequate natural frequency margin by a factor of more than two relative to the criteria of a natural frequency in excess of 220 Hz. Failure of the end attachment on a segment with spaced attachments is shown to lead to a much larger decline in natural frequency of the segment to a level that approaches that of the maximum high rotor speed.

On the basis of this analysis it appeared that the number of attachments of the segment to the shell could be reduced significantly without compromising the dynamic properties of the segment. The apparent desire for redundancy of attachment at the ends of the segment may be offset by confidence in the integrity of the attachment as experience is accumulated with actual hardware. To that end, the analysis was extended to a configuration having only three attachments. (To maintain compatibility conditions at the plane of symmetry, this configuration was modeled as having two closely spaced attachments in the center rather than one on the centerline.) The results of the analysis indicated that the fundamental natural frequency of the panel at 544 Hz was still about 10 percent higher than that of the metallic segment with a comparable number of attachments. When one of the attachments at the end of the panel was eliminated to simulate loosening or failure, the natural frequency dropped to 105 Hz. Figure 7-12 shows the mode shape for vibration of the panel with the attachments intact and with one at the end loose. With the loose attachment the natural frequency of the three attachment configuration is below the criteria of 220 Hz minimum to avoid excitation by the high rotor. However, a similar decline in natural frequency would occur if an attachment were to fail on the metallic segment. Redundancy of attachments to maintain margin from rotor induced vibration in the event of an attachment failure had not been a criteria in the design of the baseline metallic liner in Section 4.0, and there is no reason to expect the composite liner attachments to have less integrity. In fact, being located in a cool region, the attachments of the composite liner segments are probably considerably less vulnerable. Consequently, attachment redundancy was not a consideration in the final definition of the composite liner configuration and three attachments per segment were selected for the remainder of the structural analysis.

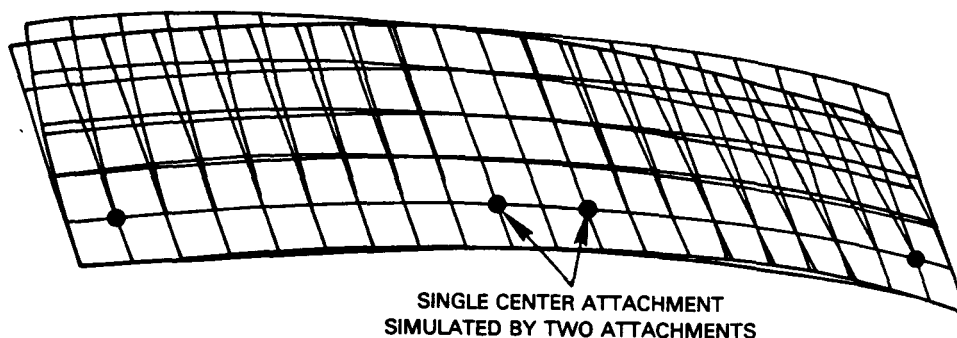
7.6 Static Structural Analysis

The static structural analysis of the composite liner was conducted on the NASTRAN program using the solid element structural model with the transversely isotropic constitutive definition of the SiC-LAS material as described in Section 7.4. Based on the results of the dynamic analysis the segment was assumed to be connected to the shell by three attachments but, as in that analysis, the attachment at the plane of symmetry of the panel could not be readily modeled and was simulated with an attachment either side of that plane. The connections at the attachment allowed complete freedom of relative motion between



the shell and the panel in the transverse and axial direction while maintaining a radial constraint. The analysis was conducted at conditions representative of takeoff operation of the reference PW2037 engine with the temperature distribution in the panel and shell being described by the data of Figure 7-6. The mechanical loads on the panel and shell consisted of the forces generated by static pressure loadings. Consistent with the constraints of Section 3.3, the overall static-to-static pressure drop across the combustor liner was 2.5 percent of the combustor inlet total pressure or 0.069 MPa (10.0 psia) at the takeoff condition analyzed. On the shingle type of liner construction the shell carries this entire load. There are no pressure loads on the SiC-LAS panels other than the localized force produced by the impingement of the cooling air jets on the cold side. These loads were deduced to be about 60 percent of the above cited overall liner pressure drop and were imposed only on the elements of the panels opposite the cooling air admission holes in the shell.

ALL ATTACHMENTS INTACT
NATURAL FREQUENCY = 544 Hz



LOOSE ATTACHMENT AT END
NATURAL FREQUENCY = 105 Hz

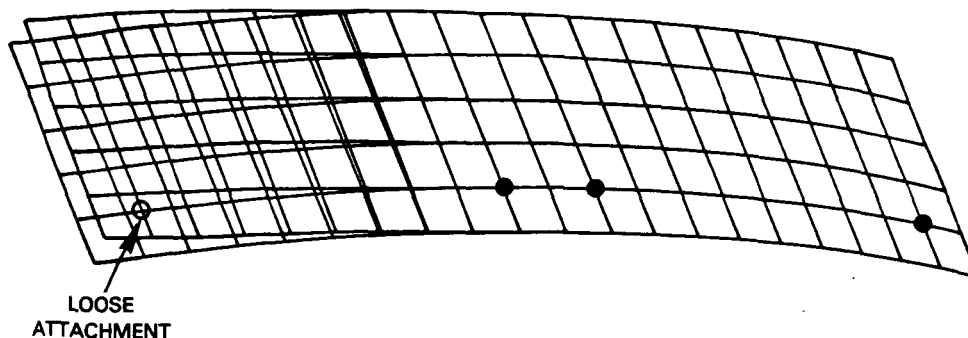
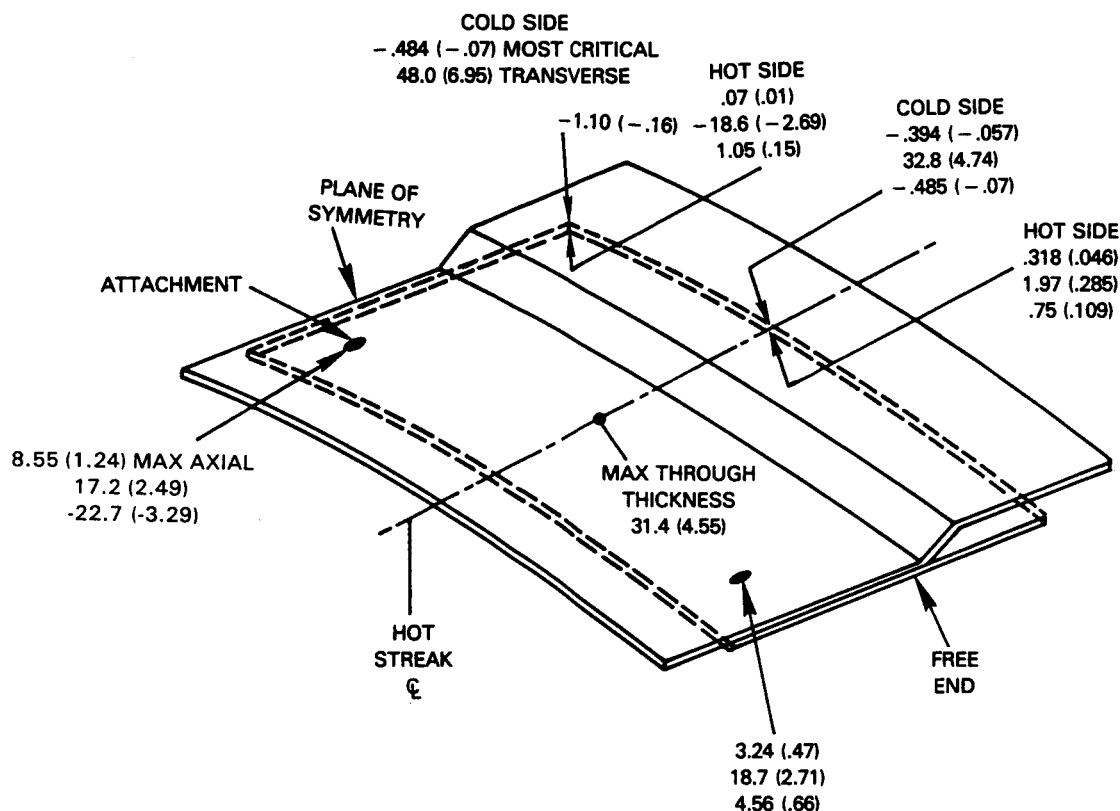


Figure 7-12 Mode Shapes for Vibration of Panel With Final Three-Point Attachment Configuration

Figure 7-13 shows the highlights of the results of the structural analysis with the magnitude of the three components of stress in the cylindrical coordinate system being shown at selected critical locations in the panel including those where each is a maximum or most critical. The results show that the stress levels in the panel are low, and since the panel grows relatively independent of the shell, they are primarily due to local temperature gradients and not mechanical loads.



STRESS IN MPa (KSI) IN AXIAL, TRANSVERSE AND
THROUGH THICKNESS DIRECTIONS RESPECTIVELY

Figure 7-13 Highlights of Stress Distribution in the Composite Liner Panel

The transverse component of stress is dominant and Figure 7-14 shows the detailed distribution of this component in the hot and cold side surfaces of the panel. The stress magnitude is shown at the corner of each element of the breakup in the analysis. Over the downstream half of the length of the panel, i.e., that part with high convective cooling on the cold surface, the stresses are tensile in the cold surface and compressive in the hot side. This stress distribution is caused by the high through thickness temperature differential in this part of the segment. The difference between hot and cold side surface temperature is 247 to 284°C (445 to 512°F) and, while the coefficient of expansion of the composite material is low, it is constrained by the shell and opposing compressive and tensile stresses are generated at the hot and cold surfaces. The highest stress magnitudes in this part of the panel occur at the

plane of symmetry from which they decline toward zero at the free ends. There is little evidence of the hot gas temperature streaks in the stress distribution with the only perturbation being a limited region of reversed stress of very low magnitude, less than 6.9 MPa (1.0 ksi), on the hot side surface. The temperature gradient through the downstream end of the panel also causes the panel to deflect radially away from the hot gas side. The computed deflections are 0.33 mm (0.013 in) and 0.38 mm (0.015 in) at the plane of symmetry and free edge of the panel respectively. While significant relative to the 2.54 mm (0.10 in) height of the gap in which the cooling air film is generated, these deflections can be readily compensated for in defining the cold dimensions of the gap.

The transverse stress component map also indicates that the stresses in the upstream half of the composite panel may be defined in terms of two bands - one at the leading edge of the panel around the attachments that is dominated by tensile stresses in both surfaces and the other further downstream in which the stresses in both surfaces are predominately compressive. The through thickness temperature gradients are negligible in these regions and these stresses are due to axial temperature gradients in the material. As shown in Figure 7-7, the temperatures in the leading edge region of the panel were about 627°C (1160°F) whereas the temperatures further downstream (i.e., where the panel is exposed to the hot combustion gases but has minimal cooling of the cold surface) average around 1177°C (2150°F). The resultant thermal strain gives rise to the bands of compressive and tensile transverse stress in this area.

As shown on Figure 7-13, the magnitude of the axial component of stress in the panel was low with the maximum level being 8.55 MPa (1.24 ksi) at the "center" attachment location. Consequently, the magnitude of the maximum stresses in the plane of the fibers is essentially that of the transverse components. On this basis, the highest stress levels encountered are about 58 MPa (8.5 ksi) in tension and these are in the cooler region near the attachment. In the hot regions of the panel, the maximum stresses are lower being nominally 55 MPa (8 ksi) in compression and 48 MPa (7 ksi) in tension. Based on the flexure tests of the SiC-LAS material shown in Figure 6-4, stresses of this magnitude are only about half those of the proportionality limit of the material. Consequently from the point of view of the in-plane stresses, the validity of the use of the NASTRAN linear elastic analysis is established.

With reference to Figure 7-13, the radial stress components in the panel are higher near the attachments and almost nonexistent at the hot downstream lip. The radial stress is 22.7 MPa (3.29 ksi) in the compressive direction at the "center" attachment, while it is tensile and of considerably lower magnitude at the attachment near the free end. These stresses are caused by the changes in the radius of curvature of the segment and the shell. When both are heated to about the same temperature level, but with significantly different coefficients of expansion, radial loads develop in the attachments. This analysis was conducted for a composite segment on the inside surface of an outer liner shell. The loading would be reversed for a segment on the inner liner shell in that the center attachment would be loaded in tension and those at the free end in compression.

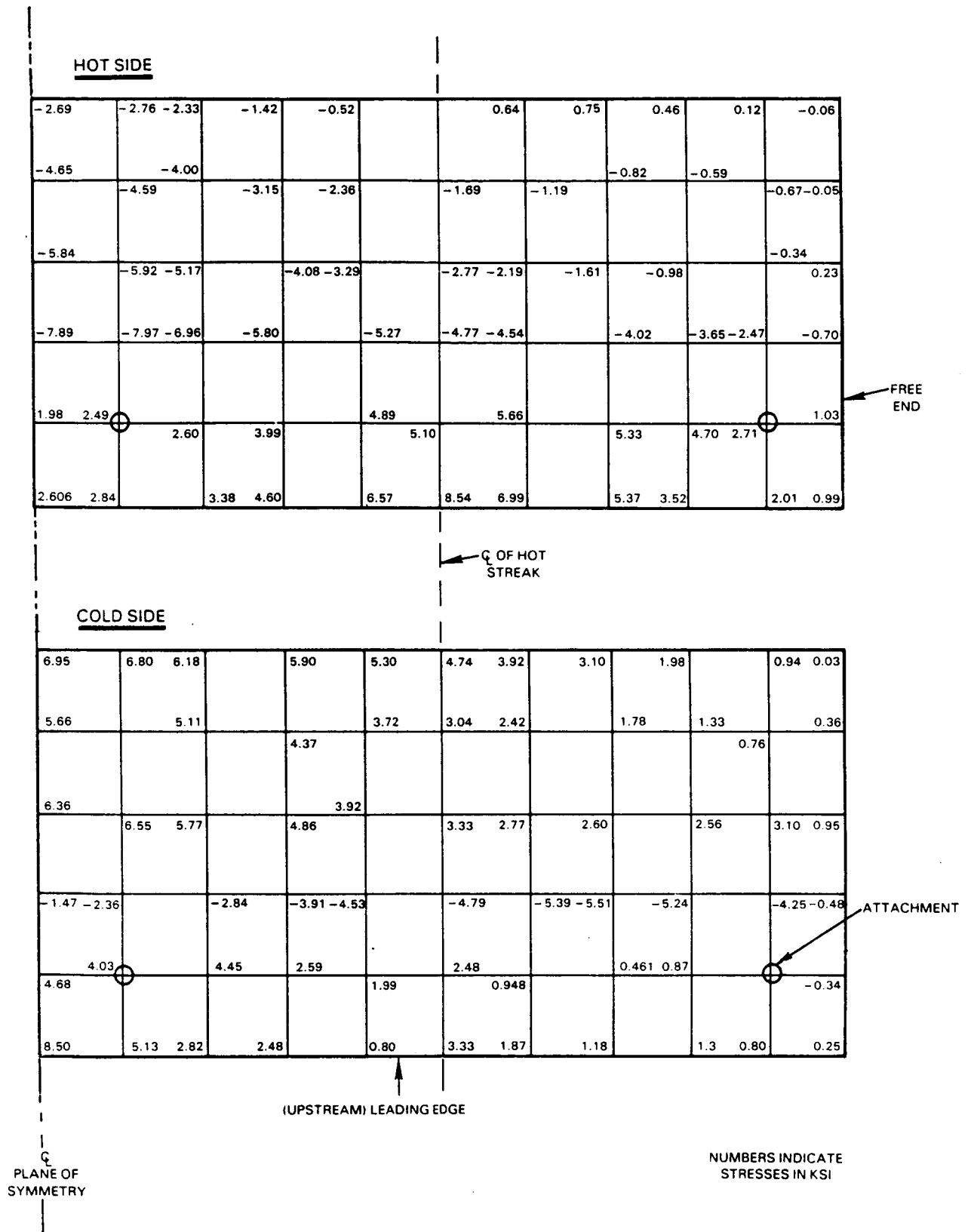


Figure 7-14 Distribution of Transverse Component of Stress in Surfaces of Composite Liner Segment

The maximum radial stress is shown on Figure 7-13 to occur on the centerline of the high gas temperature streak at an axial position near the center of the panel. Figure 7-15 shows the detailed distribution of the radial stress component along the plane of the high temperature streak and indicates that the magnitude of the stress diminishes rapidly both upstream and downstream of this maximum. Comparison with the temperature distribution in the panel at the hot streak plane in Figure 7-7 indicates that the maximum stress coincides with the juncture between a region of low through thickness temperature differential upstream of the cooling air injection point and one having high temperature gradients through the composite panel as a consequence of the convective cooling on the cold side surface. The high through thickness stresses occur in this region because the upstream part of the panel with high hot and cold side surface temperatures has a higher average temperature than the downstream region and is constrained from growing thicker by the downstream region.

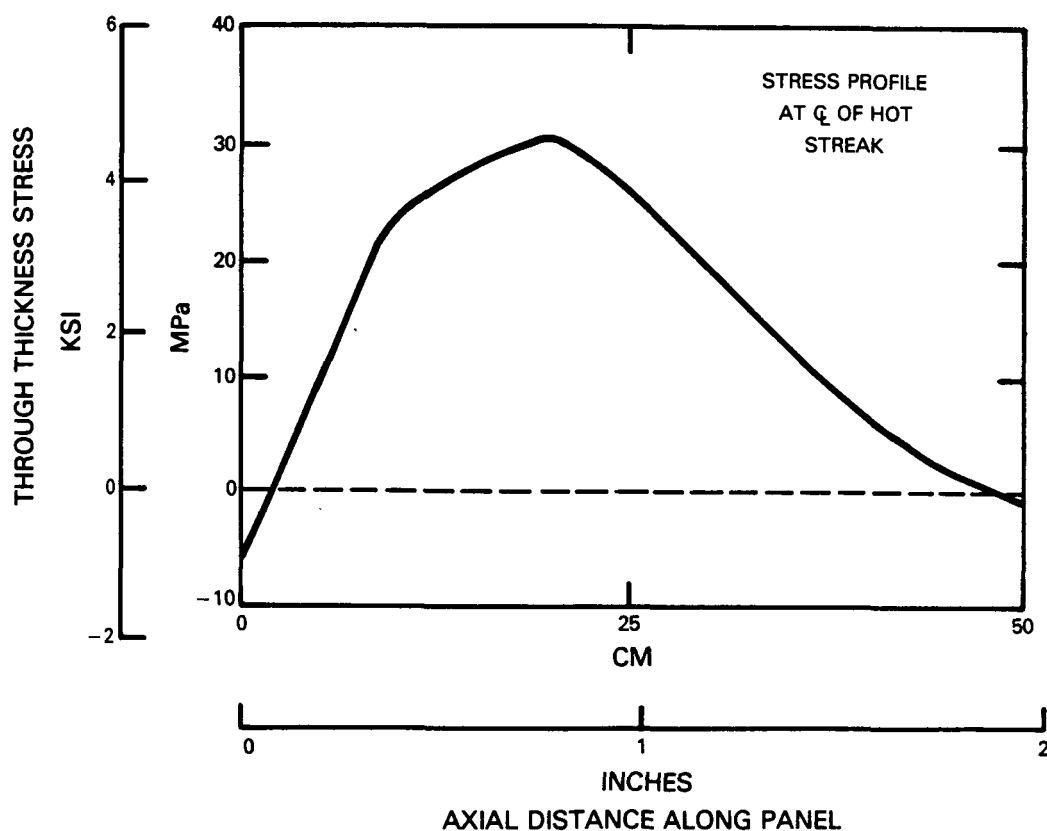


Figure 7-15 Distribution of Through Thickness or Radial Stress in Composite Panel

Figure 7-16 shows a graphic representation of the transverse stress components on the hot and cold side surfaces of the composite panel at the downstream end - the stress magnitudes having been deduced from the maps of that component in Figure 7-14. The data indicate that the opposition of stress direction over the central half of the panel gives rise to significant interlaminar shearing action over that region but that these stress differentials, and hence the shearing effect, diminish to zero at the free ends of the composite panel. With the structural analysis, of practical necessity, restricted to one element in the through thickness direction, the direct computation of shear stresses in this plane was impossible. Using beam theory and assuming that the transverse stresses in the surfaces of the panel in the vicinity of the plane of symmetry are analogous to those induced by four point flexure loading of the material; as in the test configuration of Section 6.2; the magnitude of the interlayer shear stress was estimated. The bending stress on the section was computed by this approach to be 34.5 MPa (5.0 ksi) and the corresponding shear stress across the layers of the composite 0.97 MPa (0.14 ksi). For comparative purposes, a similar analysis was made of the stresses in Specimen 2350-7 of the flexure tests of Section 6.2. When loaded to the yield point at a temperature of 1038°C (1900°F) in four point flexure, the corresponding stresses were 90 MPa (13.0 ksi) in bending and 1.94 MPa (0.28 ksi) in shear which is more than twice the magnitudes computed in the downstream end of the liner panel. Since all of the flexure test specimens evaluated at high temperatures ultimately failed in tension at loads well in excess of that producing yield and with no visible evidence of interlaminar shear distress, it appears that the shear stress levels computed in the liner panel are moderate and should not compromise the integrity of the panel.

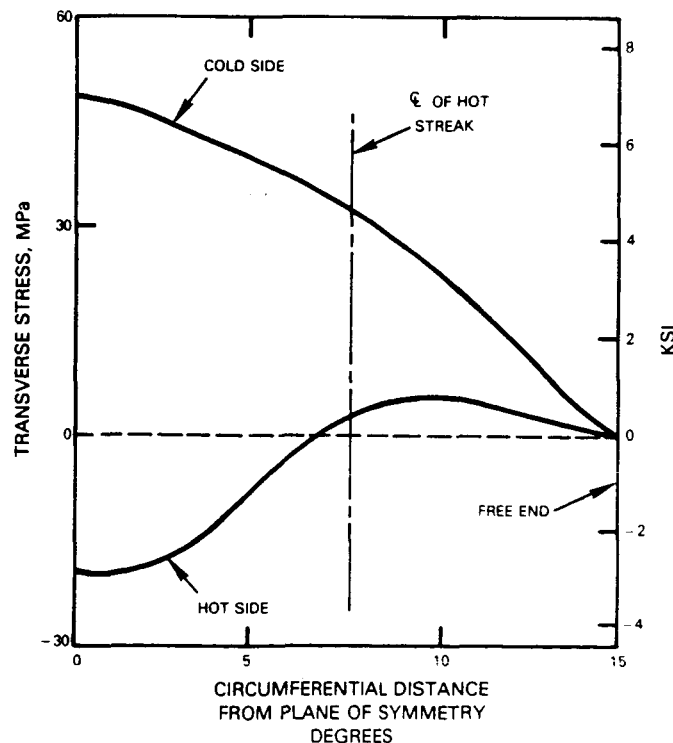
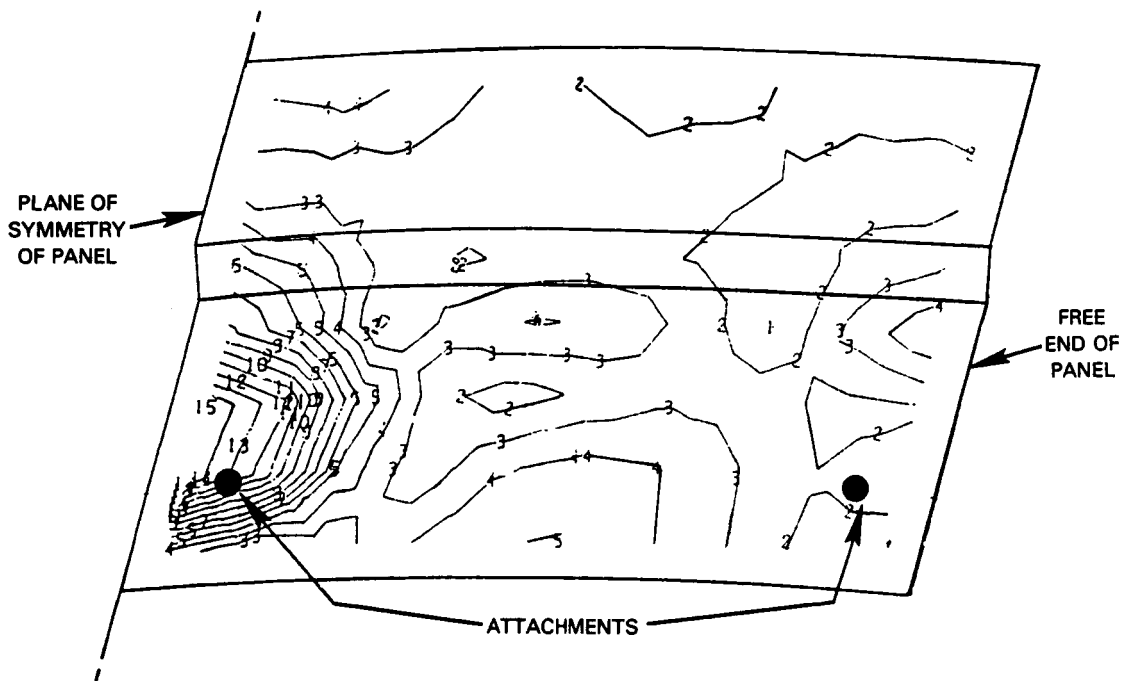


Figure 7-16 Distribution of Transverse Stress Component at Downstream End of Composite Panel

The structural analysis also computed the stresses in the Hastelloy X shell supporting in composite liner panels. Figure 7-17 shows the distribution of the Von Mises stress arising in the shell as a result of thermal and mechanical loads transmitted from the panels. With the shingle construction and unconstrained axial and transverse motion between panel and shell, the latter loads are very small. The overall stress levels in the shell are extremely low with the peak stress being only 8.15 MPa (1.181 ksi) in a region centered on the plane of symmetry of the panel and downstream of the attachment. The stresses are an order of magnitude less than those computed in the shell of the reference metallic segment liner of Section 4.4 which is a consequence of the elimination of transmission of couples to the shell by not having the panel attached at the upstream and downstream ends. With the Hastelloy X shell having a 0.2 percent yield stress of about 200 MPa (30 ksi) these stress levels are acceptable. The buckling analysis conducted on the shell of the reference liner in Section 4.4 is also valid for this configuration and indicated a factor of safety of more than 5.0 relative to the critical buckling load.

The foregoing static structural analysis of both the liner panel and the shell was conducted under the assumption of radial attachment between the segment and the shell at the attachment locations but with complete freedom of motion between these components in the axial and transverse direction. Mechanically this was equivalent to a bolted attachment in which the clamping action of the bolt or retention clip was strong, but the hole for the attachment bolt was well oversized in one or both components to allow the transverse and axial freedom of motion. To investigate the effect of constraint at the attachment the structural analysis was repeated with the modeling of the attachments altered to represent the extreme case where there was no freedom of motion between the panel and the shell, and the attachment was effectively "locked" or rigid in all three directions. The results of this analysis indicated that the stresses in the vicinity of the attachments rose to completely unacceptable levels. The transverse component in particular reached levels of nearly 1400 MPa (200 ksi) in compression in the composite panel at the "central" attachment as a consequence of the differential thermal expansion between the panel and the shell. This, in turn, led to radial compressive stresses in excess of 1100 MPa (160 ksi) in the composite material at that location. Predicted stresses of this magnitude mean only that the composite material would be crushed or the attachments failed long before loads of this magnitude could develop. The net benefit of analyzing this extreme case is to demonstrate the need to assure adequate freedom of motion in the attachment design to avoid the possibility of "locking" the attachments.



VON MISES STRESS

	MPa	(KSI)
1	-.282	-.041
2	.317	.046
3	.925	.134
4	1.53	.221
5	2.12	.308
6	2.73	.395
7	3.32	.483
8	3.92	.570
9	4.52	.657
10	5.14	.744
11	7.74	.832
12	6.26	.919
13	6.95	1.006
14	7.55	1.094
15	8.15	1.181

Figure 7-17 Stress Distribution in the Shell Supporting the Composite Liner Panels

The static structural analysis was concluded with an assessment of the loads on the panel to shell attachment bolts and their sizing. The static loads on the three bolts consist of the aerodynamic pressure force on the panel and the loads generated by differences in the radius of curvature of the panel relative to the shell when both are heated. As previously discussed, the differential thermal expansion of the metal and ceramic composite material gives rise to tensile loads in the attachment bolts near the free end of a panel on the outer liner shell and in the bolt at the center of a panel mounted on the inner liner of the combustor. The combination of these two static load effects produces a tensile force of 80 N (18 lb) at takeoff. The attachment bolts also experience potential vibratory loading; and if the panel moved as a rigid body with 200g acceleration, this would result in an alternating load on the attachment bolt of 58 N (13 lb). To add conservatism in sizing of the attachments, it was assumed that all the static and vibratory load will have to be resisted by any one attachment. Furthermore, a stress concentration factor of 3.0 was used to account for the threads in the attachment bolt. Based on the 3.81 mm (0.150 in) standard size attachment bolt of Figure 7-5, the overall static tensile stress in the bolt was calculated to be 65.5 MPa (9.5 ksi) while the vibratory components was 45.5 MPa (6.6 ksi). When plotted on the modified Goodman diagram of Figure 7-18, these stress levels are shown to be low compared to the load carrying capability of Hastelloy X at a conservatively high temperature of 760°C (1400°F).

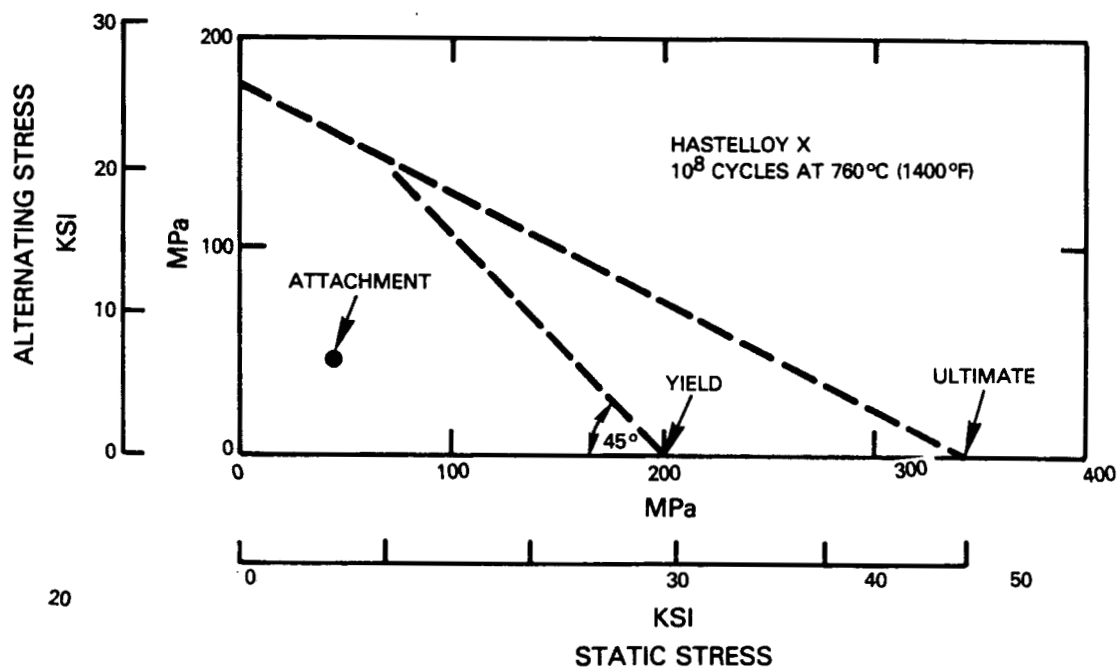


Figure 7-18 Axial Stress in the Composite Liner Attachment Bolts

On the basis of the foregoing discussion of the consequences of allowing the attachments to "lock" or constrain the panels to the shell in the plane of the latter, sizing of the clearance of the attachment hole in the panel is also a critical aspect. With the attachment bolts positioned on the plane of symmetry and 1.5 degrees from the free end of the panel, the nominal spacing between bolts is 12 degrees of arc. For an outer combustor liner having a nominal radius of 38 cm (15 in) the required circumferential growth allowance would be a minimum of 0.48 mm (0.019 in). A diametral clearance of 0.33 mm (0.013 in) would be required on the holes in a composite panel that would mount on an inner liner having a nominal radius of 25 cm (10 in). These clearances are beyond the stackup of tolerances associated with fabrication and assembly of the components.

7.7 Liner Life Analysis

The results of the static structural analysis of the composite liner panel and its supporting shell indicated that, if the attachments did not constrain transverse motion of the panel, the stress levels in both components were quite moderate. The maximum normal stress in the plane of the SiC fibers in a hot region of the liner panel was computed to be less than 55 MPa (8 ksi) which, based on the data of Section 6.2, is about half the elastic limit of the SiC-LAS material. The high through thickness temperature gradients in the composite panel give rise to shearing forces in the plane of the fibers but, as shown in Section 7.6, the maximum interlaminar shear stresses induced by these loads appears to be only about half those experienced by SiC-LAS beam specimens when they were yielding in tension in flexure tests at elevated temperatures. While it would appear that the magnitude of these predominantly thermally induced stresses are low relative to the conventional design parameters of concern; such as the proportionality limit and yield point; ceramic composites must also be recognized as a uniquely different class of materials that may be subject to other design constraints.

To provide a basis for interpreting the magnitude of the computed stresses in the composite liner panel in terms of life limiting factors, a structural analysis was conducted of one of the disc type specimens evaluated in the thermal fatigue tests of Section 6.5. These discs had a nominal thickness of 1.15 mm (0.045 in) which is identical to that of the composite liner panel and were cyclically heated to high temperature levels and through thickness temperature gradients. The analysis was conducted on the NASTRAN computer program with axisymmetric boundary conditions using the same six sided isoparametric (Hexa) element structural model used in the modeling of the composite panel in Section 7.4. It also incorporated the same orthotropic constitutive model of the SiC-LAS material that was described in that section. The structural analysis was conducted with a radial temperature distribution in the disc that was representative of that occurring at the peak of the thermal cycle during the testing of Specimen 3 of Table 6-VII. In particular, the periphery of the 7.6 cm (3.0 in) diameter disk was maintained at 537°C (1000°F), while the center was heated to 1150°C (2100°F) on the hot surface and 1040°C (1900°F) on the cold surface. The results of this analysis indicated that the maximum normal stress in the plane of the fibers occurred at the center of the disc and had a magnitude of about 48 MPa (7 ksi) which is comparable to the computed maximum in-plane normal stress in the liner panel.

The structural analysis of the composite liner panel in Section 7.6 had also indicated that the maximum tensile through thickness stress in the panel was about 31 MPa (4.5 ksi). There was cause for concern over this stress magnitude because it tends to pull the layers of the composite apart. However, the analysis of the thermal fatigue test specimen indicated that the through thickness tensile stress in the center of the specimen, at 34 MPa (5.05 ksi), was nearly identical in magnitude. In view of the fact that this test specimen had been subjected to 3500 thermal cycles during the fatigue tests and experienced only minor distress to the hot side surface and minute internal microcracking during this exposure, it appears that neither the in-plane or through thickness normal stresses computed to occur in the composite liner panel will be sufficient to lead to a thermal fatigue failure mode in the panel.

In the absence of significant thermal fatigue distress and the ensuing crack development and propagation failure mechanism encountered in conventional metallic combustor liners, it appears that the failure of the composite liner will be governed by material deterioration due to exposure to the high temperature environment. This mode will involve the removal of material from the hot side surface of the SiC-LAS shingle because of one or more processes including oxidation of the matrix or fibers, spalling or flaking of the surface layer, or erosion of the surface. The property characterization tests of Section 6.0 were insufficient in scope to identify the dominant mode of "hot time deterioration", and since failure by any of these modes would involve removal of a predefined quantity of material from the panel surface or penetration of a deficiency into that surface, long duration tests of the order of hundreds of hours would be required to define the rate of surface depletion. Lacking these data, it was not possible to formulate a complete damage model for the composite material that would be capable of predicting the life of the SiC-LAS combustor liner panels. However, a general failure model, applicable to most "hot time deterioration" modes, was formulated and has been evolved to the point where segment life may be expressed in terms of an empirically defined constant that could be evaluated in a future experiment.

The progressive removal of material from the hot side surface of the liner segment, regardless of the particular mode of depletion, must be dependent on time spent at elevated temperature. The rate of depletion in such a process is generally a strong function of the level of temperature above some threshold and assumes an Arrhenius character as defined by the equation:

$$R = C \exp (-A/T) \quad (7-2)$$

20

where: R = rate of material removal - mm/hr (in/hr)
 T = absolute surface temperature - °K (°R)
 C and A = constants that are functions of the material and the environment.

The constants C and A in Equation 7-2 may be eliminated by introducing the values of the depletion rates R^* and R_t which are the rate of depletion of the surface of the material at the temperatures T^* and T_t , respectively. This leads to the following equation for the rate of removal R at temperature T :

$$R = R^* \left(\frac{R_t}{R^*} \right) \left(\frac{T_t}{T_t - T^*} \right) \left(1 - \frac{T^*}{T} \right) \quad (7-3)$$

It is assumed that T_t is the threshold temperature at which the damage to the material, i.e., the rate of depletion R_t , is vanishingly small. Based on experience with the SiC-LAS material, this threshold temperature has been established at about 1256°K (1800°F). Likewise, T^* is the maximum temperature that the material will encounter during the operation cycle. Based on the thermal analysis of the composite liner design at the takeoff operating condition, this temperature is 1532°K (2303°F). While nothing is known of the magnitudes of the depletion rates R_t and R^* at these temperatures, based on the exponential character of the equation between these limits, R^* must be many decades larger than R_t with a value of the ratio (R_t/R^*) of 10^{-4} appearing appropriate. On this basis, the general depletion rate R can be defined as a multiple of the maximum depletion rate R^* from Equation (7-3).

This approach was applied to the composite combustor liner by examining the temperature history in the combustor of the reference advanced PW2037 engine during the 90 minute, 500 nautical mile reference mission defined in Section 3.0. Figure 7-19 shows the temperature history in terms of the combustor inlet and discharge temperatures and the maximum liner temperature as deduced from the thermal analysis of the composite liner. Using the above established threshold of distress of 1256°K (1800°F), the liner encounters damage, i.e., the depletion of material from the surface of the SiC-LAS panels, during three intervals:

- o a two minute period during takeoff;
- o a period of fifteen minutes during climb ending just prior to the start of cruise;
- o a short interval of about fifteen seconds during maximum thrust reversal after landing.

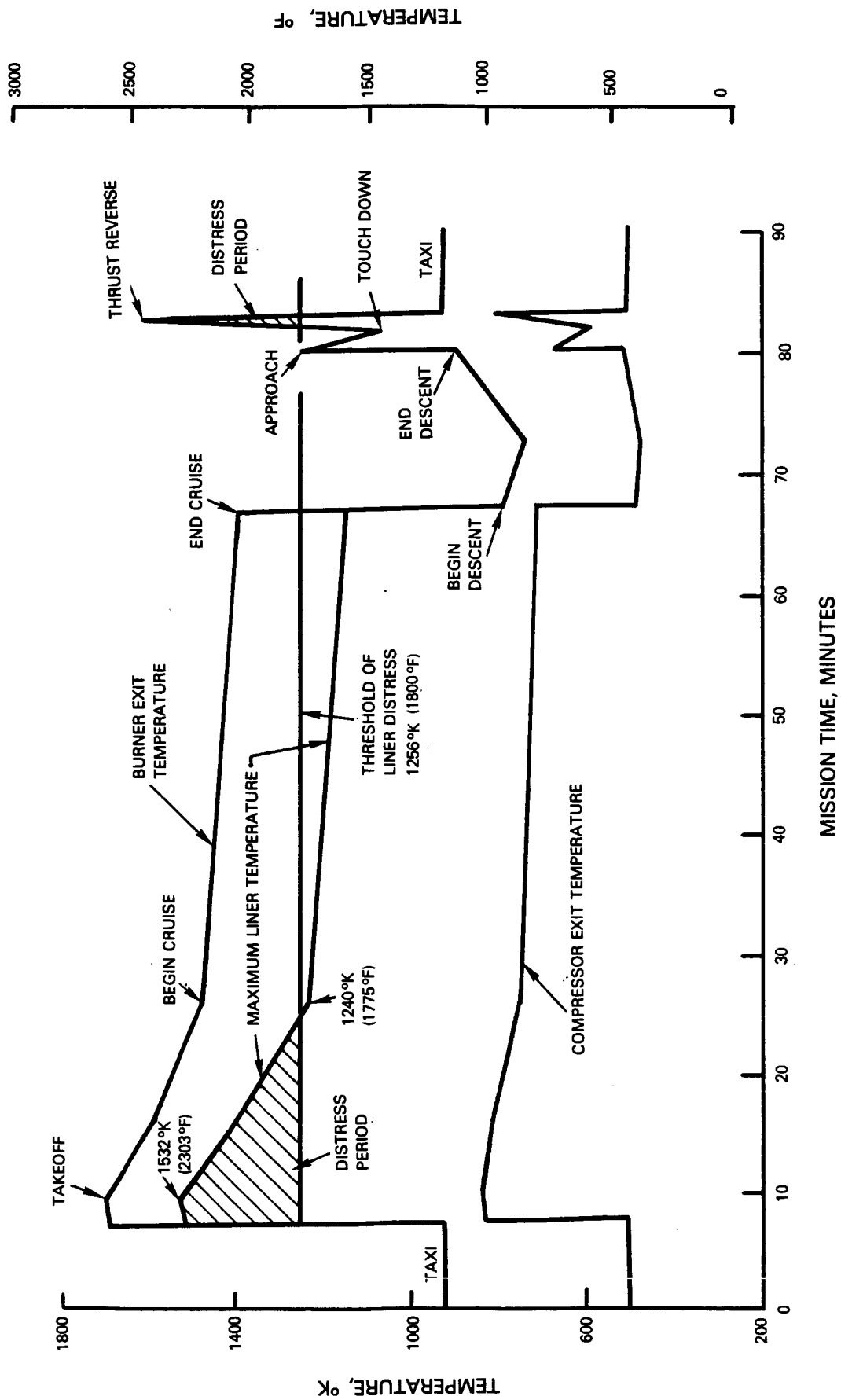


Figure 7-19 Distress Profile of Composite Liner During 500 Nautical Mile Mission

Numerical integration of Equation (7-3) over these three distress periods predicted that the total amount of material removed from the surface of the liner panels is $0.0554 R^*$ per mission. The breakdown of removal by distress period was: takeoff - 50.2 percent, climb - 49.1 percent, and thrust reversal - 0.7 percent. The nearly equal amounts of material depletion during the 2 minute takeoff and 15 minute climb intervals reflects the exponential characteristic of the Arrhenius rate equation. Expressed alternatively, the damage inflicted on the composite liner segment over one flight cycle is equivalent to that produced by 3.32 minutes of steady state operation at a surface temperature of 1532°K (2303°F) at which the removal rate is R^* mm/hr. If the composite liner is to attain the program goal of a service life of 15,000 hours which the reference metallic liner is projected to achieve, it must withstand 10,000 flight cycles. Taking the conservative position that failure occurs when the entire 1.14 mm (0.045 in) thickness of the composite panel is locally depleted, R^* must be equal to or less than 2.06×10^{-3} mm/hr to achieve this life.

7.8 Summation

The analysis of the composite combustor liner has identified a shingle type of liner construction as being the optimum aerothermal configuration consistent with the thermal properties of ceramic composite materials. Based on reasonably optimistic projections of the properties of these materials, which permit maximum surface temperatures of 1260°C (2300°F) at takeoff, a liner design employing the same cooling airflow as the reference metallic liner was defined. Structural analysis indicates that despite locally high through thickness temperature gradients the stress levels in the composite liner panels are low. By analogy with thermal fatigue test results of Section 6.0, it appears that these stresses will be insufficient to precipitate fatigue type failure in these components. The life limiting mechanism is concluded to be an unspecified material deterioration associated with long term exposure to elevated temperatures. While a model of such a distress mechanism has been formulated, there is currently an insufficient data base for its quantitative use to project liner life.

SECTION 8.0

ECONOMIC BENEFIT ASSESSMENT

An analysis was conducted to identify the economic benefits of the use of the ceramic composite combustor liner relative to the reference metallic segment liner defined and analyzed in Section 4.0. The economic analysis was based on the characteristics of the Boeing 757-200 aircraft powered by the PW2037 engine selected in Section 3.0 as the reference for this study. The airplane-engine combination was "flown" on the 500 nautical mile (90 minute) airline mission depicted in Figures 3-3 and 3-4 at typical load factors, with standard Air Transport Association (ATA) reserves and mission profile. Performance on this mission was used to generate airline operating economics for engines incorporating the reference metallic and the advanced composite combustor liner. The airplane economic model was used to generate direct operating cost trade factors. These factors potentially included the effects of engine performance increments, weight, initial cost and maintenance cost differentials on the direct operating cost of the aircraft. Following are the details of the means of defining these input factors:

Performance

Both the reference metallic segment combustor liner and the composite shingle liner were designed with the same quantity of liner cooling air, i.e., approximately 20.5 percent of combustor airflow. Hence, the net amount of air available for combustion in the primary zone and dilution functions are not altered. Likewise, both liners are designed to the same pressure drop and, consequently, there should be no difference in total pressure loss across the combustor section. In addition, no significant change is anticipated in combustor exit temperature profile or pattern factor as a result of the use of the composite liner. Hence, the quantity and distribution of cooling air to the turbine is not affected by the selection of the combustor liner. As a result, no advantages or debits in engine cycle performance or efficiency can be associated with the use of the composite liner and engine performance changes did not enter the analysis.

Weight

Differences in combustor liner weight due to material density and liner construction effects were determined and input to the analysis. The difference in weight was small for commercial aircraft applications, being only 22.8 N (11.27 lb) per engine in favor of the composite segment liner, and did not measurably affect the outcome of the analysis. For reference purposes, a change of 5050 N (2500 lb) per engine weight would produce a one percent difference in direct operating cost for the Boeing 757-200 - PW2037 airframe-engine combination on the 500 nautical mile mission. The weight differential could be more significant in a military application.

Initial Cost

The initial cost of the composite combustor liner relative to the metallic liner was incorporated in the analysis. The costs of fabricating the composite segments and casting metallic segments were estimated based on these being made at full production rate. Potential differences in fabrication costs for the liner shell, attachment hardware, and engine assembly were also recognized. Table 8-1 presents a breakdown of the initial cost of each liner configuration in which the cost of the elements and differentials are shown as a fraction of the total cost of the assembled metallic liner. The results indicate that the net fabrication and assembly cost of the combustor liner with the composite panels was 65.5 percent of that of the baseline metallic segment liner. The cost advantage arose from lower segment fabrication costs in that the layup and hot pressing of the simple constant thickness composite panels was less costly than casting the metallic segments. In addition, the metallic segments were assumed to be coated with an oxidation resistant coating that was not required on the composite material. These advantages were offset somewhat by higher attachment hardware and assembly costs for the composite liner design. These were attributable to the currently perceived need for more attachment points (324 vs. 276 per liner assembly) and more complex attachments for the composite liner panels. Some variations in the ground rules of the analysis could significantly alter the results of this aspect. For example, the analysis of Section 4.5 indicated the need for an oxidation resistant coating on the metallic segments was marginal. Deletion of the need to coat the metallic segments could eliminate about two-thirds of the cost advantage of the composite segment design. The study also revealed that the cost of casting the metallic segments could be reduced from 0.585 to 0.402 if they were made from INCO-713 rather than Modified B-1900. While this substitution would essentially negate the panel fabrication cost advantage of the composite liner, INCO-713 had been cited in the design of the reference metallic segment liner in Section 4.1 as having a much lower yield strength at elevated temperature than the Modified B-1900. This was suspect of leading to faster crack propagation and, hence, reduced life which would have altered the maintenance cost assessment. There is also a significant difference in the attachment hardware and assembly costs between the two liner concepts, and reducing the complexity of the attachment of the composite liner panel by eliminating the single panel removability feature could improve its initial cost position further. In addition, no consideration has been given in this analysis to the use of strategic materials in the metallic combustor liner segments. Shifts in the availability of these materials could have a substantial impact on the initial cost of these components, whereas the SiC-LAS composite liner panels do not incorporate critical materials and would not have such a sensitivity.

Table 8-I

Initial Cost Breakdown of Metallic and Composite Combustor Liner

	<u>Cast Metallic Segments</u>	<u>Composite Panels</u>	<u>Differential</u>
Liner Shell	0.120	0.120	0.0
Segment Fabrication	0.585	0.390	-0.195
Segment Coating	0.232	0.0	-0.232
Attachment Hardware and Assembly	<u>0.063</u>	<u>0.145</u>	<u>+0.082</u>
Total	1.000	0.655	-0.345

Maintenance Cost

The effect of the use of the composite liner on maintenance cost was recognized in the analysis by including the cost of replacement liner parts and the overhaul shop labor required for their installation. The most significant factor in determining maintenance cost is the frequency of replacement of the liner and related components. For the reference metallic liner, the structural and cyclic fatigue analysis of Section 4.0 was used to define the replacement intervals. That analysis indicated that the life of the metallic segment liner would be low cycle fatigue limited, and it was projected that cracks up to 6.6 mm (0.26 in) in length would develop in high temperature streak regions over the 15,000 hour or equivalently 10,000 flight cycles design life of these segments. This design life was used as the criteria for replacement of the metallic liner segments. As discussed in Section 7.7, the composite liner panels are not expected to have cyclic fatigue life limitations but rather will eventually fail from the effects of time dependent exposure to high temperatures. Since there is currently insufficient data to formulate a life prediction model for this material in a thermal exposure failure mode, a parametric approach was used in the benefit study by conducting the analysis for panel lives between overhaul of 0.66, 1.0, 1.5, and 2.0 times the 15,000 operating hour life of the reference metallic liner segments. Table 8-II presents a summary of the maintenance cost factors. The lower maintenance cost of the composite liner at equal lifetimes is attributable to the lower cost of replacement parts as reflected in the Initial Cost data of Table 8-I and discussed above.

Table 8-II

Relative Maintenance Cost and Direct Operation Cost
Comparison for Metallic and Composite Segmented Combustor Liners

	Cast Metallic Segments	SiC-LAS Composite Segments			
Life - hrs.	15,000	10,000	15,000	22,500	30,000
- x Goal	1.0	0.666	1.0	1.5	2.0
Relative Maintenance Cost	1.000	1.179	0.854	0.618	0.470
Direct Operating Cost of Total Aircraft With:					
Coated Metallic Segments	1.0000	1.0002	0.9995	0.9990	0.9987
Uncoated Metallic Segments	0.9999	1.0002	0.9995	0.9990	0.9987
Direct Operating Cost of Combustor Liner With:					
Coated Metallic Segments	1.000	1.091	0.773	0.545	0.455
Uncoated Metallic Segments	0.945	1.091	0.773	0.545	0.455

When all of the above factors were incorporated in the analysis, a projection of the impact on direct operating cost was generated based on a Jet A fuel cost of \$1.00 per gallon. As shown on Table 8-II, the results of this analysis indicate that the impact of combustor liner configuration on the total direct operating costs of the aircraft is small being only of the order of a tenth of a percent at the highest composite liner life ranges. To show the combustor liner cost and lifetime influences more effectively, Table 8-II also includes an equivalent "direct operating cost" of the combustor liner which includes the initial cost of the combustor liner assembly and the cost of all labor and hardware associated with its maintenance over the economic life of the aircraft. Based on either direct operating cost parameter, it is evident that the ceramic composite liner enjoys some

direct operating cost advantage at equal liner life and this obviously reflects the lower initial and replacement cost of the panels relative to the metallic segments. The break-even point for direct operating cost occurs at a composite liner panel life of 76 percent of that of the metallic segment or about 11,400 hours above which the composite liner is less costly. To demonstrate the effect of changes in initial cost factors, Table 8-II also includes the direct operating cost with uncoated metallic segments on the assumption that the absence of a coating will not compromise their lifetime. In this case, the break-even point shifts to a composite liner life of 81 percent of that of the metallic segment liner or 12,150 hours.

At the completion of the Benefit Assessment it was concluded that the cost of fabricating the liner segments with their attachment hardware and the frequency of their replacement were the only significant factors affecting a direct operating cost comparison. The composite liner was shown to produce a lower direct operating cost if its life was at least 75 percent of the 15,000 hour life of the reference metallic liner segments.

SECTION 9.0

CONCLUDING REMARKS

While limited in scope, this study has accomplished the objective of evaluating the technical feasibility and potential advantages of the use of high temperature composite materials in combustor liners for aircraft gas turbine engines. The results indicate that a composite consisting of silicon carbide (SiC) reinforcing fibers in a matrix of lithium aluminosilicate (LAS) offers unique opportunities for improved combustor liners. Economic studies based on an advanced PW2037 engine in the Boeing 757 aircraft indicate that a composite liner design concept consisting of film cooled shingles of SiC-LAS mounted on a Hastelloy X shell will consume the same quantity of cooling air, cost less to fabricate and weigh 22.8 N (11.27 lb) less than a comparable advanced technology segmented metallic combustor liner while also eliminating the need for critical strategic materials in the panels.

The ceramic composite material has been found to have high thermal fatigue resistance and it appears that the ultimate failure mode as a combustor liner material will be an as yet unidentified deterioration from accumulative exposure to elevated temperatures. While an analytical model has been formulated of such a failure mechanism, the lack of information on the deterioration processes, its rates and controlling mechanisms have precluded the quantification of this process into a life prediction system. To do so would require conducting relatively long duration laboratory scale tests to identify the critical factors and rates in the deterioration process. The potential benefits mandate conducting such a research activity to provide definition of the service life of SiC-LAS components at elevated temperatures.

The field of ceramic composite materials is very dynamic and near term improvements are anticipated in the strength and temperature capability of silicon carbide fibers and ceramic matrix materials. For example, in the relatively short period over which this study was conducted, an experimental variation to the lithium aluminosilicate matrix material was found to produce an increase of about 165°C (300°F) in the temperature at which comparable distress was observed in the thermal fatigue tests of Section 6.5. Such advances must be monitored and the resultant materials characterized to determine their impact on future combustor liner designs.

While the present study has addressed the specific application of composite materials to combustor liners, there are obviously other high temperature components in aircraft gas turbine engines that could exploit the unique properties of these materials. Similar feasibility and benefit assessments are required to identify these areas and the critical aspects of these applications. The accumulative results of such studies will provide direction for the overall development of ceramic composite materials.

REFERENCES

1. Roberts, R., A. Peduzzi and G. E. Vitti, "Experimental Clean Combustor Program, Phase I, Final Report," National Aeronautics and Space Administration CR-134756, October 1975.
2. Roberts, R., A. Peduzzi and G. E. Vitti, "Experimental Clean Combustor Program, Phase II, Final Report," National Aeronautics and Space Administration CR-134969, November 1976.
3. Roberts, R., A. Fiorentino and W. Greene, "Experimental Clean Combustor Program, Phase III, Final Report," National Aeronautics and Space Administration CR-135253, October 1977.
4. Dubiel, D. J., W. Greene, C. V. Sundt, S. Tanrikut and M. H. Zeisser, "Energy Efficient Engine Sector Combustor Rig Test Program Technology Report," National Aeronautics and Space Administration CR-167913, September 1982.
5. "MARC General Purpose Finite Element Program, Users Information Manual," MARC Analysis Research Corporation, Palo Alto, CA, 1981.
6. McCormick, C. W., editor, "MSC/NASTRAN Users Manual," Macneal-Schwendler Corporation, Los Angeles, CA, May 1983.
7. Layden, G. K. and K. M. Prewo, "Advanced Fabrication of SiC Fiber Reinforced Glass Ceramic Matrix Composites," Final Report, Office of Naval Research Contract N00014-81-C-0218, 1982.
8. Brennan, J. J., "Additional Studies of SiC Fiber Reinforced Glass-Ceramic Matrix Composites," Office of Naval Research Report R83-916018-2, February 1983.
9. Prewo, K. M., "Advanced Characterization of SiC Fiber Reinforced Glass Ceramic Matrix Composites," Office of Naval Research Report R83-915939-1, June 1983.
10. Prewo, K.M., J. J. Brennan and E. R. Thompson, "Study of Potential Engine Component Applications for Silicon Carbide-Glass Ceramic Materials," Office of Naval Research Report R81-915596-1, 1981.
11. Brennan, J., "Program to Study SiC Fiber Reinforced Glass Matrix Composites," Office of Naval Research Report R80-914401-4, November 1980.
12. Brennan, J. J. and K. M. Prewo, "Study of Lithium Aluminosilicate (LAS)/SiC Fiber Composites for Naval Gas Turbine Applications," Naval Air Systems Command Report R82-915778-4, October 1982.

REFERENCES (continued)

13. Petrasek, D. W. and R. A. Signorelli, "Tungsten Fiber Reinforced Superalloys - A Status Review," National Aeronautics and Space Administration TM 82500, January 1981.
14. Essock, D. M. and I. Machlin, "FeCrAlY Matrix Composites for Gas Turbine Applications," Proceedings of AIME Metallurgical Society Symposium on Advanced Fibers and Composites for Elevated Temperatures, February 1979.
15. Petrasek, D. W., E. A. Winsa, L. J. Westfall and R. A. Signorelli, "Tungsten Reinforced FeCrAlY - A First Generation Composite Turbine Blade Material," Proceedings of AIME Metallurgical Society Symposium on Advanced Fibers and Composites for Elevated Temperatures, February 1979.
16. Ahmad, I. and J. Barranco, "W-2% ThO₂ Filament Reinforced Cobalt Base Alloy Composites for High Temperature Application," Proceedings of AIME Metallurgical Society Symposium on Advanced Fibers and Composites for Elevated Temperatures, February 1979.
17. Signorelli, R. A., "Review of the Status and Potential of Tungsten Wire - Superalloy Composites for Advanced Gas Turbine Engine Blades," National Aeronautics and Space Administration TM X-2599, September 1972.
18. Warburton, R. E., T. E. Schmid and R. J. Miller, "Advanced Exhaust Nozzle System Demonstration," United States Air Force Aeropropulsion Laboratory Report AFWAL-TR-82-2051.
19. Stuart, E. H., "Preliminary Design Data for ACC-4," Southern Research Institute Document SoRI EAS-84-9, December 1983.
20. Stuart, E. H., "Thermal Conductivity of Two Carbon-Carbon Composites," Southern Research Institute Document SoRI EAS-82-148-4930-F, March 1982.
21. Taylor, R. E. and H. Groot, "Thermophysical Property Tests of Silicon Carbide Coated Carbon-Carbon Composite," Purdue University Report TPRL 236, December 1980.
22. "Leading Edge Structural Subsystem Preliminary Design Allowables for Improved Coating System," Vought Corporation Report DIR 2-53442/RCC/6-0033, September 1976.
23. "Development of a Thermal Protection System for the Wing of a Space Shuttle Vehicle, Phase II, Final Report," Vought Corporation Report to National Aeronautics and Space Administration MSC Report 20557, April 1972.

LIMITED DISTRIBUTION LIST - FINAL REPORT

ADVANCED COMPOSITE COMBUSTOR
STRUCTURAL CONCEPTS PROGRAM
CONTRACT NAS3-23284

NASA Lewis Research Center
Attn: Contracting Officer, MS 500-312
21000 Brookpark Road
Cleveland, OH 44135

NASA Lewis Research Center
Attn: Technical Report Control
Officer, MS 5-5
21000 Brookpark Road
Cleveland, OH 44135

NASA Lewis Research Center
Attn: Technical Utilization Office
MS 3-16
21000 Brookpark Road
Cleveland, OH 44135

NASA Lewis Research Center
Attn: AFSC Liaison Office, MS 501-3
21000 Brookpark Road
Cleveland, OH 44135

NASA Lewis Research Center
Attn: Structures Div. Contract
File, MS 49-6
21000 Brookpark Road
Cleveland, OH 44135

NASA Lewis Research Center
Attn: Library, MS 60-3
21000 Brookpark Road
Cleveland, OH 44135

NASA Lewis Research Center
Attn: L. Berke, MS 49-6
21000 Brookpark Road
Cleveland, OH 44135

NASA Lewis Research Center
Attn: R. H. Johns, MS 49-6
21000 Brookpark Road
Cleveland, OH 44135

NASA Lewis Research Center
Attn: J. A. Ziemianski, MS 49-6
21000 Brookpark Road
Cleveland, OH 44135

NASA Lewis Research Center
Attn: G. R. Halford, MS 49-7
21000 Brookpark Road
Cleveland, OH 44135

NASA Lewis Research Center
Attn: T. T. Serafini, MS 49-1
21000 Brookpark Road
Cleveland, OH 44135

NASA Lewis Research Center
Attn: R. A. Signorelli, MS 106-1
21000 Brookpark Road
Cleveland, OH 44135

NASA Lewis Research Center
Attn: N. T. Saunders, MS 49-1
21000 Brookpark Road
Cleveland, OH 44135

NASA Lewis Research Center
Attn: R. L. Thompson, MS 49-6
(15 copies)
21000 Brookpark Road
Cleveland, OH 44135

NASA Lewis Research Center
Attn: D. E. Sokolowski, MS 49-1
21000 Brookpark Road
Cleveland, OH 44135

NASA Lewis Research Center
Attn: F. I. Hurwitz, MS 106-1
21000 Brookpark Road
Cleveland, OH 44135

National Aeronautics & Space Admin.
Attn: NHS-22/Library
Washington, DC 20546

National Aeronautics & Space Admin.
Attn: RTM-6/M. A. Greenfield
Washington, DC 20546

National Aeronautics & Space Admin.
Attn: RTM-6/M. S. Hirschbein
Washington, DC 20546

National Aeronautics & Space Admin.
Attn: RTM-6/S. Venneri
Washington, DC 20546

NASA-Ames Research Center
Attn: Library, MS 202-3
Moffett Field, CA 94035

NASA-Goddard Space Flight Center
Attn: 252/Library
Greenbelt, MD 20771

NASA-John F. Kennedy Space Center
Attn: Library, MS AD-CSO-1
Kennedy Space Center, FL 32931

NASA-Langley Research Center
Attn: Library, MS 185
Hampton, VA 23665

NASA-Langley Research Center
Attn: M. F. Card, MS 244
Hampton, VA 23665

NASA-Langley Research Center
Attn: M. M. Mikulas, MS 190
Hampton, VA 23665

NASA-George C. Marshall
Space Flight Center
Attn: AS61/Library
Marshall Space Flt. Center, AL 35812

Jet Propulsion Laboratory
Attn: Library
4800 Oak Grove Drive
Pasadena, CA 91103

Jet Propulsion Laboratory
Attn: B. Wada
4800 Oak Grove Drive
Pasadena, CA 91103

NASA S&T Information Facility
Attn: Acquisition Division
(20 copies)
P. O. Box 8757
Baltimore-Washington
Int. Airport, MD 21240

Air Force Systems Command
Attn: Library
Aeronautical Systems Division
Wright-Patterson AFB, OH 45433

Air Force Systems Command
Attn: C. W. Cowie
Aeronautical Systems Division
Wright-Patterson AFB, OH 45433

Air Force Aeronautical
Propulsion Laboratory
Attn: Z. Gershon
Wright-Patterson AFB, OH 45433

Air Force Aeronautical
Propulsion Laboratory
Attn: E. Bailey
Wright-Patterson AFB, OH 45433

Air Force Flight Dynamics Lab.
Attn: C. B. Sendeckyj
Wright-Patterson AFB, OH 45433

Air Force Flight Dynamics Lab.
Attn: C. D. Wallace
Wright-Patterson AFB, OH 45433

Air Force Materials Laboratory
Attn: H. S. Schwartz
Wright-Patterson AFB, OH 45433

Air Force Materials Laboratory
Attn: T. J. Reinhart
Wright-Patterson AFB, OH 45433

Air Force Materials Laboratory
Attn: P. Pirrung
Wright-Patterson AFB, OH 45433

Air Force Materials Laboratory
Attn: E. J. Morrissey
Wright-Patterson AFB, OH 45433

Air Force Materials Laboratory
Attn: S. Lityak
Wright-Patterson AFB, OH 45433

Air Force Materials Laboratory
Attn: J. Rodehamel
Wright-Patterson AFB, OH 45433

Air Force Materials Laboratory
Attn: S. Tasi
Wright-Patterson AFB, OH 45433

Air Force Materials Laboratory
Attn: T. Cordell
Wright-Patterson AFB, OH 45433

Air Force Materials Laboratory
Attn: Library
Wright-Patterson AFB, OH 45433

Aerospace Corporation
Attn: Library-Documents
2400 E. El Segundo Blvd.
Los Angeles, CA 90045

Air Force Office of Scientific Res.
Attn: A. K. Amos
Washington, DC 20333

Department of the Army
Attn: AMCRD-RC
U. S. Army Material Command
Washington, DC 20315

Department of the Army
Attn: H. E. Pebly, Jr.
Plastics Technical Evaluation Center
Picatinny Arsenal
Dover, NJ 07801

Mechanics Research Lab
Attn: Dr. Donald W. Oplinger
Army Materials & Mechanics Res. Center
Watertown, MA 02172

Mechanics Research Lab
Attn: Dr. E. M. Lenoe
Army Materials & Mechanics Res. Center
Watertown, MA 02172

U. S. Army Missile Command
Attn: Document Section
Redstone Scientific Info. Center
Redstone Arsenal, AL 35808

Commanding Officer
U. S. Army Research Office (Durham)
Attn: Library
Box CM, Duke Station
Durham, NC 27706

Bureau of Naval Weapons
Attn: RRRE-6
Department of the Navy
Washington, DC 20360

Commander
U. S. Naval Ordnance Laboratory
White Oak
Attn: Library
Silver Springs, MD 20910

Commander
Naval Air System Command
Attn: A. Somoroff
U. S. Navy Department
Washington, DC 20360

Director, Code 6180
Attn: Library
U. S. Naval Research Laboratory
Washington, DC 20390

Naval Air Propulsion Test Center
Attn: Library
Aeronautical Engine Department
Trenton, NJ 08628

Naval Air Propulsion Test Center
Attn: R. Delucia
Aeronautical Engine Department
Trenton, NJ 08628

Naval Air Command Development
Center (60812)
Attn: Dr. J. Huang
Warminster, PA 18966

Naval Air Command Development
Center (60812)
Attn: T. E. Hess
Warminster, PA 18966

Federal Aviation Administration
Code NAE-214, Propulsion Section
Attn: Library
12 New England Executive Park
Burlington, MA 01803

Federal Aviation Administration DOT
Office of Aviation Safety, FEB 10A
Attn: Library
800 Independence Ave., S.W.
Washington, DC 20591

Federal Aviation Admin., AFS-140
Attn: T. G. Horeff
800 Independence Ave., S.W.
Washington, DC 20591

Massachusetts Institute of Technology
Dept. of Aeronautics & Astronautics
Building 33-307
Attn: Prof. J. W. Mar
77 Massachusetts Avenue
Cambridge, MA 02139

Univ. of Illinois at Chicago Circle
Department of Materials Engineering
Attn: Dr. Robert L. Spilker
Box 4348
Chicago, IL 60680

Univ. of Illinois at Chicago Circle
Department of Materials Engineering
Attn: Library
Box 4348
Chicago, IL 60680

Allison Gas Turbine Operation
General Motors Corporation
Attn: Mr. J. Byrd
Box 894
Indianapolis, IN 46206

Allison Gas Turbine Operation
General Motors Corporation
Attn: Library
Box 894
Indianapolis, IN 46206

General Dynamics/Convair Aerospace
Attn: Library
P. O. Box 1128
San Diego, CA 92112

General Dynamics/Convair Aerospace
Attn: J. L. Christian
P. O. Box 1128
San Diego, CA 92112

General Electric Company
Aircraft Engine Group
Attn: Mr. Herbert Garten
Lynn, MA 01902

General Electric Company
Aircraft Engine Group
Attn: Library
Lynn, MA 01902

General Electric Company
Aircraft Engine Business Group
Attn: Library, MS N32
Evendale, OH 45215

General Electric Company
Aircraft Engine Business Group
Attn: L. Beitch, MS G60
Evendale, OH 45215

General Electric Company
Aircraft Engine Business Group
Attn: M. Roberts, MS G60
Evendale, OH 45215

General Electric Company
Aircraft Engine Business Group
Attn: A. Adamson, MS G12
Evendale, OH 45215

General Electric Company
Aircraft Engine Business Group
Attn: R. Sprague, MS N82
Evendale, OH 45215

Grumman Aircraft Eng. Corp.
Attn: S. J. Dastin
Bethpage, Long Island, NY 11714

Grumman Aircraft Eng. Corp.
Attn: R. N. Hadcock
Bethpage, Long Island, NY 11714

IIT Research Institute
Technology Center
Attn: Library
Chicago, IL 60616

Lockheed California Company
Attn: Library
P. O. Box 551
Dept. 73-31, Bldg. 90, PL. A-1
Burbank, CA 91520

Lockheed California Company
Attn: Mr. Jack E. Wignot
P. O. Box 551
Dept. 73-31, Bldg. 90, PL. A-1
Burbank, CA 91520

Northrop Space Laboratories
Attn: Library
3401 West Broadway
Hawthorne, CA 90250

North American Rockwell, Inc.
Rocketdyne Division
Attn: Library, Dept. 596-306
6633 Canoga Avenue
Canoga Park, CA 91304

AVCO Lycoming Division
Attn: M. Robinson
550 South Main Street
Stratford, CT 06497

AVCO Lycoming Division
Attn: Library
550 South Main Street
Stratford, CT 06497

Boeing Commercial Airplane Company
Attn: D. Bouwer
P. O. Box 3707
Seattle, WA 98124

Boeing Commercial Airplane Company
Attn: Library
P. O. Box 3707
Seattle, WA 98124

Boeing Military Aircraft
BMAD
Attn: R. R. June
P. O. Box 3999
Seattle, WA 98111

Boeing Military Aircraft
BMAD
Attn: T. R. Porter
P. O. Box 3999
Seattle, WA 98111

Boeing Company
Attn: C. F. Tiffany
Wichita, KA

Boeing Company
Attn: Library
Wichita, KA

McDonnell Douglas Aircraft Corp.
Attn: R. Garrett
P. O. Box 516
Lambert Field, MO 63166

Douglas Aircraft Company
Attn: R. Kawai, MS 36-41
3855 Lakewood Blvd.
Long Beach, CA 90846

McDonnell Douglas Astronautics Co.
Attn: J. F. Garibotti
5301 Bolsa Avenue
Huntington Beach, CA 92647

Garrett-AiResearch
Attn: L. A. Matsch
111 South 34th Street
P. O. Box 5217
Phoenix, AZ 85010

General Dynamics
Attn: Library
P. O. Box 748
Fort Worth, TX 76101

General Dynamics
Attn: D. J. Wilkins
P. O. Box 748
Fort Worth, TX 76101

North American Rockwell, Inc.
Space & Info. Systems Division
Attn: Library
12214 Lakewood Blvd.
Downey, CA 90241

Teledyne CAE
Attn: D. E. Barbeau
1330 Laskey Road
Toledo, OH 43612

Aeronautical Research Association
of Princeton, Inc.
Attn: Library
P. O. Box 2229
Princeton, NJ 08540

Republic Aviation
Attn: Library
Fairchild Hiller Corporation
Farmington, Long Island, NY

Rohr Industries
Attn: Mr. John Meaney
Foot of H Street
Chula Vista, CA 92010

TRW
Attn: I. Toth
23555 Euclid Avenue
Cleveland, OH 44117

Composites Horizons
Attn: Library
2303 W. Valley Blvd.
Pomona, CA 91768

Hamilton Standard
Attn: Library
Windsor Locks, CT 06096

Hamilton Standard
Attn: R. A. Cornell
Windsor Locks, CT 06096

Hamilton Standard
Attn: W. Percival
Windsor Locks, CT 06096

Materials Sciences Corporation
Attn: E. W. Rosen
1777 Walton Road
Blue Bell, PA 19422